Signal processing methods based on the local polynomial fourier transform

Li, Xiu Mei

2010

Li, X. M. (2010). Signal processing methods based on the local polynomial fourier transform. Doctoral thesis, Nanyang Technological University, Singapore.

https://hdl.handle.net/10356/40206

https://doi.org/10.32657/10356/40206

Signal Processing Methods Based on the Local Polynomial Fourier Transform

LI XIUMEI

School of Electrical & Electronic Engineering

A thesis submitted to the Nanyang Technological University
in partial fulfillment of the requirement for the degree of
Doctor of Philosophy

2010

Acknowledgements

I would like to express the deepest appreciation and sincere gratitude to my supervisor, Dr. Guoan Bi, for his guidance, kindness and many invaluable comments and suggestions throughout the whole research project. Without his encouragement and support, the achievement of my thesis would be impossible.

I also take this opportunity to acknowledge my family members who have shown so much concern and care in the course of my studies. Their encouragement and unyielding support have contributed to the completion of this thesis.

I wish to thank Curtis Condon, Ken White, and Al Feng of the Beckman Institute of the University of Illinois for the bat data and for permission to use it in this thesis.

Thanks are given to Nanyang Technological University for the award of a research scholarship which enabled me to undertake this research. Besides, I am grateful to all the people in the Information System Research Laboratory, for their generous assistance and valuable suggestions provided throughout the entire project.

Last but not least, special thanks are given to all my friends. Without them, I would feel much more lonely in this long journey.

Contents

Summary

The majority of signals encountered in real applications, such as radar, sonar, speech, and communications, are often characterized by time-varying spectral contents. For this type of signals whose frequency contents evolve with time, signal representation in time or frequency domain alone cannot fully describe its time-varying characteristics. It would be far more useful to describe the signals with the time-frequency representations (TFRs).

The TFRs for processing signals with time-varying frequencies can be generally categorized as linear and nonlinear transforms. The widely used linear transform is the short-time Fourier transform (STFT). The nonlinear transforms include the Wigner-Ville distribution (WVD) and various classes of quadratic time-frequency transforms. During the studies of various signal processing methods, it is found that the local polynomial Fourier transform (LPFT) is an important and effective processing tool for many practical applications, mainly because the LPFT is a linear transform and free from the cross terms that exist in the WVD. Furthermore, the LPFT uses extra parameters to approximate the phase of the signal into a polynomial form to describe time-varying signals with a much better accuracy than the STFT.

This thesis focuses on the theoretical analysis of the LPFT, such as its uncertainty principle and SNR analysis, followed by applications to demonstrate its advantages and verify the theoretical analysis of the LPFT. Moreover, the

reassignment technique is employed to further increase the concentration of the local polynomial periodogram (LPP), which is the square of the LPFT.

First, the uncertainty principle of the LPFT is investigated. It is shown that the uncertainty product of the LPFT of an arbitrary order is related to the signal parameters, the window function, and the errors of estimating the polynomial coefficients. The uncertainty principle of the LPFT becomes time-independent when the Gaussian window is used to segment the signal and the parameters of the LPFT kernel are estimated correctly. Factors that affect resolutions of signal representation, such as the window width, the length of overlap between signal segments, order mismatch and estimation errors of polynomial coefficients, are also discussed. Examples in speech and bat sound processing are demonstrated to show the advantage of the LPFT, compared with the STFT and the WVD.

Second, the quantitative signal-to-noise ratio (SNR) analysis of the LPFT is derived based on the relationship between the LPFT and the WVD. The quantitative SNR analysis of the pseudo WVD (PWVD) in continuous-time form is presented as well. Comparisons are made among the SNRs achieved by using the LPFT, the FT, the STFT and the PWVD. Both the theoretical analysis and simulations have shown that the LPFT can provide higher SNR improvement than the FT, the STFT and the PWVD.

Third, applications in radar imaging and linear frequency modulated (LFM) signal detection are presented to show the improved performance using the LPFT and to verify the theoretical SNR analysis of the LPFT. It shows that compared with the FT and the STFT, the resolution of the ISAR images are improved by using the LPFT. Furthermore, the improvement on imaging performance is obtained by the non-overlapping approach to minimize the required computational complexity. Since it can provide a better noise suppression than the PWVD, the LPFT is a better tool to be combined with the Hough transform for LFM signal detection. Simulations are presented for the detection of

LFM signals corrupted by additive white Gaussian noise (AWGN) and impulsive noise to show that the LPP-Hough transform (LHT) achieves significant performance improvement on detecting LFM signals in very low SNR environments. In addition, the computation time needed by the LHT can be further reduced by using the time-frequency filtering.

Finally, the reassignment method is extended to the LPP to get the reassigned LPP. Its interesting properties, such as perfectly localization of the chirp and impulse signals, are investigated with mathematical proofs. Compared with the reassigned spectrogram and reassigned smoothed pseudo WVD, the reassigned LPP shows the desirable ability for improvement on the signal concentration in the time-frequency domain. Moreover, the reassignment method is extended to the robust methods, such as the robust spectrogram and the robust LPP, to process signals corrupted by impulsive noise. Performances using various LPP-related methods are compared for signals in AWGN, impulsive noise, and the mixture of AWGN and impulsive noises. It shows that while the reassigned LPP can improve the distribution concentration for signals in AWGN, the reassigned robust LPP can achieve improved concentration for signals in impulsive noise because the median filtering effectively minimizes the effects of the impulsive noise. However the reassigned LPP and reassigned robust LPP are not useful to minimize the mean squared errors of instantaneous frequency estimation, compared with those without reassignments.

List of Figures

List of Tables

List of Abbreviations

AWGN	additive white Gaussian noise
CRLB	Cramér-Rao low bound
FT	Fourier transform
DFT	discrete Fourier transform
FFT	fast Fourier transform
FM	frequency modulated
FRFT	fractional Fourier transform
HAF	high-order ambiguity function
HIM	high-order instantaneous moment
IF	instantaneous frequency
i.i.d	independent and identically distributed
IGAF	integrated generalized ambiguity function
LFM	linear frequency modulated
LPFT	local polynomial Fourier transform
LPP	local polynomial periodogram

MLE	maximum likelihood estimation
MSE	mean squared error
PHAF	product high-order ambiguity function
PPS	polynomial-phase signal
PTFT	polynomial time frequency transform
PWHT	pseudo Wigner-Hough transform
PWVD	pseudo Wigner-Ville distribution
RID	reduced interference distribution
SNR	signal-to-noise ratio
STFT	short-time Fourier transform
TFR	time-frequency representation
TFT	time-frequency transform
WHT	Wigner-Hough transform
WVD	Wigner-Ville distribution

Chapter 1

Introduction

1.1 Motivation

In many practical applications, such as radar, sonar, and communications, the signals under consideration are usually time-varying, that is, their frequencies are varying with time. According to the Weierstrass approximation theorem [1], the phase of an arbitrary time-varying signal can be well approximated by a polynomial of sufficient order. This kind of time-varying signals with polynomial phase, also known as the polynomial-phase signals (PPSs), are of significant importance. The PPSs have been reported to be used in many different areas, such as biomedical engineering [2–4], image processing [5, 6], image and audio watermarking [7, 8], motion estimation in video sequence [9, 10], communications [11–17], sonar [18] and radar applications [19–24]. The following are some examples.

- In biomedical engineering, seizures usually occur as the first sign of underlying neurological disease or dysfunction in the newborn. Electroen-

cephalogram (EEG) is a useful tool in evaluating a person's tendency for seizure disorders. It has been shown that the EEG signals exhibit significant nonstationary and multicomponent feature [3, 4]. Characterizing nonstationary EEG signals is a first step toward a global method of seizure detection and classification.

- In the direct-sequence spread spectrum (DSSS) system, its performance will deteriorate significantly when the interference is broadband such as the linear or nonlinear frequency modulated (FM) interference. This kind of interference may appear when the DSSS signal is transmitted in a band containing PPS transmission to enhance the security [11]. Estimations of the phase parameters of these PPSs provide the information to detect and excise the interference [12, 13], therefore improving the error rate performance and leading to increased system capacity and acquisition capability.

- In inverse synthetic aperture radar (ISAR) imaging, when the target has a rotational motion, its kinematic parameters can be modelled by the PPS [19]. In synthetic aperture radar (SAR), there is an increasing demand for high resolution at low frequencies to recognize targets moving under various scenarios such as hidden by foliage [20]. In such a case, longer observation intervals are needed and the received signal can be modelled as higher-order PPS [21].

The general frequency representation, Fourier transform (FT), is not suitable for the time-varying signals, because it does not tell us when the frequencies of the signals occur. As a result, in many real-time applications, it is far more useful to characterize the signals with the time-frequency representations (TFRs).

The TFR describes how the frequency content of a signal evolves over the time and helps us obtain more detailed information of the time-varying signals. The advantages of TFRs have been shown in a variety of applications such as radar imaging [25], radar target detection [26], communications [27, 28], music analysis [29–31], speech signal processing [32] and biomedical signal processing [4, 33].

There exist many different TFRs, and they generally fall into two categories, which are linear TFRs and nonlinear TFRs [34–36]. Linear TFRs mainly include the short-time Fourier transform (STFT) and the wavelet transform. Nonlinear TFRs include the Wigner-Ville distribution (WVD), the ambiguity function (AF), smoothed versions of the WVD, and the Cohen's class. Generally speaking, it is impossible to select a particular TFR for all possible applications. The choice of a TFR depends on the available properties of the TFR and the specific application at hand [34–36]. For instance, the WVD is known to be optimal for monocomponent linear frequency modulated (LFM) signals since it achieves the best energy concentration around the signal instantaneous frequency (IF) law. Therefore it has been used as the optimal IF estimator for LFM signals [37] and is well suited to time-varying filtering particularly for moncomponent signals [18]. To evaluate whether a TFR is a suitable tool for practical high resolution time-frequency analysis, the following criteria are generally considered.

- High concentration. Concentration describes how the TFRs concentrate along the signal's instantaneous frequency. To improve the concentration, we need to minimize the sidelobe amplitude relative to mainlobe amplitude, and to minimize mainlobe bandwidth about the signal instantaneous frequency.

- High resolution. Resolution usually means whether we can separate two

closely located components in the time and/or frequency domains. The resolution can be measured by the minimum frequency separation between the components' mainlobes where their amplitudes and bandwidths are preserved.

- Minimized cross terms for multicomponent signals. Due to their nonlinearity, nonlinear transforms generally suffer from the cross terms when multicomponent signals are considered. Since the cross terms often make the interpretation of the results difficult, it is greatly desired to suppress the cross terms.

- Low computational complexity. In many practical applications, real-time processing is required. To support high processing throughput, it is crucial to select a TFR with low computational complexity.

Each TFR has its own advantages and disadvantages. For example, the linear STFT is simple to implement and free from the cross terms for multicomponent signals, but it only provides low resolution for time-varying signals. In contrast, the WVD provides high resolution but contains cross terms for multicomponent signals. The LPFT, which is a generalized form of the STFT, was presented recently [38]. Since it uses extra parameters to approximate the polynomial phase of the PPSs, the LPFT can provide much better concentration and resolution than the STFT. Moreover, due to its linearity, the LPFT is free from the cross terms that exist in the WVD. The disadvantage of the LPFT is that it is computationally demanding because its calculation involves the estimation of extra parameters using the maximum likelihood estimator polynomial time frequency transform (PTFT) [39, 40]. Luckily, various fast algorithms [39, 41–47] have been proposed to reduce the computational complexity of the PTFT.

Furthermore, methods to reduce the overlap between adjacent segments are also presented to reduce the computational complexity [48]. In this way, the computational load of the LPFT can be greatly reduced.

The LPFT has received considerable attention in the past years. The properties of the LPFT were studied and its energy concentration was illustrated in [38]. This concentration motivates the use of the LPFT as an IF estimator [49]. Moreover, the LPFT has been used in a variety of applications, such as radar imaging [50, 51], interference suppression in communications [52, 53], motion parameter estimation in video sequences [10], and the IF estimation [38, 49]. Although much research has been done on the LPFT, there are still a lot of questions that remain open and further investigations are always desired to gain better understanding of the LPFT. In this thesis, we focus on the following four areas.

1.1.1 Uncertainty Principle of the LPFT

The uncertainty principle, which arose in quantum mechanics, has been a fundamental issue in signal analysis [54]. The compromise between signal concentrations in the time and frequency domains is generally described in the form of the uncertainty principle. Generally speaking, the more concentrated the signal is, the more spread out its Fourier transform must be. Particularly, the scaling property of the Fourier transform may be illustrated as follows: if we "squeeze" a signal in the time domain, its Fourier transform will "stretch out" in the frequency domain. It is well known that it is not possible to arbitrarily concentrate a signal in both time and frequency domains at the same time.

Many different transforms, such as the time-frequency transforms of the Co-

hen's class [55, 56], the fractional Fourier transform [57] and the linear canonical transform [58], are limited by the uncertainty principles. For example, it was reported that the STFT is restricted by the uncertainty principle [59]. It is understood that a shorter window used to capture the signal segment leads to a better resolution in time domain but a poorer resolution in the frequency domain to represent the signal. In contrast, a longer window used to capture the signal segment leads to a better resolution in the frequency domain but a poorer resolution in the time domain.

The LPFT, as a generalized form of the STFT, has been shown that its resolution in the time-frequency domain is also affected by the window length which controls the trade-off of bias and variance [38, 49]. However, a comprehensive study on the uncertainty principle for the LPFT has not been reported in the literature. Therefore, it will be of great interest to investigate the uncertainty principle of the LPFT and the main factors which will affect the performance of this time-frequency representation.

1.1.2 SNR Analysis of the LPFT

One important feature of time-frequency representations (TFRs) is that they usually increase the signal-to-noise ratio (SNR) in the time-frequency domain [60]. To quantitatively analyze the SNR increase by using TFRs is an important issue for practical applications. Generally the SNR is defined as the ratio of the mean power of the signal over the mean power of the noise, where the mean is taken over the entire domain. However, this definition is not proper for evaluating the possibility of detecting the narrowband signals in the frequency domain as well as for time-varying signals in the time-frequency domain [61].

Therefore another definition of SNR, which is similar to the definition of 3dB SNR in communications where only the signal in the 3dB bandwidth is considered, is introduced in [61]. This 3dB SNR definition is transform-domain dependent and directly relates to the bandwidth of the signal. It is suitable for signals in the time-frequency domain as well as in the time domain and frequency domain. Following this definition, quantitative SNR analysis of the STFT and the WVD has been presented [61, 62].

In various applications [10, 38, 49–53], compared with the FT and the STFT, the LPFT has shown its capability for improving the SNR. For example, in radar imaging, the LPFT can achieve more focused and clearer image than that using the STFT in cases of fast maneuvering targets [50, 51]. For interference suppression in communication systems, the LPFT is able to achieve performance improvement in comparison with that obtained from the systems based on the STFT [52, 53].

However, how much SNR improvement can be obtained with the LPFT has not been investigated in the literature. The SNR analysis of the LPFT should be further studied to help us quantitatively evaluate the SNR improvement achieved by using the LPFT.

1.1.3 Applications of the LPFT

Some applications, such as the ISAR imaging and LFM signal detection, are needed to demonstrate the improved performance achieved by using the LPFT and verify the theoretical SNR analysis of the LPFT.

1.1.3.1 ISAR Imaging

Radar image formation is a process of reconstructing images of radar targets from recorded complex data [63]. When the movements of radar targets are complicated such as rotation, acceleration or maneuvering, the time-frequency transforms (TFTs) can be used to achieve more focused and clearer ISAR images [25, 63].

Different types of TFTs have been employed for ISAR imaging. For example, the short-time Fourier transform (STFT) [25] is employed in ISAR imaging due to its simplicity and easy implementation. However, its resolution is low for time-varying signals. High resolution TFTs, such as Wigner-Ville distribution (WVD) [25] and continuous wavelet transform [64], were studied for ISAR image applications. However, the performances achieved by using some of these transforms generally suffer from the cross-term interferences. In general, it is desired to find a TFT that provides high concentration, has low cross-term interferences and accurately reflects the IF of the analyzed signal.

As introduced before, the LPFT can provide high resolution for time-varying signals with a local polynomial function approximating to the IF characteristic of the analyzed signals. In addition, it is free from the cross terms due to its linearity. Therefore, the LPFT can be employed as the TFT to process the LFM signals for ISAR imaging to obtain higher resolution images.

1.1.3.2 LFM Signal Detection

Among the PPSs, the linear frequency modulated (LFM) signals, also known as the chirp signals, are the most common ones in nature. For example, they can

be observed in echolocation by bats and dolphins [22], epileptic seizure activity in electroencephalographic (EEG) data [65], and glissando in music which is a slide up or down the notes of a scale [66]. They are also extensively used in manmade systems, such as radar and sonar [19]. In these areas, chirp detection is important since it helps in understanding the underlying characteristics of the signal.

For LFM signal detection, the time-frequency based methods have attracted significant attention [67–69]. Since a LFM signal will be described as a straight line in the time-frequency domain, it is possible to combine the TFR with some image processing tools, such as the Hough transform, for LFM signal detection. The Hough transform is a feature extraction technique to detect lines in an image, which has been widely used in image analysis, computer vision and digital image processing. It is robust to the extraneous noise due to the line integration. Therefore, by resorting to the Hough transform, the task of tracking straight lines in the time-frequency domain is turned into locating the maximum peak in the signal parameter domain.

The WVD has been combined with the Hough transform for LFM detection [67]. However, the WVD is suffered from cross terms for multicomponent signals. Moreover, the WVD cannot provide good representation for signals under heavy noise due to the inherent noise threshold effect problem [37]. It is desirable to use some other transforms, such as the LPFT, which can concentrate the LFM signal in low SNR environment to achieve better representation, then the Hough transform can be employed as the post-processor to detect the LFM signals.

1.1.4 Combining the Reassignment Method with the LPFT to Further Improve the Concentration

As mentioned above, a good TFR should provide high concentration and resolution for signals in the time-frequency domain. Although the LPFT can provide a good resolution for the time-varying signals, methods to further increase the concentration and resolution are always preferred so that an accurate interpretation of the signal components can be possibly made.

The reassignment method is an effective operation to improve signal concentration in the time-frequency domain. It has been generalized to deal with the bilinear time-frequency and time-scale distributions [70], the affine class [71] and S-method [72]. This observation motivates us to extend the reassignment method to the local polynomial periodogram (LPP), which is the squared LPFT, to further improve the concentration of time-varying signals.

In practice, the signals under consideration are always corrupted by noise. In general, the embedded noise is assumed to be additive while Gaussian noise (AWGN). However, in some situations, such as in the applications of communications and imaging, signals are disturbed by noises exhibiting the impulsive characteristics. For these situations, the robust methods [73, 74] are often used. It will be interesting to extend the reassignment method to the robust methods to improve the concentration of signals corrupted by impulsive noise. Moreover, performance analysis of the reassigned LPP (RLPP) and the reassigned robust LPP (RrLPP) in different noise environments is also desired.

1.2 Objectives

This thesis aims to further explore the LPFT with theoretical analysis and to process time-varying signals with techniques based on the LPFT. The main objectives of this thesis are summarized as follows.

- To investigate the uncertainty principle of different order LPFTs and to get a generalized form of the uncertainty product.
- To present the quantitative SNR analysis of the LPFT, with comparison to that of the FT, the STFT and the WVD.
- To demonstrate application examples of the LPFT in radar imaging and LFM signal detection in heavy noise environments.
- To combine the reassignment method with the LPP to improve the concentration in the time-frequency domain. The properties of the reassigned LPP are to be investigated. The reassignment method is also to be combined with the robust methods, such as the robust spectrogram and the robust LPP, to improve the concentration for signals in impulsive noise. Performances of various LPP-related transforms are to be compared in different noise environments.

1.3 Major Contributions of the Thesis

The major contributions of the thesis are as follows:

- From the second-order, third-order and fourth-order LPFT, the uncertainty principle is generalized to the Mth-order LPFT, and the derivation

of the uncertainty principle of the Mth-order LPFT with correctly estimated parameters is also given. It is shown that the uncertainty product of the LPFT is affected by the signal parameters and the window function, in addition to the errors of estimating the polynomial parameters. A few issues, such as the window width, the overlap length between the signal segments, the order mismatch and the estimation error, are explained in terms of the uncertainty products. The LPFT is compared with the FT, STFT and WVD to show its superiority in processing time-varying signals such as the speech signal and the bat sound.

- Based on the relationship between the LPFT and the WVD, theoretical analysis on the 3dB SNR achieved by using the LPFT is provided. The 3dB SNR analysis of the pseudo WVD in continuous-time form is also presented. Comparisons are made among the SNRs achieved by using different transforms such as the LPFT, the FT, the STFT and the WVD. Theoretical analysis and simulations show that the LPFT can provide improved SNR, compared with the FT, the STFT and the WVD.

- Application examples in radar imaging and LFM signal detection are presented to show the improved SNR performance achieved by using the LPFT. It shows that compared with the FT and the STFT, the resolution of the ISAR images is improved by using the LPFT. Furthermore, the improvement on imaging performance is obtained by the non-overlapping approach to minimize the required computational complexity. Compared with the WVD, the LPFT can better suppress the noise effect. Therefore, the LPFT is a better tool to be combined with the Hough transform for LFM signal detection. Using the Wigner-Hough transform (WHT) and

the LPP-Hough transform (LHT), simulation results for detecting mono-component and multicomponent LFM signals are presented. Compared with the WHT, the LHT can provide better detection for LFM signals in very low SNR environments.

- The reassigned LPP (RLPP) is developed and its interesting properties are investigated with mathematical proofs. Simulation results for various signals, such as parallel linear chirps, crossed linear chirps, parabolic frequency modulated signals and sinusoidal frequency modulated signals are presented to show that the reassigned LPP is capable of improving the signal concentration in the time-frequency domain. The reassignment method is also combined with the robust methods to process signals in impulsive noise. Furthermore, performance using various LPP-related methods are compared for signals in different noise environments, in terms of readability, computation complexity, distribution concentration, and mean squared error (MSE) of IF estimation.

1.4 Organization of the Thesis

The rest of the thesis is organized as follows.

Chapter 2 outlines the basics for the analysis of PPSs. The background of the PPS model and the Cramér-Rao lower bound (CRLB) of the PPS parameters are reviewed. The parametric methods, which are utilized for the estimation of the PPSs, are introduced and compared. Finally, a review of time-frequency representations, such as the STFT, the WVD and the LPFT, is given.

In Chapter 3, the uncertainty principle of the LPFT with arbitrary or-

der is investigated. Some issues which affect the signal concentration in the time-frequency domain are discussed. Comparisons and simulations among the STFT, the WVD and the LPFT are presented to show the advantage of the LPFT.

Based on the relationship between the LPFT and WVD, Chapter 4 provides theoretical SNR analysis for the LPFT. Comparisons are made among the SNRs achieved by using the LPFT, the FT, the STFT and the WVD. Simulations are given to show that the LPFT can achieve higher SNR improvement than the FT, the STFT and the WVD.

In Chapter 5, application examples in radar imaging and LFM signal detection are presented to verify that the LPFT can achieve improved SNR performance compared with other transforms such as the FT, the STFT and the WVD.

Chapter 6 focuses on the reassigned LPP and its properties to improve the signal concentration in the time-frequency domain. The reassigned robust methods are also proposed to better process the signals in impulsive noise. Performance on LPP-related transforms are compared in various noise environments.

This thesis is concluded in Chapter 7. Some recommendations for future work are also given in Chapter 7.

Chapter 2

Background

2.1 Introduction

This chapter is to review some fundamental concepts related to the time-varying signals and to provide the necessary background for better understanding the following chapters. The rest of this chapter is organized as follows. Section 2.2 discusses the PPS and its CRLB. In Section 2.3, the suboptimal maximum likelihood methods, such as the high-order ambiguity function (HAF) and the product HAF (PHAF), are briefly introduced. The polynomial time frequency transform (PTFT) is introduced as the maximum likelihood method and is compared with the suboptimal maximum likelihood methods to show its advantages. The fast algorithms for the PTFT are also presented. Finally the time-frequency representations are introduced and reviewed in Section 2.4. Several basic representations such as the STFT and WVD are introduced, and the local polynomial Fourier transform (LPFT) is discussed with its definition and properties.

2.2 The PPS and Its CRLB

As stated in Chapter 1, polynomial-phase signals (PPSs) are often used in a variety of applications, such as pulse compression radar systems [23, 24], synthetic aperture radar imaging [63] and mobile communications [75]. The form of the PPS is defined as

$$s(t) = A(t)e^{j\phi(t)}, \tag{2.2.1}$$

where $A(t)$ is the amplitude and $\phi(t)$ is the phase of the signal. An important parameter of the time-varying signal is the instantaneous frequency (IF) defined as the derivative of the phase, i. e. $f(t) = \frac{1}{2\pi}\frac{d\phi(t)}{dt}$. The IF, as a time-varying parameter, describes the location of the signal's spectral peak as it varies with time [18]. Much research has been carried out for estimating the IF of signals and various approaches have been proposed [18, 34, 35, 76, 77].

According to the Weierstrass approximation theorem [1], the phase $\phi(t)$ of the time-varying signal $x(t)$ can be approximated by a polynomial function on a closed and bounded interval if $\phi(t)$ is a continuous function of t. Therefore the general form of the Mth-order PPS is expressed as

$$s(t) = A(t)e^{j\phi(t)} = A(t)e^{j2\pi \sum_{m=0}^{M} a_m t^m}, \tag{2.2.2}$$

where the amplitude $A(t)$ is a constant or a real-valued stationary process. It can be easily seen that $s(t)$ becomes a harmonic signal when $M = 1$. When $M = 2$, $s(t)$ becomes a linear frequency modulated (LFM) signal, which is also called a chirp signal.

For a constant amplitude monocomponent PPS embedded in additive white

Gaussian noise (AWGN), the discrete signal model is given by

$$x(n) = Ae^{j2\pi \sum_{m=0}^{M} a_m \Delta^m n^m} + w(n), \quad n = 0, 1, \cdots, N-1 \tag{2.2.3}$$

where Δ is the sampling interval, which is assumed (without loss of generality) to be unit unless otherwise indicated in the rest of the thesis, and $w(n)$ is independent and identically distributed (i.i.d) sequence of complex Gaussian random variables with zero mean and variance σ^2. The unknown parameters are assumed to be the amplitude A and the phase parameters $a_0, a_1, \cdots, a_M$. For the unbiased mth-order phase parameter estimate $\hat{a}_m$, the Cramér-Rao lower bound (CRLB), which is the theoretical minimum variance of estimators for a deterministic parameter, is given as follows [78]

$$\begin{aligned} \mathrm{var}\{\hat{a}_m\} \geq\ & \frac{1}{8\pi^2 N(N\Delta)^{2m}\,\mathrm{SNR}} \left[\frac{1}{2m+1} + \frac{(M+1)^2}{2N(m+1)^2} - \frac{1}{2N} + O(N^{-2})\right] \\ & \cdot[(M+m+1)C_{M+m}^{m} C_{M}^{m}]^2, \end{aligned} \tag{2.2.4}$$

where $C_n^k = \frac{n!}{(n-k)!}$ is the binomial coefficient, and $\mathrm{SNR} = A^2/\sigma^2$ is the input SNR. It shows that the CRLB is approximately inversely proportional to the SNR, the number of measurements N, and the $2m$th power of the observation interval $N\Delta$. Interestingly, the CRLB is independent of the phase parameters a_m. Some special cases are given by

$$\begin{aligned} \mathrm{var}\{\hat{a}_0\} &\geq \left[1 + \frac{(M+1)^2 - 1}{2N} + O(N^{-2})\right] \frac{(M+1)^2}{8\pi^2 N\,\mathrm{SNR}} \\ \mathrm{var}\{\hat{a}_1\} &\geq \left[\frac{1}{3} + \frac{(M+1)^2 - 4}{8N} + O(N^{-2})\right] \frac{[M(M+1)(M+2)]^2}{8\pi^2 N(N\Delta)^2\,\mathrm{SNR}} \\ \mathrm{var}\{\hat{a}_M\} &\geq [1 + O(N^{-2})] \frac{(2M+1)(C_{2M}^{M})^2}{8\pi^2 N(N\Delta)^{2M}\,\mathrm{SNR}}\ . \end{aligned} \tag{2.2.5}$$

Multicomponent PPSs are also very common in a variety of applications, such as radar and mobile communications [21, 79, 80]. In these applications,

multiple targets, multiple paths or multicomponent interferences often occur. The number of components is equal to the number of targets in the radar application or to the number of multiple paths or interferences in the communication application. For an L-component PPS, the discrete signal can be expressed as

$$x(n) = \sum_{i=1}^{L} A_i(n) e^{j2\pi \sum_{m=0}^{M} a_{i,m} n^m} + w(n), \quad 0 \le n \le N-1, \qquad (2.2.6)$$

where the parameter $a_{i,m}$ is the phase coefficient, and the subscript i denotes the ith component. The definition of IF is meaningful only for monocomponent signals. For multicomponent signals, the signal can be viewed as a weighted sum of monocomponent signals, each one with its own IF [81].

2.3 Parameter Estimation of PPSs

In many applications, estimation of the PPS parameters is of significant importance since these parameters usually carry the desirable and relevant information. In inverse synthetic aperture radar (ISAR) imaging, for example, when the target has a rotational motion, its kinematic parameters can be modelled by the PPS [19]. To achieve a focused image of the target, polar reformatting is usually needed to allow the FT to be used properly. The knowledge of initial kinematic parameters of the target is needed to perform the polar reformatting. In synthetic aperture radar (SAR), there is an increasing demand for high resolution at low frequencies to recognize targets moving under various scenarios such as hidden by foliage [20]. In such a case, longer observation intervals are needed and the received signal should be modelled as higher-order PPS [21]. Furthermore, in the direct-sequence spread spectrum system, the performance will deteriorate significantly when the interference is broadband such as

the linear or nonlinear frequency modulated interference. Estimations of the phase parameters of the PPSs provide the information to detect and excise the interference [12, 13].

Tremendous research work has been done on the estimation of PPSs [21, 23, 34, 39, 40, 79, 82–90]. These reported approaches can be categorized as nonparametric methods and parametric methods. Nonparametric methods can employ the filter-based techniques such as the phase-locked loop (PLL), least mean square (LMS) and recursive least square (RLS) adaptive filters to track the phase of the signals [82–84]. However, these filter-based methods are unable to track very rapid changes in the IF. Moreover, the step size has to be adjusted a priori; otherwise, they may not converge to the true answer [18]. The time-frequency transforms can also be used as nonparametric methods to estimate the IF of the signals [34] and they have the advantages of providing time information about the variations of the IF of the analyzed signal. Their effectiveness to provide accurate estimates of the IF has been extensively investigated in the past decades [18, 34, 35, 60, 76]. The parametric methods are motivated by the Weierstrass approximation theorem to estimate the polynomial phase parameters. Compared with the nonparametric methods, the parametric methods provide inherently unlimited resolution and good noise rejection capability [91]. Generally, the parametric methods can be categorized into two classes, which are the suboptimal methods such as those based on high-order ambiguity function (HAF) [21, 23, 79, 85–88] and the maximum likelihood estimator based on the polynomial time frequency transform (PTFT) [39, 40, 89, 90].

2.3.1 Suboptimal Maximum Likelihood Methods

The high-order ambiguity function (HAF) is an efficient transform to estimate the parameters of PPSs [23, 79, 85, 86]. Among the suboptimal maximum likelihood methods, HAF-based estimation is the most popular candidate due to its computational efficiency. Given a sequence $x(n)$, the generalized Mth-order multi-lag high-order instantaneous moment (ml-HIM) is given recursively as [87]

$$\begin{aligned} x_1(n) &= x(n), \\ x_2(n;\boldsymbol{\tau}_1) &= x_1(n+\tau_1)x_1^*(n-\tau_1), \\ &\cdots \\ x_M(n;\boldsymbol{\tau}_{M-1}) &= x_{M-1}(n+\tau_{M-1};\boldsymbol{\tau}_{M-2})x_{M-1}^*(n-\tau_{M-1};\boldsymbol{\tau}_{M-2}), \end{aligned} \quad (2.3.1)$$

where $\boldsymbol{\tau}_{M-1} = [\tau_1, \tau_2, \cdots, \tau_{M-1}]$ is the vector containing all the lags for the Mth-order ml-HIM. The multi-lag HAF (ml-HAF) of the signal $x(n)$ is defined as the FT of the ml-HIM

$$X_M(f;\boldsymbol{\tau}_{M-1}) = \sum_{n=0}^{N-1} x_M(n;\boldsymbol{\tau}_{M-1})e^{-j2\pi fn}. \quad (2.3.2)$$

This definition of the ml-HIM, however, differs from the definitions in [23, 79, 85, 86] in two aspects: i) it does not assume that the lags τ_i are all equal to each other; ii) it is symmetric with respect to the lags. It means that the HAF given in [23, 79, 85, 86] is the special case of the ml-HAF, corresponding to the situation in which the lags are all equal to each other, i.e., $\boldsymbol{\tau}_{M-1} = (\tau, \tau, \cdots, \tau)$ and nonsymmetric definitions. It has been proved in [88] that the lag diversity introduces a redundancy which is then exploited to attenuate cross terms and spurious harmonics with respect to the useful terms. Furthermore,

the symmetric definition yields the same variance in the estimate of the highest order parameter but smaller variances for the estimates of all other parameters compared with the nonsymmetric definition. Therefore, the multi-lag symmetric definition is preferred.

The basic property is that the Mth-order ml-HIM can reduce a sampled Mth-order PPS into a single tone with frequency $f = 2^{M-1}M! \prod_{k=1}^{M-1} \tau_k a_M$. Thus, the estimation of the parameter a_M can be obtained by searching for the peak of the magnitude of (2.3.2), i.e.,

$$\hat{a}_M = \frac{1}{2^{M-1}M! \prod_{k=1}^{M-1} \tau_k} \arg\max_f \left| X_M(f; \boldsymbol{\tau}_{M-1}) \right|. \tag{2.3.3}$$

Once the highest order parameter $\hat{a}_M$ has been estimated, it can be removed from the signal $x(n)$ by multiplying $x(n)$ with $e^{-j2\pi \hat{a}_M n^M}$ to obtain a PPS of order $M-1$, where $\hat{a}_{M-1}$ can be estimated using the $(M-1)$th-order ml-HAF. The technique can then be iterated to estimate all the phase parameters up to the first order one.

Although the HAF is computationally efficient, it suffers from the noise-masking effects at low SNR and the cross terms in the presence of multicomponent signals due to its nonlinearity [79]. Moreover, it has been shown in [21, 88] that HAF-based methods suffer from an identifiability problem if multicomponent signals have the same highest order phase parameters. To overcome the identifiability problem and attenuate the cross terms, the product high-order ambiguity function (PHAF) was proposed in [21, 88]. Given L sets of lags $\boldsymbol{\tau}_{M-1}^{(l)} = (\tau_1^{(l)}, \tau_2^{(l)}, \cdots, \tau_{M-1}^{(l)})$ with $l = 1, 2, \cdots, L$, the PHAF is obtained as the

product of the ml-HAFs, properly scaled, i.e.,

$$X_M^L(f;T_{M-1}^L)=\prod_{l=1}^{L}X_M\left[\frac{\prod_{k=1}^{M-1}\tau_k^{(l)}}{\prod_{k=1}^{M-1}\tau_k^{(1)}}f;\boldsymbol{\tau}_{M-1}^{(l)}\right], \tag{2.3.4}$$

where $\tau_k^{(l)}$ indicates the kth component of the lth set, and T_{M-1}^L is the matrix containing all the sets of lags. The main property of the PHAF is that the locations of only the useful sinusoids are dependent with the lags, and the scaling operation aligns the useful sinusoids. In contrast, the peaks of the spurious sinusoids fall in different locations after scaling. In this way, the PHAF enhances the useful peaks and suppresses the spurious ones. In the monocomponent case, the PHAF has a lower SNR threshold than the HAF.

Several other algorithms have been proposed to improve the statistical performance including output SNR and asymptotic variance. For instance, the integrated generalized ambiguity function (IGAF) [87], an extension of the HAF-based methods, is defined by coherent integrations along each lag in the ml-HIM defined in (2.3.1). The IGAF estimates two phase parameters at each iteration as opposed to estimating one in the HAF-based methods, therefore it is more computationally intensive. Because of the coherent integrations, the IGAF can effectively suppress the cross terms. Therefore, the IGAF provides higher output SNR, which leads to a lower SNR threshold and a closer approach to the CRLB. It also provides a better capability of discriminating multicomponent signals. Moreover, the high-order phase function (HPF) [92, 93] has been introduced recently to estimate the parameters of a PPS. The advantage of the HPFs is that they always have lower orders of nonlinearities than the HAFs, therefore having a lower SNR threshold for effective analysis. For multicomponent PPS, the algorithm based on the generalized HPF is suggested in [94] by adopting a

similar idea of PHAF. A new and very broad generalization has been proposed in the form of the generalized multilinear function class [95]. The generalized multilinear function class subsumes many previously defined classes, including the HAF, the polynomial WVD, and the HPF. It also provides a framework for creating new class numbers for efficiently analyzing high-order PPS. Another interesting method [91] was proposed to use a "bottom-up" approach which first estimates the parameters associated with the lowest order instead of the highest order, based on the observation that the number of cross terms increases drastically with the order of HAF (PHAF).

However, it should be mentioned that the improvements on the output SNR and estimation variances of these reported methods are limited, especially for PPSs with high order and/or low input SNR. This is because these methods do not change the nonlinearity, which is the fundamental reason for the performance deterioration. Moreover, the recursive estimation structure will produce the error propagation phenomena.

2.3.2 Maximum Likelihood Method

Maximum likelihood estimation (MLE) is a popular method used for fitting a statistical model to data and providing estimates for the model's parameters. Compared with the HAF-based methods, the MLE provides higher output SNR without any SNR threshold and achieves better statistical performance which asymptotically approaches the CRLB [90, 96]. This is because that the MLE is implemented with a linear transform which is free from the cross terms. For the constant amplitude PPS embedded in AWGN, as defined in (2.2.3), the MLE

of the phase parameters and the amplitude are given by [89, 97]

$$\begin{aligned}\{\hat{a}_1, \hat{a}_2, \cdots, \hat{a}_M\} &= \arg\max_{\boldsymbol{\theta}} \left| \sum_{n=0}^{N-1} x(n) e^{-j2\pi \sum_{m=1}^{M} \theta_m n^m} \right|^2 \\ \hat{a}_0 &= \text{angle} \left(\sum_{n=0}^{N-1} x(n) e^{-j2\pi \sum_{m=1}^{M} \hat{a}_m n^m} \right) \\ \hat{A} &= \frac{1}{N} \left| \sum_{n=0}^{N-1} x(n) e^{-j2\pi \sum_{m=1}^{M} \hat{a}_m n^m} \right|, \end{aligned} \tag{2.3.5}$$

where $\boldsymbol{\theta} = \{\theta_1, \theta_2, \cdots, \theta_M\}$.

If the amplitude is random time-varying, it can be assumed to be a real-valued stationary process with any structure and independent of the AWGN. Accordingly the discrete signal model can be given by

$$x(n) = A(n) e^{j2\pi \sum_{m=0}^{M} a_m \Delta^m n^m} + w(n), \quad n = 0, 1, \cdots, N-1 \tag{2.3.6}$$

and the MLE of the phase parameters and the amplitude are expressed as follows [90]:

$$\begin{aligned}\{\hat{a}_1, \hat{a}_2, \cdots, \hat{a}_M\} &= \arg\max_{\boldsymbol{\theta}} \left| \sum_{n=0}^{N-1} x^2(n) e^{-j2\pi \sum_{m=1}^{M} 2\theta_m n^m} \right|^2 \\ \hat{a}_0 &= \frac{1}{2} \text{angle} \left(\sum_{n=0}^{N-1} x^2(n) e^{-j2\pi \sum_{m=1}^{M} 2\hat{a}_m n^m} \right) \\ \hat{A}(n) &= \frac{1}{N} \left| \sum_{n=0}^{N-1} x(n) e^{-j2\pi \sum_{m=1}^{M} \hat{a}_m n^m} \right|. \end{aligned} \tag{2.3.7}$$

2.3.2.1 Polynomial Time Frequency Transform (PTFT)

To obtain the MLE, $\boldsymbol{\theta} = \{\theta_1, \theta_2, \cdots, \theta_M\}$ needs to be digitized. Therefore, the Mth-order polynomial time frequency transform (PTFT) is defined as [39, 40]

$$\text{PTFT}(k_0, k_1, \cdots, k_{M-1}) = \sum_{n=0}^{N_0-1} y(n) W_{N_0}^{k_0 n} W_{N_1}^{k_1 n^2} \cdots W_{N_{M-1}}^{k_{M-1} n^M}, \tag{2.3.8}$$

where $W_N = e^{-j2\pi/N}$, $y(n) = x(n)$ for constant amplitude and $y(n) = x^2(n)$ for time-varying amplitude, $0 \le k_i \le N_i - 1$ for $i = 0, 1, \cdots, M-1$, and k_i/N_i is the discrete form of θ_{i+1}. For simplicity of presentation, let us define a demodulated sequence $y^{(d)}(n) = y(n) W_{N_1}^{k_1 n^2} \cdots W_{N_{M-1}}^{k_{M-1} n^M}$, then (2.3.8) can be expressed as

$$\mathrm{PTFT}(k_0, k_1, \cdots, k_{M-1}) = \sum_{n=0}^{N_0-1} y^{(d)}(n) W_{N_0}^{k_0 n}, \tag{2.3.9}$$

which means that the PTFT of $y(n)$ is equivalent to the discrete Fourier transform (DFT) of $y^{(d)}(n)$. Due to the property of DFT, sharp peaks appear in the PTFT if there exist sinusoidal signals in $y^{(d)}(n)$. This occurs when integer k_i for $i = 1, \cdots, M-1$ can take values satisfying $k_i/N_i \approx a_{i+1}$. Since the parameters $a_1, a_2, \cdots, a_M$ are estimated according to the defined grids, the performance of PTFT is influenced by the quantization errors δ_i, i.e., $\delta_i = a_{i+1} - k_i/N_i$, which can be controlled by the dimension size N_i. The frequency deviation caused by the quantization errors δ_i is assumed to be much smaller than the frequency of the sinusoidal component, which can be expressed as [39]

$$\left| \sum_{i=1}^{M-1} n^i \delta_i \right| \le \left| \sum_{i=1}^{M-1} n^i / (2N_i) \right| \ll |a_1| \le 0.5, \quad n = 0, \cdots, N_0 - 1, \tag{2.3.10}$$

since the maximum quantization error δ_i along the ith dimension is $1/(2N_i)$. Otherwise the peak may not be easily identified due to the quantization errors. Therefore we have

$$\sum_{i=1}^{M-1} \frac{N_0^i}{N_i} \ll 1, \tag{2.3.11}$$

which mean that for $1 \le i \le M-1$, $N_i \gg N_0^i$ is required to achieve a satisfactory accuracy for parameter estimation.

When the above constraint is satisfied the PTFT of a multicomponent PPS exhibits the same number of peaks as that of components in the PPS. For

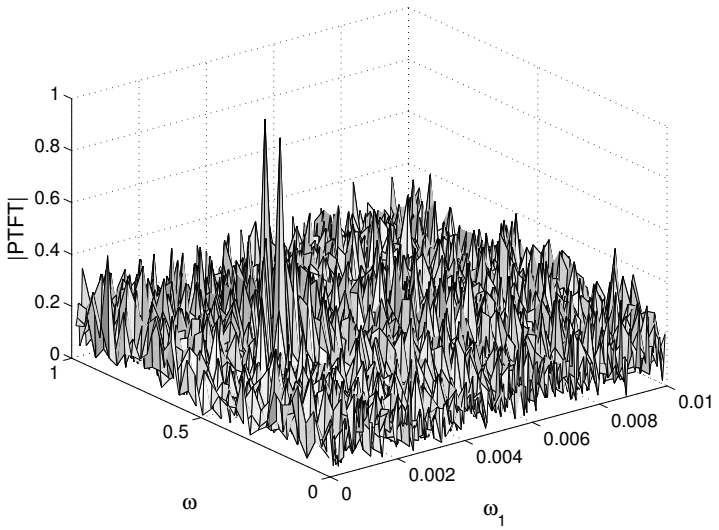

Figure 2.1: The PTFT of the sum of two second-order PPSs having the same amplitude (SNR = 0dB).

example, Figure 2.1 indicates that the second-order PTFT of a two-component PPS clearly shows the locations of two peaks even in the presence of AWGN with SNR = 0dB. From the location coordinates of the peaks, the parameters of the PPS can be estimated.

2.3.2.2 Advantages of the PTFT

Compared with the suboptimal estimation methods, such as the HAF, the PHAF and the IGAF, the most significant advantage of the maximum likelihood method based on the PTFT is that it is a linear transform with respect to the signal $x(n)$. This linear property is important since it makes the PTFT work well even at low SNRs and/or higher orders. The PTFT generally provides advantages in the following three aspects.

Firstly, the PTFT provides MLE of the PPS's phase parameters [90] and asymptotically approaches the CRLB [78]. In contrast, statistical analysis in [86]

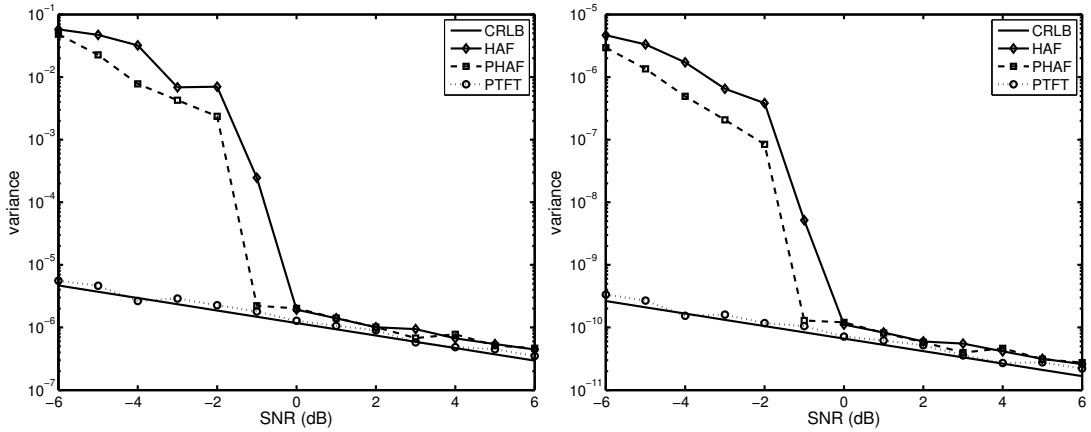

Figure 2.2: Comparison of variances of the estimates achieved using HAF, PHAF, PTFT and CRLBs, (a) $\hat{a}_1$ and (b) $\hat{a}_2$, versus SNR.

demonstrates that, although the asymptotic variances of estimates based on HAF are close to the CRLB for high SNR, they exhibit a consistent departure from the CRLB for low SNR and the deviation increases with the phase polynomial order. As shown in [88], although the PHAF can improve the performance of the HAF in the presence of noise, the estimation variances obtained from PHAF cannot reach the CRLB, that is due to the noise masking effects caused by the nonlinearity structure of the estimator. Therefore, the estimation based on the HAF or PHAF is comparable to that based on PTFT only when SNR is high and the phase polynomial order is small. The IGAF is a recursive approach that estimates two phase parameters at each iteration, and its performance falls between those of the maximum likelihood method and the HAF-based methods [87]. It is asymptotically efficient for the second order but loses the efficiency when the degree of the polynomial increases [87]. The following experiment is given to compare their performances. A second-order PPS corrupted by AWGN is considered, with the parameter $a_1 = 0.2$, $a_2 = 0.001$ and $N = 128$ samples. The numbers of the grids for computing HAF and PTFT are selected large

enough to keep the maximum quantization errors smaller than the root of the CRLB. For each value of the SNR, the variances of estimating a_1 and a_2 are obtained from 200 independent trials. The variations achieved using the HAF, PHAF (with L=3 sets), and PTFT are compared with the CRLBs [78] in Figure 2.2. It can be easily observed that the variances acquired by the PTFT are always closer to the CRLB than the HAF-based methods. The variances achieved from the HAF-based methods become close to the CRLB only when the SNR is greater than a threshold. When the SNR is smaller than the threshold, the performance degrades rapidly, which means the methods cannot work properly under this condition.

Secondly, the PTFT has a higher output SNR (SNR_{out}) than the HAF-based methods, especially when the input SNR (SNR_{in}) is low. The SNR_{out} is an important measurement of the estimator's sensitivity to noise [67, 87]. The relationship between the SNR_{in} and SNR_{out} of the PTFT has been derived in [98] as

$$\text{SNR}_{out} = N\,\text{SNR}_{in}, \tag{2.3.12}$$

which clearly shows that the ratio between SNR_{out} and SNR_{in} of the PTFT is a function of the number of samples and independent of the order M. The expressions of SNR_{out} of the IGAF and HAF are summarized in [87] and are given here for comparison. The expressions relative to the IGAF for the second-order and third-order PPSs are as follows

$$\text{SNR}_{out}^{(2)} = \frac{N^2\,\text{SNR}_{in}^2}{2N\,\text{SNR}_{in}+2} \tag{2.3.13}$$

and

$$\text{SNR}_{out}^{(3)} = \frac{10N^5\,\text{SNR}_{in}^4}{240N^2+960N^2\,\text{SNR}_{in}+450N^3\,\text{SNR}_{in}^2+81N^4\,\text{SNR}_{in}^3}. \tag{2.3.14}$$

The expressions relative to the HAF are given as

$$\mathrm{SNR}_{out}^{(2)} = \frac{N\,\mathrm{SNR}_{in}^2}{4\,\mathrm{SNR}_{in}+2} \tag{2.3.15}$$

and

$$\mathrm{SNR}_{out}^{(3)} = \frac{N\,\mathrm{SNR}_{in}^4}{6+24\,\mathrm{SNR}_{in}+33\,\mathrm{SNR}_{in}^2+18\,\mathrm{SNR}_{in}^3} \tag{2.3.16}$$

According to equations from (2.3.12) to (2.3.16), Figure 2.3 plots the SNR_{out} normalized with respect to the number of samples N as a function of SNR_{in}, i.e., SNR_{out}/N vs. SNR_{in}. The dashed, solid and dotted lines refer to the PTFT, IGAF and HAF respectively. From this figure, we can observe that: i) both IGAF and HAF exhibit the threshold effect, i.e., the output SNRs decrease drastically below a certain value of SNR_{in}. Moreover, the threshold effect becomes more evident as the polynomial orders increases; ii) the threshold of the IGAF decreases as the number of samples increases, while the HAF has a threshold that does not depend on the number of samples; iii) the PTFT is free from the threshold effect. Furthermore, for a given SNR_{in}, the PTFT has the highest SNR_{out} compared with the HAF-based methods.

Finally, since the PTFT estimates all the phase parameters simultaneously, it does not suffer from the error propagation which occurs in the recursive structures of the HAF, PHAF and IGAF algorithms. In addition, when dealing with multicomponent PPSs, the PTFT has no cross terms due to its linearity. In contrast, the cross terms generally exist in HAF, PHAF and IGAF algorithms due to their nonlinearity.

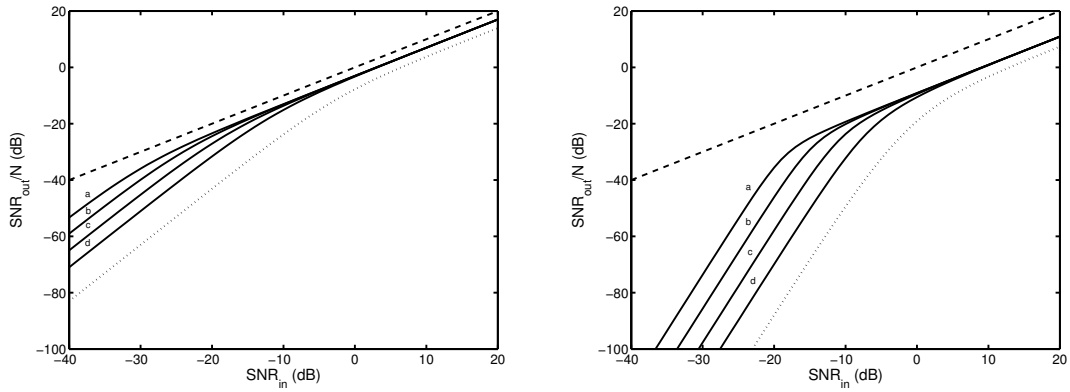

(a) (b)

Figure 2.3: The output SNR, normalized by N, versus input SNR for (a) second-order and (b) third-order PPS. Dashed line: PTFT, dotted line: HAF, and solid line: IGAF with (a) $N = 1024$, (b) $N = 256$, (c) $N = 64$, (d) $N = 16$.

2.3.2.3 Fast Algorithms for the PTFT

Although the PTFT can provide MLE for the phase parameters of PPSs, it generally requires a huge computation complexity due to the multi-dimensional calculation. Therefore fast algorithms for the PTFT are very important for practical applications. Some algorithms have been proposed to reduce the computational complexity, which will be reviewed as follows.

As shown in (2.3.9), the PTFT of $y(n)$ can be expressed as

$$\begin{aligned} \mathrm{PTFT}(k_0, k_1, \cdots, k_{M-1}) &= \sum_{n=0}^{N_0-1} y^{(d)}(n) W_{N_0}^{k_0 n} \\ &= \mathrm{DFT}_n[y^d(n)], \end{aligned} \tag{2.3.17}$$

where the subscript n indicates that the DFT is performed in terms of index n. Thus, the computation defined in (2.3.8) can be performed by using 1D DFT calculations, which is similar to the row-column method for the multi-dimensional DFTs. For an Mth-order PTFT of a length-N input sequence, $(\prod_{i=1}^{M-1} N_i)$ 1D length-N DFTs are required. Assuming the input sequence length N is a power

of two, with the help of the fast Fourier transform (FFT) [99], the PTFT can reduce its complexity from the order of $(\prod_{i=1}^{M-1} N_i)N^2$ to $(\prod_{i=1}^{M-1} N_i)N \log_2 N$, which is still difficult to support even with high speed processors.

To achieve a better computational efficiency, the fast quadratic phase transform [39] was proposed for the second-order PTFT. Compared with the FFT version of the PTFT, the fast quadratic phase transform can reduce the computational complexity by a factor $\log_2 N$. This work was extended to the third-order PTFT by exploiting the intrinsic symmetric properties of the PTFT [41]. It was further generalized to support an arbitrary order PTFT in [42], based on the decimation-in-time (DIT) decomposition technique, to reduce the overall computational complexity. For example, the numbers of complex multiplications and additions are reduced by a factor of $2^{M-1} \log_2 N$ for the Mth-order PTFT of length-N input sequence, compared with the algorithm that directly uses the 1D FFTs.

However, further reduction on computational complexity is still possible since some properties of the PTFT are not fully utilized. Recent work [43, 44] was reported to provide a significant computational saving for an arbitrary order PTFT. For example, a general fast algorithm for arbitrary order PTFTs is derived based on the split-radix concept [43], and a radix-2 decimation-in-frequency (DIF) fast algorithm for any order PTFTs was reported in [44] by using the periodic and symmetric properties of the PTFT.

It should be noted that these reported fast algorithms for PTFT [39, 41–44] only support sequence length being a power of two. When the sequence length is not supported by the available fast algorithms, however, zero padding techniques have to be employed to augment the input sequence to the next available

size supported by these fast algorithms. This mismatch surely wastes the computational resources and increases the computational complexity. Therefore fast algorithms based on various radix numbers for other sequence lengths are also highly desired. Based on radix-3 decomposition techniques, fast algorithms for the PTFT of any order is presented in [45]. By combining other factors in the sequence lengths, it can be used to efficiently support many different sequence lengths. The fast algorithms are further generalized for computing the PTFT of length $a^p b$, where a, b and p are positive integers [46]. The periodic and symmetric properties of the PTFT are effectively used to minimize the computational complexity. By assigning values of a, b, and p, various algorithms, for example, radix-a and split-radix-2/(2a) are presented to provide the flexibility supporting PTFTs of various sequence lengths. Similarly, fast algorithms for computing the PTFT that deals with a real-valued sequence of length $a^p b$ are investigated in [47]. Since the PTFT has a conjugate symmetric property for real-valued input sequence, the corresponding fast algorithms can effectively reduce the computational complexity compared to the fast algorithms for complex-valued sequences.

2.4 Time-Frequency Representations

From a mathematical point of view, a given signal can be described in many different ways. In the time domain representation, it is shown how signal magnitude changes over time. Frequency domain is another most important representation. One widely used frequency representation is the Fourier transform (FT), which tells us the distribution of the frequencies and their amplitudes. However, the spectrum obtained via the FT does not tell us when those fre-

quencies occur or vanish. In many practical applications, it is far more useful to characterize the signal in time and frequency domain simultaneously, which is the time-frequency representations (TFRs).

The fundamental idea of the TFRs is to describe how the frequency content of a signal changes in time, so that we can deal with the time-varying signal more accurately. As shown in Figure 2.4, the plot at the bottom of the figure is the time waveform of the bat sound which can be downloaded from [100]. The plot on the left is the standard power spectrum from the FT. From the spectrum alone, however, we cannot tell how those frequencies evolve over time. The main plot is the time-dependent spectrogram, a function of both time and frequency, which clearly reveals the frequency characteristics of the signal. From this plot, we can not only tell how the frequency changes, but also see the intensity of the frequencies shown by the relative brightness levels of the plot. Consequently, by using the TFRs, the information in the frequency domain can be more accurately revealed.

TFRs have been used in many practical applications. In radar imaging, due to the complex motion of a target, the Doppler frequency shifts are generally time-varying. By using the Fourier transform to retrieve Doppler information, the Doppler spectrum becomes smeared and the image is blurred. The TFRs can be used to replace the Fourier transform as a means of radar image reconstruction, and the blurred image due to complex motion can be refocused without polar reformatting [25]. In image and audio watermarking, when the linear chirps are embedded as watermark signal, the detection of this kind of watermark can be performed by the TFRs [6, 7]. The TFRs significantly improve the performance of the watermark detection process and can be combined with other

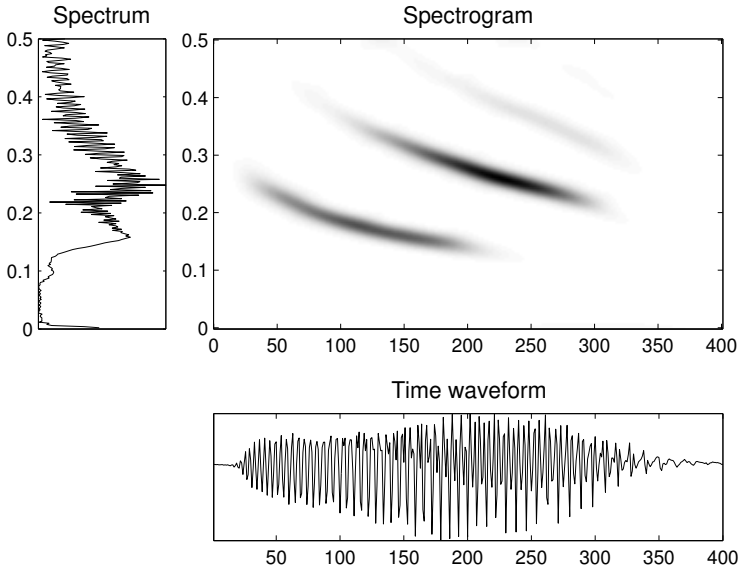

Figure 2.4: The time waveform, spectrum, and TFR of the bat sound data.

existing watermark embedding/extraction algorithms for increased robustness. In the spread spectrum communications, the TFRs are used for nonstationary interference excision with improved bit error ratio (BER) performance [27, 28]. Moreover, the TFRs provide interesting approaches to mathematically analyze music, identify patterns in the time-frequency structure of music at multiple time scales, and provide insight into the nature of music [29, 30]. The TFRs are employed to provide time-frequency structures of the sounds produced by different musical instruments [31]. These time-frequency structures correlate well with our perceptions of the sounds and their differences produced by these instruments. The advantages of TFRs can also be found in radar target detection [26], speech signal processing [32, 101] and biomedical signal processing [3, 4, 33].

There are various types of TFRs. Each type has its individual advantages and disadvantages. Generally speaking, it is not possible to have a particular

TFR that is suited to all possible applications. The choice of a TFR depends on the specific application at hand [34–36] to best use the available properties of the TFR. Performance criteria for the TFRs are introduced in [102]. For a monocomponent signal, performance of the TFRs can be measured in terms of the energy concentration that the TFR approaches to the signal IF. To improve the concentration, we need to minimize the sidelobe amplitude relative to mainlobe amplitude, and to minimize mainlobe bandwidth about the signal IF. For a multicomponent signal, performance of the TFR can be analyzed by not only the energy concentration of each component but also the resolution, which is measured by the minimum frequency separation between the components' mainlobes where their amplitudes and bandwidths are preserved. Resolution measure criteria was introduced in [103], which takes into account key attributes of TFRs, such as components' mainlobes, sidelobes and cross terms. The introduction of this measure allows to quantify the quality of TFRs instead of relying solely on visual inspection of their plots in the time-frequency domain.

2.4.1 Short-time Fourier Transform (STFT)

The most popular linear TFR is the STFT due to its simple concept and easy implementation. The basic idea behind STFT is straightforward. As shown in Figure 2.5 [60], at each time instant t_0, the spectrum is represented by the FT of a small segment of the signal $x(t)$ around t_0. For the signal $x(t)$, the STFT is defined as

$$\mathrm{STFT}(x;t,\omega) = \int_{-\infty}^{\infty} x(t+\tau)h^*(\tau)e^{-j\omega\tau}d\tau, \tag{2.4.1}$$

where $h(\tau)$ is the window function of finite sequence length. For simplicity in the rest of the thesis, the integral without limits implies that the integration is from $-\infty$ to ∞. Since the STFT is a linear transform, it is free from the cross terms that appear in many nonlinear TFRs.

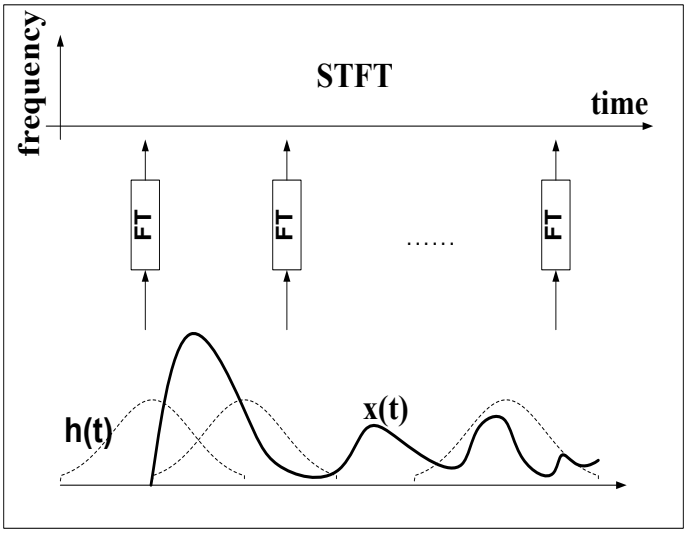

Figure 2.5: Illustration of the STFT.

The STFT is widely used because of its easy implementation and linearity property. It has been used for many practical applications such as speech pitch and format analysis [32], interference excision in spread spectrum communications [28], fingerprint enhancement [104] and onset detection in music signals [105].

Nevertheless, the basic assumption of the STFT is that the frequencies in each signal segment are not changed with time so that the Fourier transform can be used to analyze the frequency characteristics. In this way, the frequency variations with time are approximately described by the Fourier transforms of the successive signal segments. Because the basic assumption mentioned above is not generally true, however, the resolution of the STFT in the time-frequency

domain is often limited. Moreover, it should be noted that the time resolution and frequency resolution of the STFT are limited by the uncertainty principle [34]. With a time-limited window function, the resolution of the STFT is determined by the window size. A larger window has a higher time resolution but lower frequency resolution; a smaller window has a higher frequency resolution but lower time resolution.

In most applications, such as the instantaneous frequency estimation which arises in a variety of applications including FM demodulation [106] and non-stationary interference excision in direct sequence spread spectrum communications [28], high resolution is desired. Therefore, some forms of adaptive STFT are presented to get a better resolution for the signals [106–109]. The STFTs with different window lengths are computed at different time instances. The window used at each time instance, which can be decided according to the adaptation criteria such as concentration measurement [106] and maximum correlation rule [108], should be matched to the signal characteristics of that instance, therefore increasing the resolution of the STFT. To reduce the computational complexity, the STFTs with different window lengths can be computed in a recursive way [28, 107].

2.4.2 Nonlinear TFRs

2.4.2.1 Quadratic TFRs: Wigner-Ville distribution (WVD), ambiguity function (AF) and Cohen's class

The WVD is defined as the FT of the product function $x(t+\tau/2)x^*(t-\tau/2)$ with respect to τ,

$$\mathrm{WVD}(x;t,\omega) = \int x(t+\tau/2)x^*(t-\tau/2)e^{-j\omega\tau}d\tau, \tag{2.4.2}$$

which is obtained by performing the Fourier transform with respect to the variable τ.

By performing the Fourier transform with respect to the variable t, we obtain another popular time-frequency representation called the ambiguity function (AF), i.e.,

$$\mathrm{AF}(x;\theta,\tau) = \int x(t+\tau/2)x^*(t-\tau/2)e^{j\theta t}dt. \tag{2.4.3}$$

The ambiguity function has been widely used in the context of radar and sonar. It has a close relationship with the WVD as

$$\mathrm{WVD}(x;t,\omega) = \frac{1}{2\pi}\int\int \mathrm{AF}(x;\theta,\tau)e^{-j(\omega\tau-\theta t)}d\theta d\tau, \tag{2.4.4}$$

which indicates that the WVD is a double Fourier transform of the ambiguity function.

The WVD satisfies a large number of desirable mathematical properties [34]. For example, it is always real-valued, preserves time and frequency shifts, satisfies the marginal properties, and also provides the optimal concentration for LFM signals. Despite all these desirable properties, the WVD suffers from the cross terms due to its nonlinearity when multicomponent signals are considered.

Since the cross terms often make the interpretation of the results difficult, the reduction of the cross terms becomes an important issue. Many alternatives, such as pseudo WVD (PWVD), smoothed pseudo WVD (SPWVD) [60], and reduced interference distribution (RID) [110], have been proposed to suppress the undesired cross terms. In general, these solutions are to use various windows to filter out the oscillating cross terms. With fewer cross terms, these modified WVDs have been used in many applications, such as analysis of the biological signals [110] and the radar imaging [111]. Although these modified methods can substantially suppress the cross terms, the smoothing operation will destroy many of the desirable properties of the WVD.

Generally, these variations, together with the WVD, constitute the Cohen's class defined by

$$\begin{aligned} C(x;t,\omega) &= \frac{1}{4\pi^2}\int\int\int x(u+\tau/2)x^*(u-\tau/2)\phi(\theta,\tau)e^{-j\theta t-j\tau\omega+j\theta u}dud\tau d\theta \\ &= \frac{1}{4\pi^2}\int\int \phi(\theta,\tau)\mathrm{AF}(x;\theta,\tau)e^{-j\theta t-j\tau\omega}d\tau d\theta \end{aligned} \tag{2.4.5}$$

where $\phi(\theta,\tau)$ is the kernel function. This indicates that a quadratic TFR is obtained from a two-dimensional filtering in the ambiguity domain. The properties of the TFRs in this class can be readily known by simply examining the kernel function $\phi(\theta,\tau)$.

The S-method is another technique proposed to suppress the cross terms [72]. It performs well when the components are well separated and its performance deteriorates if the signal components overlap in the time-frequency domain [112].

2.4.2.2 High-order TFRs – Polynomial WVD

As we introduced, the WVD provides optimal concentration for a LFM signal in the time-frequency domain, that is, it can yield delta function around the instantaneous frequency (IF) for the LFM signal. However, for nonlinear FM signals the optimal concentration cannot be obtained and some artifacts may occur to hide the real feature of the signals. This limitation motivates the design of the polynomial WVD [113], which is an extension of the WVD. The polynomial WVD is defined as

$$W_x^{(M)}(t,\omega) = \int \prod_{m=1}^{M/2} x(t+d_m\tau)x^*(t+d_{-m}\tau)e^{-j\omega\tau}d\tau, \tag{2.4.6}$$

to exhibit delta functions around the signal IF for polynomial FM signals. The order M of the polynomial WVD is an even integer which indicates the order of nonlinearity of the polynomial WVD, whereas d_m and d_{-m} are real coefficients. The realness of the polynomial WVD results in $d_m = -d_{-m}$. The optimal energy concentration of the polynomial WVD enables it to be used for estimation of the IF of polynomial FM signals. Its performance as an IF estimator is evaluated in the presence of additive white Gaussian noise [77] and impulsive noise [114]. The design of higher order polynomial WVD and the selection criteria for the optimal set of kernel coefficients are discussed in [115].

Due to its nonlinearity, the polynomial WVD suffers from the cross terms when it is used to analyze multicomponent signals. The number of cross terms increases very rapidly with the order of the polynomial WVD [77]. Moreover, when it is used as the IF estimator, the polynomial WVD performs well at high SNR but suffers from threshold effects at low SNR [116].

2.4.3 Local Polynomial Fourier Transform (LPFT)

Recently the local polynomial Fourier transform (LPFT) [38] was developed as a high-order generalization of the STFT. It was reported to provide high resolution for time-varying signals with a local polynomial function approximating to the IF characteristic of the analyzed signals. To realize the local polynomial function approximation, the LPFT introduces polynomial parameters including the first order derivative and other higher order derivatives of the IF of the analyzed signal. The form of the LPFT is as follows [38],

$$\begin{aligned} \mathrm{LPFT}(x;t,\varpi) &= \mathrm{LPFT}(x;t,\omega,\omega_1\cdots\omega_{M-1}) \\ &= \int x(t+\tau)h(\tau)e^{-j\theta(\tau,\varpi)}d\tau, \end{aligned} \tag{2.4.7}$$

where

$$\begin{aligned} \theta(\tau,\varpi) &= \omega\tau+\omega_1\tau^2/2+\cdots+\omega_{M-1}\tau^M/M!, \\ \varpi &= (\omega,\omega_1,\cdots,\omega_{M-1}), \end{aligned}$$

and M is the order of the LPFT. The local polynomial periodogram (LPP) is defined as

$$\mathrm{LPP}(x;t,\varpi) = \left|\mathrm{LPFT}(x;t,\varpi)\right|^2. \tag{2.4.8}$$

When $M=1$, the LPFT and LPP become the STFT and spectrogram, respectively.

The LPFT has found applications in many areas. For instance, it has been used for improvement of the radar images in cases of fast maneuvering targets [50, 51] and for nonstationary interference suppression in noise radar systems [117]. It is useful for interference suppression in communication systems to achieve performance improvement in comparison with that obtained from the

systems based on the STFT [52, 53]. In [118], a new form of beamformer based on the LPFT is derived for source localization and tracking in nonstationary environment, which can resolve closely spaced sources provided that their velocities are sufficiently different. Motion parameters in video sequences, such as the velocity and acceleration, can be estimated using the LPFT [10]. Moreover, the LPFT can be used as an IF estimator, and the corresponding asymptotic covariance matrix and bias of the estimates are studied in [38, 49]. The concept of the LPFT is also implemented for the polynomial WVD to produce high signal concentration along the IF [119], and it is also extended to the L-Wigner distribution in [120].

For the LPFT, the corresponding form of Parseval's theorem can be written as [119]

$$\frac{1}{2\pi}\int |\mathrm{LPFT}(x;t,\varpi)|^2\, d\omega = \int |x(t+\tau)h(\tau)|^2\, d\tau, \tag{2.4.9}$$

which indicates that the LPFT can be interpreted as a time-frequency energy distribution over the $t-\boldsymbol{\omega}^0(t)$ space, where $\boldsymbol{\omega}^0(t) = [\Omega(t), \Omega^{(1)}(t), \cdots, \Omega^{(m-1)}(t)]^T$ is a vector of the true values of the IF $\Omega(t)$ and its derivatives. The energy concentration of $\mathrm{LPFT}(t,\boldsymbol{\omega})$ in $\boldsymbol{\omega}^0(t)$ for the time instant t is illustrated in [38, 49].

The principal difference between the LPFT and the quadratic and high-order TFRs has been discussed in [38]. The LPFT is linear with respect to the signal and uses the polynomial function, $\theta(\tau,\varpi)$, in the complex exponent (or the transform kernel). On the other hand, quadratic and higher degree polynomials of the signals are used with the exponential function $e^{-j\omega\tau}$ in TFRs, wherein the argument of the exponent is linear with respect to variable τ. Due to its linearity, the LPFT can be inversed to reconstruct the original signal by

integrating the LPFT over ω, that is

$$x(t) = \frac{1}{2\pi h(0)} \int \mathrm{LPFT}(x; t, \varpi) d\omega. \tag{2.4.10}$$

It has been shown in [74] that for a LFM signal $s(t) = Ae^{j(a_0 t + \frac{b_0}{2} t^2)}$ the corresponding second-order LPFT is

$$|\mathrm{LPFT}(s; t, \omega)| = A\sqrt{\frac{2\pi}{|\omega_1 - b_0|}} \exp\left\{ j \frac{(\omega - a_0 - b_0 t)^2}{4(\omega_1 - b_0)} \right\} * H(\omega), \tag{2.4.11}$$

where $*$ is the convolution in the frequency domain and $H(\omega)$ is the Fourier transform of the window function $h(t)$. Therefore the second-order LPFT is concentrated along the instantaneous frequency of the LFM signal, $\omega = a_0 + b_0 t$, for $\omega_1 = b_0$. The fractional Fourier transform (FRFT), a generalization of the FT, is another method that can concentrate LFM signals. Its definition is expressed as [121]

$$\mathrm{F}_\alpha(u) = \begin{cases} \sqrt{\frac{1 - j\cot\alpha}{2\pi}} e^{j(u^2/2)\cot\alpha} \int x(t) e^{j(t^2/2)\cot\alpha - jut\csc\alpha} dt, & \alpha \neq n\pi, \\ x(t), & \alpha = 2n\pi, \\ x(-t), & \alpha = (2n+1)\pi. \end{cases} \tag{2.4.12}$$

The FT is a special case of the FRFT with the rotation angle $\alpha = \frac{\pi}{2}$. For M=2, $\omega = u\csc\alpha$ and $\omega_1 = \cot\alpha$ in (2.4.7), the FRFT can be expressed in terms of the second-order LPFT as

$$F_\alpha(u) = \sqrt{\frac{1 - j\cot\alpha}{2\pi}} e^{j(u^2/2)\cot\alpha} \mathrm{LPFT}(x; t, \omega, \omega_1), \tag{2.4.13}$$

therefore the LPFT provides a broad generalization of the FRFT [36].

The LPFT is computationally demanding because it is based on the PTFT estimation which involves calculating a multi-dimensional function and finding

the maximum of the multi-dimensional function. To decrease calculation burden, the second-order LPFT with point-wise chirp rate parameter estimation was proposed as [50, 74]

$$\mathrm{LPFT}_{\alpha(t)}(x;t,\omega) = \int x(t+\tau)h^*(\tau)e^{-j\alpha(t)\tau^2/2}e^{-j\omega\tau}d\tau, \quad (2.4.14)$$

where $\alpha(t)$ is time-varying chirp parameters, which can be estimated by

$$\hat{\alpha}(t) = \arg\max_{\alpha\in\Lambda} H(\alpha,t), \quad (2.4.15)$$

where Λ is a set of values of considered chirp rate parameters, and $H(\alpha,t)$ is the concentration measure discussed in [122, 123]. For signals with multiple components, another efficient method known as the modified LPFT was introduced in [48]. It can be approximately viewed as the sum of the LPFT of each component. It is computed through the following steps:

- use a window function to divide the signal into a number of segments, and model each segment as an Mth-order PPS;
- estimate the phase parameters of each segment using the PTFT;
- compute LPFT with the estimated parameters and selected window length.

The length of overlap between two consecutive segments controls the computation load as well as the smoothness of the spectrum. It has been shown in [48] that the LPFT with no overlap can still yield satisfactory performance if the window length is small enough. In this way, the computational complexity can be greatly reduced. More details on the application of the LPFT can be found in [48]. Since the computation complexity of the LPFT increases with the order of the PPS, processing higher order PPSs with lower order LPFT is another way to reduce the computational complexity. It should be noted that for

higher-order PPSs, the second-order LPFT can employ a small window length to ensure that each segment within the window can be assumed to be a chirp signal. In this way, the second-order LPFT, which is particularly suitable to process the LFM signals, can also be used to process higher-order signals with time-varying frequencies, which will be shown later.

Compared with the nonlinear transforms such as the WVD, the LPFT is free from the cross terms due to its linearity [38]. Moreover, theoretically the LPFT can provide high resolution for PPSs if the extra parameters required by the LPFT computation are properly estimated and updated [38]. In general, accurate estimation of parameters can be easily obtained by using the PTFT [39, 40] to achieve a high resolution of the time-frequency representation. Therefore, the LPFT is a nonparametric method which has strong links with both nonparametric methods and the parametric estimators of the polynomial phase [49]. To further explore the theoretical analysis and applications of the LPFT, as well as to further improve the concentration for the LPP, will be the theme of this thesis.

Chapter 3

Uncertainty Principle of the LPFT

3.1 Introduction

The uncertainty principle plays an important role in signal processing [54] as well as in physics [124]. For the Fourier transform, generally speaking, the more concentrated the signal is, the more spread out its Fourier transform must be. It is impossible to arbitrarily concentrate both a function and its Fourier transform. This trade-off can be formalized in the form of the uncertainty principle. Similarly, the STFT is also limited by the uncertainty principle [34]. Based on the uncertainty principle, it is understood that a shorter window used to capture the signal segment leads to a poor resolution in the frequency domain to represent the signal, and vice verse. It is not possible to arbitrarily increase the resolution in both domains at the same time. Literatures [125, 126] and the references therein can be referred to about the review on the uncertainty

principle.

Studies on the uncertainty principle of various transforms have been reported in the literature. It was addressed in [55] that the time-frequency transforms of the Cohen's class are affected by some fundamental properties such as the marginal property, the energy conservation property, and the Moyal's relation. Each of these properties implies a restriction on the signal concentration in the time-frequency domain and is thus related to the uncertainty principle. The local uncertainty product of the spectrogram and a large class of bilinear time-frequency distributions were considered in [56], and the uncertainty principle of local quantities was demonstrated to show that the local uncertainty product is always less than or equal to the global uncertainty product. The uncertainty principle for real signals in the domain of fractional Fourier transform (FRFT) was investigated in [57], and a tighter lower bound than that reported in [127] was derived on the product of the signal spreads in the time and FRFT domains. The logarithmic, Heisenberg's and short-time uncertainty principles associated with the FRFT were recently presented in [128], and it was shown that the uncertainty principles continue to hold for these transforms involving the FRFT parameter. Two entropic uncertainty principles in FRFT domains, i.e., Shannon entropy uncertainty principle and Rényi entropy uncertainty principle, were recently derived in [129] and were generalized for multiple functions and discrete case as well. Similarly, the uncertainty principle for real signals in the linear canonical transform (LCT) domain was derived in [58] to give a tighter lower bound than that given in [121]. The uncertainty principle for complex signals in the LCT domain were derived in [130], and the tighter lower bound for real signals in [58] was also proven to hold for arbitrary LCT parameters based on the properties of moments for the LCT.

It has been observed that the resolution of the LPFT in the time-frequency domain is also influenced by the window size which controls the trade-off of bias and variance [38, 49]. A data-driven approach based on the intersection of confidence intervals (ICI) was proposed in [131] to solve the problem of window size selection. The window size is considered as a parameter of estimation and a number of estimates are calculated for a set of values of this parameter. Then, the ICI rule is used for selection of the estimate with the best window size, therefore obtaining a varying adaptive window size selection optimizing the local accuracy of estimation. Note that when nonsymmetric rectangular window is used and the signal is corrupted by AWGN, the LPP estimator coincides with the maximum likelihood estimator mentioned in Section 2.3.2. It is believed that there must exist some form of the uncertainty principle based on the LPFT. However, a comprehensive study on the uncertainty principle for an arbitrary order LPFT has not been reported in the literature.

The definition of the LPFT has been given in Chapter 2 and is rewritten here for the convenience of the readers. The Mth-order LPFT is expressed as [38]:

$$\begin{aligned} &\mathrm{LPFT}(t,\omega,\omega_1\cdots\omega_{M-1}) \\ &= \int s(t+\tau)h(\tau)\exp\left\{-j\omega\tau - j\sum_{m=2}^{M}\frac{\omega_{m-1}\tau^m}{m!}\right\}d\tau, \\ &= \int s(\tau)\exp\left\{j\omega t - j\sum_{m=2}^{M}\frac{\omega_{m-1}(\tau-t)^m}{m!}\right\}h(\tau-t)\exp\left\{-j\omega\tau\right\}d\tau, \end{aligned} \tag{3.1.1}$$

where M is the order of the polynomial function, $\omega_1 = \frac{d\Omega(t)}{dt}$, $\omega_2 = \frac{d^2\Omega(t)}{dt^2}$, ..., and $\omega_{M-1} = \frac{d^{M-1}\Omega(t)}{dt^{M-1}}$ are the polynomial parameters, and $\Omega(t)$ is the instantaneous frequency of the signal.

The LPFT is particularly suited to process the polynomial-phase signals

(PPSs) with a Gaussian amplitude defined by

$$s(t) = (\frac{a}{\pi})^{1/4} \exp\left\{-\frac{at^2}{2}\right\} \exp\left\{j \sum_{m=1}^{P} \frac{a_{m-1} t^m}{m!}\right\}, \tag{3.1.2}$$

where P is the order of the PPSs. To compute the LPFT in (3.1.1), the polynomial parameters ω_1, ω_2, ..., ω_{M-1} are first estimated using the polynomial time frequency transform (PTFT) [39, 40] and then used to form the polynomial phase, as shown in (3.1.1). The LPFT is obtained by using an STFT procedure whose input is obtained by modulating $s(\tau)$ with $\exp\left\{j\omega t - j \sum_{m=2}^{M} \frac{\omega_{m-1}(\tau-t)^m}{m!}\right\}$.

When M, the order of the LPFT, is large, one practical problem is that the corresponding PTFT requires a heavy computational load even using the fast algorithms reported in Section 2.3 of Chapter 2. Based on the radix-2 fast algorithm for the PTFT [44] and the fast Fourier transform (FFT) algorithm [99] for the STFT computation, the number of complex multiplications needed by the LPFT is approximately

$$C_{LPFT}(N) \simeq \left[C^r_{PTFT}(q) + \frac{q}{2}\log_2 q + 0.75q\right] \frac{N}{q-l}, \tag{3.1.3}$$

where N is the length of the input signal, q is the length of the window (or signal segment), and l, $1 \leq l \leq q-1$, is the length of overlap between signal segments. In (3.1.3), $C^r_{PTFT}(q)$ is the number of complex multiplications needed by the rth-order PTFT of length q, the second term in the square bracket is the number of complex multiplications for an FFT of length q, the third term in the square bracket is the number of complex multiplications for windowing and modulation operations, and the factor outside the square bracket is approximately the number of the signal segments used for the LPFT. It was reported that for the rth-order PTFT of length N, where $r = 2$ or 3, the required number

of complex multiplications are in the order of N^r [44],

$$C^2_{PTFT}(N) = \frac{13}{64}N^2 - \frac{3}{2}N + 1, \quad (3.1.4)$$

$$C^3_{PTFT}(N) = \frac{31}{1536}N^3 - \frac{7}{6}N + 1, \quad (3.1.5)$$

which means that the PTFT requires a heavy computational complexity, especially when N is large. Therefore it is important to find various methods to minimize the computational complexity for the parameter estimations by using the PTFT. Similar to the concept of the STFT which uses Fourier transform to deal with the time-varying signal, we can use a smaller number of the polynomial parameters in the LPFT to approximate the frequency contents of the signal segments. If the second-order LPFT is used to process higher-order PPSs, as shown in [48, 74], for example, the number of polynomial parameters to be estimated is reduced, which directly leads to the reduction of the PTFT order, or equivalently the required computational complexity. We will discuss the side effects of this order mismatch, i.e., the order of the LPFT is smaller than the order of the PPSs, on the resolution of the signal representation in the time-frequency domain. Other practical issues, which also exist in the STFT, including the effects of window width and the length of overlap between adjacent signal segments, will be discussed. The computational complexity can be significantly reduced if the overlap length can be minimized without obviously degrading the resolution of the time-frequency representation. The effects of estimation errors of the polynomial parameters are also to be observed in this chapter.

This chapter firstly reports the mathematical derivations of the uncertainty principles of the second, third, fourth-order and thereafter Mth-order LPFTs. It is found that the uncertainty product of an arbitrary order LPFT is related

to the parameters of the signal and the window function, as well as the errors of estimating the polynomial parameters. When the polynomial parameters of the transform kernel are accurately estimated, the uncertainty product becomes a constant when a Gaussian window is used to segment the input signal. Based on the derived signal duration and bandwidth, from which the uncertainty product is obtained, we then discuss the effects, in terms of the resolution in the time-frequency domain and the minimization of the required computational complexity, of window width, order mismatch, i.e., using the second-order LPFT to process higher-order PPSs, and the length of overlap between signal segments. Comparisons are also made on the resolutions of signal representations in the time-frequency domain achieved by using the STFT, the Wigner-Ville distribution (WVD) and the second-order LPFT.

The rest of the chapter is organized as follows. After the review on the terminologies used in deriving the uncertainty principle of the STFT in Section 3.2, the uncertainty principles of the LPFTs of different orders are given in Section 3.3. Section 3.4 discusses the effects of various issues on obtaining desirable signal representations in the time-frequency domain. Signal concentrations of different time-frequency representations are also compared. Conclusions are given in Section 3.5. Finally the mathematic derivation of the uncertainty product of the Mth-order LPFT, with the parameters correctly estimated, is given in Appendix in Section 3.6.

3.2 Review on the Uncertainty Principle of STFT

We will consider the Pth-order PPS defined in (3.1.2) as the input signal. By multiplying $s(t)$ with a window function $h(t)$, the local signal is defined as $s_t(\tau) = s(\tau)h(t-\tau)$. It is easily seen that the Fourier transform of the local signal $s_t(\tau)$ is exactly the STFT of the original signal $s(t)$. The normalized local signal at time t is

$$\eta_t(\tau) = \frac{s(\tau)h(\tau - t)}{\sqrt{\int |s(\tau)h(\tau - t)|^2 d\tau}}, \tag{3.2.1}$$

which ensures that for any t, $\int |\eta_t(\tau)|^2 d\tau = 1$. We will review some terminologies based on the normalized local signal $\eta_t(\tau)$ [34] which is a function of τ within a short duration, and its Fourier transform is defined as

$$F_t(\omega) = \int \eta_t(\tau) \exp\{-j\omega\tau\} d\tau,$$

to reveal the spectral information around the time instant t. For this normalized local signal, all the relevant quantities, such as the mean time, duration, mean frequency and bandwidth, are time dependent [34].

The mean time of the normalized local signal is defined as

$$\begin{aligned} \langle \tau \rangle_t &= \int \tau |\eta_t(\tau)|^2 d\tau \\ &= \frac{\int \tau |s(\tau)h(\tau - t)|^2 d\tau}{\int |s(\tau)h(\tau - t)|^2 d\tau}, \end{aligned} \tag{3.2.2}$$

and its duration, or signal spread in time, is defined as

$$\begin{aligned} T_t^2 &= \int (\tau - \langle \tau \rangle_t)^2 |\eta_t(\tau)|^2 d\tau \\ &= \langle \tau^2 \rangle - \langle \tau \rangle_t^2, \end{aligned} \tag{3.2.3}$$

where $\langle \tau^2 \rangle$ is the second-order moment of the normalized local signal, defined as

$$\langle \tau^2 \rangle = \int \tau^2 |\eta_t(\tau)|^2 d\tau.$$

Similarly, the nth-order moment of the normalized local signal is defined as

$$\langle \tau^n \rangle = \int \tau^n |\eta_t(\tau)|^2 d\tau.$$

The mean frequency of the normalized local signal is defined as

$$\begin{aligned} \langle \omega \rangle_t &= \int \omega |F_t(\omega)|^2 d\omega \\ &= \int \eta_t^*(\tau) \frac{1}{j} \frac{d}{d\tau} \eta_t(\tau) d\tau, \end{aligned} \tag{3.2.4}$$

and its bandwidth, or signal spread in frequency, is

$$\begin{aligned} B_t^2 &= \int (\omega - \langle \omega \rangle_t)^2 |F_t(\omega)|^2 d\omega \\ &= \langle \omega^2 \rangle - \langle \omega \rangle_t^2, \end{aligned} \tag{3.2.5}$$

where

$$\langle \omega^2 \rangle = \int \omega^2 |F_t(\omega)|^2 d\omega = -\int \eta_t^*(\tau) \frac{d^2 \eta_t(\tau)}{d\tau^2} d\tau. \tag{3.2.6}$$

The duration T_t^2 and bandwidth B_t^2 are good measures of the broadness of the local signal in the time and frequency domains, respectively. For example, T_t^2 (or B_t^2) of a signal means the squared width of the signal concentrated around the mean time $\langle \tau \rangle_t$ (or mean frequency $\langle \omega \rangle_t$). The uncertainty product in the STFT domain is generally a function of time, the signal $s(t)$ and the window $h(t)$, and has a lower bound [34]

$$B_t^2 T_t^2 \geq \frac{1}{4}.$$

It should be noted that the focus of this chapter is on the uncertainty product obtained by multiplying the duration and bandwidth of the local signal. It is important to understand that this uncertainty product places limits on the processing techniques of the windowed transforms. Other kinds of uncertainty products, such as the global uncertainty products, can be referred to [59].

3.3 Uncertainty Principles of the LPFTs

Based on the definitions given in the previous section, this section first presents the uncertainty principles for the lower order, i.e., $M = 2$, 3 and 4, LPFTs. Then, a general expression of the uncertainty principle for the Mth-order LPFT is deduced. It is assumed that the input signals are PPSs with the same orders of the LPFTs, i.e., M in (3.1.1) is equal to P in (3.1.2). The corresponding normalized local signal is

$$\eta_t(\tau) = \frac{s(\tau)h(\tau - t)\exp\left\{j\omega t - j\sum\limits_{m=2}^{M}\frac{\omega_{m-1}(\tau-t)^m}{m!}\right\}}{\sqrt{\int |s(\tau)h(\tau - t)|^2 d\tau}}, \tag{3.3.1}$$

where

$$h(t) = \left(\frac{\alpha}{\pi}\right)^{1/4}\exp\left\{-\frac{\alpha t^2}{2}\right\}, \tag{3.3.2}$$

is a Gaussian window used to obtain the signal segments and $\alpha > 0$ is the parameter to control the window width.

With the above defined input signal and the window function, the normalization factor, i.e., the integral in the denominator of (3.3.1), becomes

$$\int |s(\tau)h(\tau - t)|^2 d\tau = \left(\frac{a\alpha}{\pi(a+\alpha)}\right)^{1/2}\exp\left\{-\frac{a\alpha t^2}{a+\alpha}\right\}. \tag{3.3.3}$$

Therefore, the normalized local signal is expressed as

$$\eta_t(\tau) = \left(\frac{\alpha+a}{\pi}\right)^{1/4} \exp\left\{-\frac{\alpha^2 t^2}{2(\alpha+a)} - \frac{(\alpha+a)\tau^2}{2} + \alpha\tau t + j\sum_{m=1}^{P}\frac{a_{m-1}t^m}{m!}\right\} \cdot \exp\left\{j\omega t - j\sum_{m=2}^{M}\frac{\omega_{m-1}(\tau-t)^m}{m!}\right\}. \tag{3.3.4}$$

For an arbitrary order PPS, it is easy to derive

$$|\eta_t(\tau)|^2 = \left(\frac{\alpha+a}{\pi}\right)^{1/2} \exp\left\{-(\alpha+a)(\tau - \frac{\alpha t}{\alpha+a})^2\right\}, \tag{3.3.5}$$

which is independent of the order of the PPS. With (3.2.2), the mean time, $\langle\tau\rangle_t$, of the normalized local signal becomes

$$\langle\tau\rangle_t = \frac{\alpha t}{a+\alpha}.$$

Similarly, we also obtain

$$\langle\tau^2\rangle = \frac{1}{2(a+\alpha)} + \frac{\alpha^2 t^2}{(a+\alpha)^2}. \tag{3.3.6}$$

Therefore the duration defined in (3.2.3), or the signal spread in time, of the normalized local signal is expressed as

$$T_t^2 = \frac{1}{2(a+\alpha)}. \tag{3.3.7}$$

Since both $\langle\tau\rangle_t$ and T_t^2 are related to $|\eta_t(\tau)|$ instead of $\eta_t(\tau)$, they are independent of the order of the input signal. It means that the signal duration in the time domain is determined by the signal parameter α and window parameter a only.

We will compute the mean frequency $\langle\omega\rangle_t$ and the bandwidth B_t for the LPFTs of various orders. For the second-order LPFT, the local signal is

$$s_t(\tau) = s(\tau)h(\tau-t)\exp\left\{j\omega t - j\frac{\omega_1(\tau-t)^2}{2}\right\}, \tag{3.3.8}$$

where $s(t)$, the input of the second-order LPFT, is the second-order PPS, or the chirp signal, obtained by setting $P = 2$ in (3.1.2), and ω_1 is estimated by using the second-order PTFT. In this case, the Fourier transform of the local signal $s_t(\tau)$ becomes the second-order LPFT of $s(t)$.

The normalized local signal for $P = 2$ in (3.3.4) at the time t becomes

$$\begin{aligned}\eta_t(\tau) &= \frac{s(\tau)h(\tau-t)\exp\left\{j\omega t - j\frac{\omega_1(\tau-t)^2}{2}\right\}}{\sqrt{\int |s(\tau)h(\tau-t)|^2 d\tau}} \\ &= \left(\frac{\alpha+a}{\pi}\right)^{1/4}\exp\left\{-\frac{(\alpha+a)\tau^2}{2} + \alpha\tau t + ja_0\tau + \frac{ja_1\tau^2}{2} - \frac{\alpha^2t^2}{2(\alpha+a)}\right\} \\ &\quad \cdot\exp\left\{j\omega t - \frac{j\omega_1(\tau-t)^2}{2}\right\}.\end{aligned}$$

With the definition in (3.2.4), we have

$$\begin{aligned}\langle\omega\rangle_t &= a_0 + \omega_1 t + \frac{\alpha t(a_1-\omega_1)}{a+\alpha} \\ &= a_0 + \omega_1 t + (a_1-\omega_1)\langle\tau\rangle_t, \end{aligned} \tag{3.3.9}$$

in which the first term is related to the signal parameter a_0, the second term is related to ω_1, and the last term is a product of the deviation of ω_1 from a_1 and the mean time $\langle\tau\rangle_t$. Similarly, by using (3.2.6), we have

$$\langle\omega^2\rangle = \frac{a+\alpha}{2} + \langle\omega\rangle_t^2 + \frac{1}{2(a+\alpha)}(a_1-\omega_1)^2, \tag{3.3.10}$$

which shows that the frequency variance is determined by the parameters of the signal and the window in the first term, the square of mean frequency in the second term, and the scaled square of the estimation error of the polynomial parameter ω_1 in the last term. With the above derivation results, the bandwidth in the domain of the second-order LPFT becomes

$$\begin{aligned}B_t^2 &= \langle\omega^2\rangle - \langle\omega\rangle_t^2 \\ &= \frac{a+\alpha}{2} + \frac{(a_1-\omega_1)^2}{2(a+\alpha)}. \end{aligned} \tag{3.3.11}$$

Therefore

$$B_t^2 T_t^2 = \frac{1}{4} + \frac{(a_1 - \omega_1)^2}{4(a+\alpha)^2}, \tag{3.3.12}$$

which is related to the parameters of the signal and the window, and the errors of estimating the polynomial parameters ω_1.

Next we will consider the uncertainty principle of the third-order LPFT. The local signal is

$$s_t(\tau) = s(\tau)h(\tau - t)\exp\left\{j\omega t - j\frac{\omega_1}{2}(\tau - t)^2 - j\frac{\omega_2}{6}(\tau - t)^3\right\},$$

where $s(t)$, the input of the third-order LPFT, is the third-order PPS obtained by setting $P = 3$ in (3.1.2).

In this case, the local normalized signal becomes

$$\begin{aligned}\eta_t(\tau) &= \left(\frac{\alpha + a}{\pi}\right)^{1/4} \exp\left\{j\omega t - \frac{j\omega_1(\tau - t)^2}{2} - \frac{j\omega_2(\tau - t)^3}{6}\right\} \\ &\quad \cdot \exp\left\{-\frac{(\alpha + a)\tau^2}{2} + \alpha\tau t + ja_0\tau + \frac{ja_1\tau^2}{2} + \frac{ja_2\tau^3}{6} - \frac{\alpha^2 t^2}{2(\alpha + a)}\right\}.\end{aligned} \tag{3.3.13}$$

With the same procedure, the mean frequency defined in (3.2.4) is expressed as

$$\langle\omega\rangle_t = a_0 + \omega_1 t - \frac{\omega_2 t^2}{2} + (a_1 - \omega_1 + \omega_2 t)\langle\tau\rangle_t + \frac{1}{2}(a_2 - \omega_2)\langle\tau^2\rangle, \tag{3.3.14}$$

and $\langle\omega^2\rangle$ defined in (3.2.6) becomes

$$\begin{aligned}\langle\omega^2\rangle &= \frac{a + \alpha}{2} + \langle\omega\rangle_t^2 \\ &\quad + \frac{1}{2(a+\alpha)}[(a_1 - \omega_1 + \omega_2 t) + (a_2 - \omega_2)\langle\tau\rangle_t]^2 + \frac{(a_2 - \omega_2)^2}{8(a+\alpha)^2}.\end{aligned} \tag{3.3.15}$$

Thus, the bandwidth becomes

$$\begin{aligned}B_t^2 &= \langle\omega^2\rangle - \langle\omega\rangle_t^2 \\ &= \frac{a + \alpha}{2} + \frac{1}{2(a+\alpha)}[(a_1 - \omega_1 + \omega_2 t) + (a_2 - \omega_2)\langle\tau\rangle_t]^2 + \frac{(a_2 - \omega_2)^2}{8(a+\alpha)^2}.\end{aligned} \tag{3.3.16}$$

Therefore

$$B_t^2 T_t^2 = \frac{1}{4} + \frac{1}{4(a+\alpha)^2}\left[(a_1 - \omega_1 + \omega_2 t) + (a_2 - \omega_2)\langle\tau\rangle_t\right]^2 + \frac{(a_2-\omega_2)^2}{16(a+\alpha)^3}. \tag{3.3.17}$$

It is observed that the uncertainty product, $B_t^2 T_t^2$, is affected by the errors of estimating the polynomial parameters ω_1 and ω_2 in addition to the parameters of the signal and the window function.

By setting $P = 4$ in (3.1.2) and using the fourth-order LPFT, we can similarly obtain the corresponding mean frequency, $\langle\omega\rangle_t$, and the bandwidth, B_t, which are listed in Table 3.1, respectively. From the expressions in Table 3.1, we can observe the rules of $\langle\omega\rangle_t$ and B_t^2 as M, the order of the LPFT, is increased. The mean frequency and the bandwidth for the Mth-order LPFT are

$$\begin{aligned}\langle\omega\rangle_t &= a_0 + \sum_{m=2}^{M}\frac{(-1)^m \omega_{m-1} t^{m-1}}{(m-1)!} \\ &\quad + \sum_{n=1}^{M-1}\frac{1}{n!}\left(a_n + \sum_{m=n+1}^{M}\frac{(-1)^{m-n}\omega_{m-1}t^{m-n-1}}{(m-n-1)!}\right)\langle\tau^n\rangle, \qquad (3.3.18)\\ B_t^2 &= \frac{a+\alpha}{2} + \sum_{l=1}^{M-1}\frac{1}{2^l l!(a+\alpha)^l} \\ &\quad \cdot\left[\sum_{n=l}^{M-1}\frac{1}{(n-l)!}\left(a_n + \sum_{m=n+1}^{M}\frac{(-1)^{m-n}\omega_{m-1}t^{m-n-1}}{(m-n-1)!}\right)\langle\tau^{n-l}\rangle\right]^2. \qquad (3.3.19)\end{aligned}$$

It is observed that both $\langle\omega\rangle_t$ and B_t^2 are related to the moments $\langle\tau^n\rangle$.

In general the uncertainty product of an arbitrary order LPFT is related to the parameters of the signal and the window function, as well as the errors of estimating the polynomial parameters. When the polynomial parameters are estimated correctly for the Mth-order LPFT, that is, $\omega_1 = \frac{d\Omega(t)}{dt}$, ..., $\omega_{M-1} =$

Table 3.1: Expressions of $\langle\omega\rangle_t$ and B_t^2 for LPFTs of order 2, 3 and 4

M	$\langle\omega\rangle_t$
2	$a_0+\omega_1 t+(a_1-\omega_1)\langle\tau\rangle_t$
3	$a_0+\omega_1 t-\frac{\omega_2 t^2}{2}+(a_1-\omega_1+\omega_2 t)\langle\tau\rangle_t+\frac{1}{2}(a_2-\omega_2)\langle\tau^2\rangle$
4	$a_0+\omega_1 t-\frac{\omega_2}{2}t^2+\frac{\omega_3}{6}t^3+(a_1-\omega_1+\omega_2 t-\frac{\omega_3}{2}t^2)\langle\tau\rangle_t$ $+\frac{1}{2}(a_2-\omega_2+\omega_3 t)\langle\tau^2\rangle+\frac{1}{6}(a_3-\omega_3)\langle\tau^3\rangle$
	B_t^2
2	$\frac{a+\alpha}{2}+\frac{1}{2(a+\alpha)}(a_1-\omega_1)^2$
3	$\frac{a+\alpha}{2}+\frac{1}{2(a+\alpha)}[(a_1-\omega_1+\omega_2 t)+(a_2-\omega_2)\langle\tau\rangle_t]^2+\frac{1}{8(a+\alpha)^2}(a_2-\omega_2)^2$
4	$\frac{a+\alpha}{2}+\frac{1}{2(a+\alpha)}[(a_1-\omega_1+\omega_2 t-\frac{\omega_3}{2}t^2)+(a_2-\omega_2+\omega_3 t)\langle\tau\rangle_t$ $+\frac{1}{2}(a_3-\omega_3)\langle\tau^2\rangle]^2+\frac{1}{8(a+\alpha)^2}[(a_2-\omega_2+\omega_3 t)+(a_3-\omega_3)\langle\tau\rangle_t]^2$ $+\frac{1}{48(a+\alpha)^3}(a_3-\omega_3)^2$

$\frac{d^{M-1}\Omega(t)}{dt^{M-1}}$, the mean frequency becomes

$$\begin{aligned}\langle\omega\rangle_t &= a_0+a_1 t+\frac{a_2}{2}t^2+\ldots+\frac{a_{M-1}}{(M-1)!}t^{M-1}\\ &= \sum_{m=1}^{M}\frac{a_{m-1}t^{m-1}}{(m-1)!}\end{aligned}\tag{3.3.20}$$

which is exactly the instantaneous frequency of the Mth-order PPS. The bandwidth in the domain of the Mth-order LPFT becomes $B_t^2=\frac{a+\alpha}{2}$, which leads to the uncertainty product as

$$B_t^2T_t^2=\frac{1}{4}.\tag{3.3.21}$$

The uncertainty principle for the Mth-order LPFT, with the parameters correctly estimated, is mathematically proved in Appendix in Section 3.6.

Based on the above derived results, we have the following conclusions. When using the Gaussian window to segment the signal, the signal duration of the PPS is related to the signal parameter a and the window parameter α only and is independent of the order. For $M>1$, the bandwidth B_t is related to the parameters of the signal and the window function, as well as the errors of estimating

the polynomial parameters ω_1, ω_2, ... , and ω_{M-1}. When the polynomial parameters are estimated accurately, the uncertainty product of the Mth-order LPFT, with the same order PPS as the input, is independent of time or frequency, and becomes a constant. When there are errors of estimating the polynomial parameters, the bandwidth together with the uncertainty product, are polynomial functions of these errors, which directly affect the signal representation in the time-frequency domain.

3.4 Discussions

The main objective on studying various issues of the LPFT is to achieve the desired signal concentration in the time-frequency domain with minimum computational costs. This section considers a few important issues, in terms of the uncertainty principles of the LPFTs, that have direct impact on signal concentration and the required computational complexity.

3.4.1 Window Width Effects

The uncertainty products derived in the previous section show that there exists a trade-off between the resolutions in the time and frequency domains. With the assumption that the polynomial parameters used in the LPFT are accurately estimated, the signal duration T_t^2 is inversely proportional to the sum of window width α and the signal parameter a. Meanwhile the signal bandwidth B_t^2, which is independent of the order of the PPS and the LPFT, is directly proportional to the sum of window width α and the signal parameter a.

With different widths of the Gaussian window, Figure 3.1 shows the sig-

nal concentrations in the time-frequency domain achieved by using the second-order LPFT to process the PPS which contains chirp components. As defined in (3.1.3), the length of the input signal is N and the window length is q. It

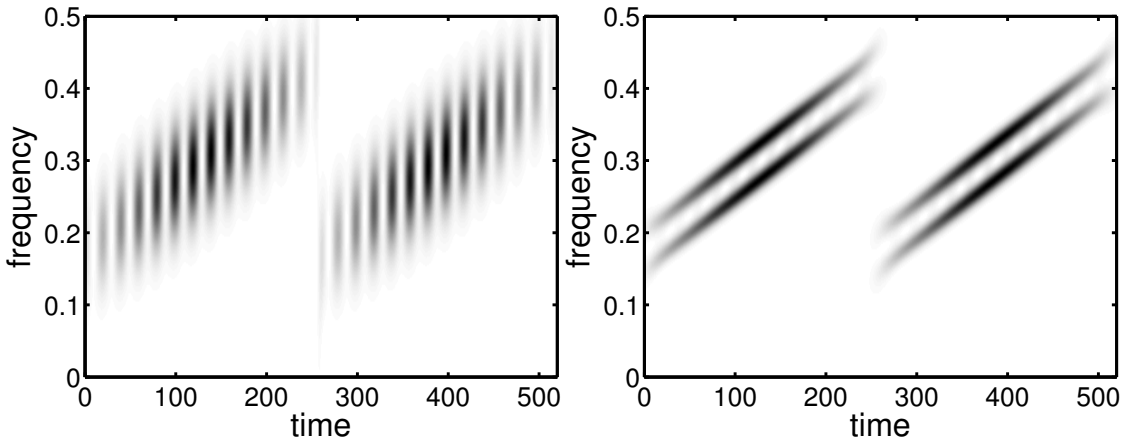

(a) α=25 (b) α=5

(c) α=2.5 (d) α=0.25

Figure 3.1: The second-order LPFTs of a second-order multicomponent PPS, with different α values. Here $q = \frac{N}{4}$, where q is the window length and N is the length of the input signal.

is seen that, as α decreases or the window width increases, the chirp components become more concentrated in the frequency direction, or equivalently, the resolution of the signal representation in the frequency direction is increased. As for the resolution in the time direction, the signal in Figure 3.1(a) can be

clearly separated in different time index. As the parameter α decreases, such separation in time direction disappears. Therefore from Figure 3.1(a) to (d) we can observe that the resolution in the time direction decreases as the parameter α decreases. This observation is consistent with the signal duration T_t^2 and the bandwidth B_t^2 derived in the last Section. For example, decreasing the window parameter α leads to the increase of the signal duration T_t^2, or equivalently, the increase of signal spread in time. At the same time, the bandwidth B_t^2 decreases as α decreases so that the signal spread in frequency is reduced. That is, the resolution of the signal representation in the frequency direction is increased. Because it is impossible to arbitrarily increase the resolution in both domains at the same time, a compromise has to be made to balance the requirements of the signal representation in the time-frequency domain. When $\alpha = 2.5$ which is the default value in MATLAB Gaussian window function, for example, Figure 3.1(b) provides acceptable resolutions for both time and frequency domains.

3.4.2 Order Mismatch Effects

It is desired to use lower order LPFTs to deal with higher-order PPSs to significantly reduce the required computational complexity. However, this mismatch between the orders of the LPFT and the PPSs will affect the performance of the signal representation in the time-frequency domain. It is necessary to find out how the signal representation in the time-frequency domain is affected and if possible, how the mismatch effects are to be minimized. First we will consider the use of the second-order LPFT to process the third-order PPSs.

By setting $\omega_2 = 0$ in (3.3.14) and (3.3.16), the mean frequency and the

bandwidth become

$$\begin{aligned}\langle\omega\rangle_t &= a_0+\omega_1 t+(a_1-\omega_1)\langle\tau\rangle_t+\frac{1}{2}a_2\langle\tau^2\rangle \\ &= a_0+\omega_1 t+\frac{\alpha t(a_1-\omega_1)}{a+\alpha}+\frac{a_2(2\alpha^2t^2+a+\alpha)}{4(a+\alpha)^2},\end{aligned}$$

$$B_t^2 = \frac{a+\alpha}{2}+\frac{1}{2(a+\alpha)}\left[(a_1-\omega_1)+\frac{a_2\alpha t}{a+\alpha}\right]^2+\frac{a_2^2}{8(a+\alpha)^2}.$$

When the parameter ω_1 is estimated correctly, i.e., $\omega_1 = a_1 + a_2 t$, we have

$$\langle\omega\rangle_t = a_0+a_1t+\frac{a_2t^2}{2}+\frac{a^2a_2t^2}{2(a+\alpha)^2}+\frac{a_2}{4(a+\alpha)}, \tag{3.4.1}$$

$$B_t^2 = \frac{a+\alpha}{2}+\frac{(a_2at)^2}{2(a+\alpha)^3}+\frac{a_2^2}{8(a+\alpha)^2}. \tag{3.4.2}$$

Therefore, the uncertainty product becomes

$$B_t^2T_t^2 = \frac{1}{4}+\frac{1}{4(a+\alpha)^2}\left(\frac{a_2at}{a+\alpha}\right)^2+\frac{a_2^2}{16(a+\alpha)^3}. \tag{3.4.3}$$

In (3.4.1) and (3.4.2), the last two terms are the effects of the order mismatch, which are directly proportional to the polynomial parameter, a_2. Therefore, the order mismatch may have a small effect when a_2 is small enough, which is generally true in many practical applications. Another way to reduce the effect of the order mismatch is to decrease the window width, that is to increase the window parameter α. For example, when $\alpha \to \infty$, $\langle\omega\rangle_t$ in (3.4.1) is approaching to $a_0 + a_1 t + \frac{a_2}{2}t^2$, which is the instantaneous frequency of the third-order PPS. Meanwhile B_t^2 in (3.4.2) is approaching to $\frac{a+\alpha}{2}$. It means that, when the third-order PPS is processed with the second-order LPFT, $\langle\omega\rangle_t$ and B_t^2 of the second-order LPFT approach to those of the third-order LPFT as the window width is decreased. The uncertainty product in (3.4.3) also approaches to the minimum.

When the signal parameter a approaches to zero, the third-order PPS with a Gaussian amplitude becomes a third-order PPS with a constant amplitude. Under this situation, the mean frequency and bandwidth become

$$\begin{aligned} \langle\omega\rangle_t &= a_0 + a_1 t + \frac{a_2 t^2}{2} + \frac{a_2}{4\alpha}, \\ B_t^2 &= \frac{\alpha}{2} + \frac{a_2^2}{8\alpha^2}. \end{aligned} \tag{3.4.4}$$

Since

$$T_t^2 = \frac{1}{2(a+\alpha)},$$

the uncertainty product is

$$B_t^2 T_t^2 = \frac{1}{4} + \frac{a_2^2}{16\alpha^3} \qquad \text{as } a \longrightarrow 0, \tag{3.4.5}$$

which increases with the polynomial parameter a_2 and decreases with the window parameter α. Similarly, as α goes to infinity, $\langle\omega\rangle_t$ approaches to the instantaneous frequency, and $B_t^2 T_t^2$ approaches to $\frac{1}{4}$ which is the minimum of the uncertainty product.

Although it is difficult to draw a general conclusion for all possible cases, the order mismatch effect of using the second-order LPFT to process the Mth-order PPSs can be expressed as follows.

By setting $\omega_2 = \omega_3 = ... = \omega_{M-1} = 0$ in (3.3.18) and (3.3.19), the mean frequency and the bandwidth become

$$\begin{aligned} \langle\omega\rangle_t &= a_0 + \omega_1 t - \omega_1\langle\tau\rangle_t + \sum_{n=1}^{M-1} \frac{a_n}{n!}\langle\tau^n\rangle \\ &= a_0 + \omega_1 t + (a_1 - \omega_1)\langle\tau\rangle_t + \sum_{n=2}^{M-1} \frac{a_n}{n!}\langle\tau^n\rangle, \end{aligned}$$

$$\begin{aligned} B_t^2 &= \frac{a+\alpha}{2} + \frac{1}{2(a+\alpha)}(a_1 - \omega_1)^2 \\ &\quad + \sum_{l=2}^{M-1} \frac{1}{2^l \cdot l!(a+\alpha)^l}\Big[\sum_{n=l}^{M-1} \frac{1}{(n-l)!} a_n \langle\tau^{n-l}\rangle\Big]^2. \end{aligned}$$

and thus

$$B_t^2 T_t^2 = \frac{1}{4} + \frac{1}{2(a+\alpha)^2}(a_1 - \omega_1)^2 + \sum_{l=2}^{M-1} \frac{1}{2^l \cdot l!(a+\alpha)^{l+1}} [\sum_{n=l}^{M-1} \frac{1}{(n-l)!} a_n \langle \tau^{n-l} \rangle]^2.$$

Therefore as α goes to infinity, $\langle \omega \rangle_t$ approaches to the instantaneous frequency, and $B_t^2 T_t^2$ approaches to $\frac{1}{4}$ which is the minimum of the uncertainty product.

From the above discussion, it is seen that increasing the window parameter α always helps to achieve a better estimation of the instantaneous frequency $\langle \omega \rangle_t$. It should be noted that, however, as α goes to infinity, that is as the window becomes narrower in the time domain, the signal bandwidth B_t^2 in (3.4.4) also approaches to infinity, which decreases the resolution in frequency. Therefore, the window width for practical applications should be properly selected to achieve a compromise between the resolutions in time and frequency.

3.4.3 Effects of Overlap Lengths

It was shown in [48] that when the second-order LPFT is used to process the chirp signals, the length of overlap between the adjacent signal segments can be significantly reduced without obviously degrading the signal concentration in the time-frequency domain, which allows us to further minimize the required computational complexity. For example, the required number of complex multiplications in (3.1.3) is reduced as the length of overlap l increases. For the

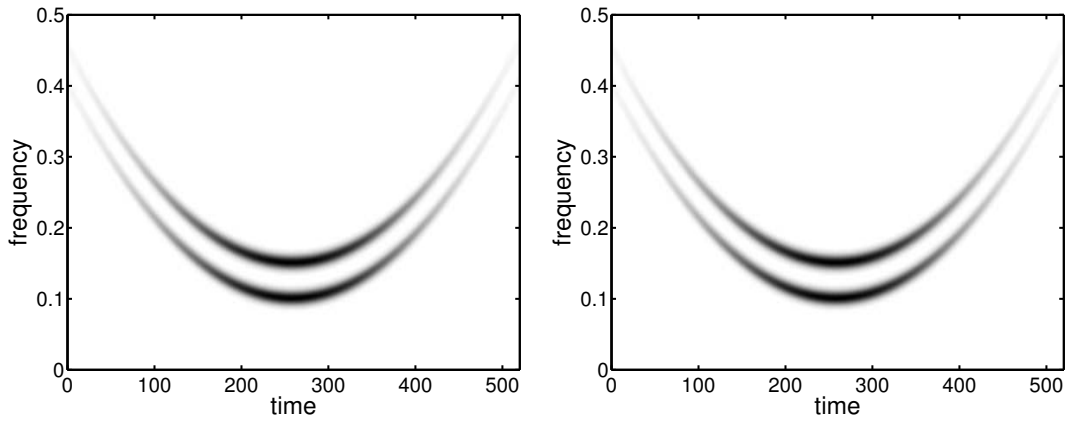

(a) LPFT without overlap (b) LPFT with the maximum overlap

Figure 3.2: The third-order LPFTs of a third-order PPS using Gaussian window function with α=2.5 and $q = \frac{N}{4}$, where q is the window length and N is the length of the input signal.

third-order PPS,

$$s(t) \tag{3.4.6}$$
$$= \left(\frac{a}{\pi}\right)^{1/4} e^{-at^2/2}[e^{j(0.4t+1.15\times10^{-3}t^2+1.48\times10^{-6}t^3)} + e^{j(0.45t+1.15\times10^{-3}t^2+1.48\times10^{-6}t^3)}]$$

with $a = 10^{-4}$, Figure 3.2(a) shows the signal representation obtained by the third-order LPFT without any overlap. Compared with the performance with the maximum overlap, i.e., $l = q-1$, as shown in Figure 3.2(b), no obvious degradation in signal concentration is observed from Figure 3.2(a). Because the total computational complexity is directly proportional to the number of signal segments being processed, the LPFT computation without overlap between signal segments makes significant savings on the computational complexity compared to that using the overlap between signal segments.

Next we will consider the effects of using lower order LPFT with different overlap lengths. Figure 3.3(a) shows the representation of the third-order PPS obtained by using the second-order LPFT without any overlap. Obvious unsmoothness is observed at the junctions of two adjacent segments where the

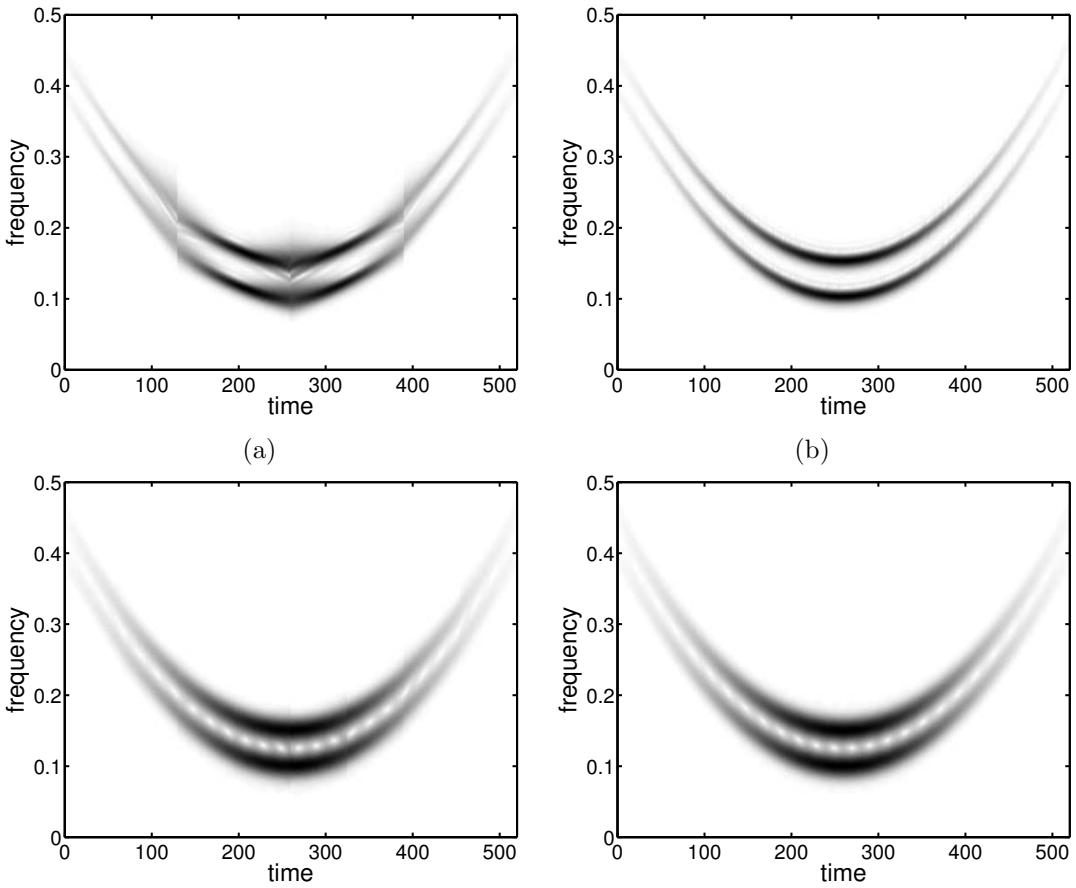

Figure 3.3: The LPFTs of the third-order PPS using Gaussian window function with α=2.5 (a) the second-order LPFT without overlap, (b) the second-order LPFT with the maximum overlap, (c) the second-order LPFT without overlap and with a shorter window length $q = \frac{N}{8}$, and (d) the third-order LPFT without overlap. $q = \frac{N}{4}$ in (a) and (b), and $q = \frac{N}{8}$ in (c) and (d).

estimated chirp rates have sudden changes. This order mismatch effect can be minimized by increasing the length of overlap between the adjacent segments. As shown in Figure 3.3(b), the second-order LPFT with the maximum overlap achieves a representation that is comparable to that obtained by using the third-order LPFT in Figure 3.2(b).

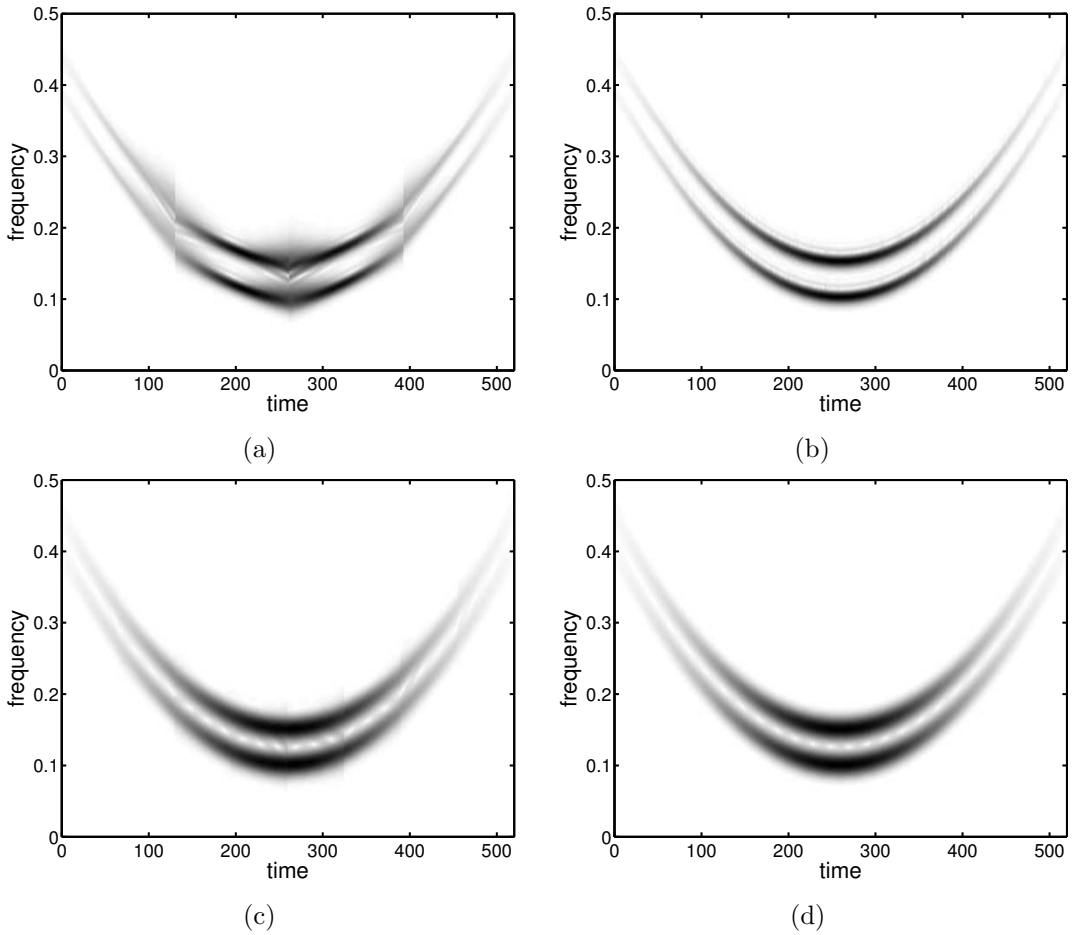

Figure 3.4: The LPFTs of the third-order PPS using Hamming window function (a) the second-order LPFT without overlap, (b) the second-order LPFT with the maximum overlap, (c) the second-order LPFT without overlap and with a shorter window length $q = \frac{N}{8}$, and (d) the third-order LPFT without overlap. $q = \frac{N}{4}$ in (a) and (b), and $q = \frac{N}{8}$ in (c) and (d).

To process higher-order PPSs with the second-order LPFT, another method for improving the signal representation is to reduce the window length to ensure that each segment can be approximately assumed as a chirp component. Compared with Figure 3.3(a), Figure 3.3(c) shows the improvement on the smoothness of signal representation, which is achieved by reducing the window length q from $\frac{N}{4}$ to $\frac{N}{8}$. It should be noted that, compared with the third-order LPFT with the small window length in Figure 3.3(d), the second-order LPFT

with the same window length in Figure 3.3(c) can achieve comparable result and with less computational complexity. It is worth mentioning that for any order LPFTs, the frequency resolution will become degraded as the window length is reduced, as shown in Figure 3.3(c) and (d). For other higher-order PPSs, the second-order LPFT can also be used, as long as the window length is small enough to ensure that each segment within the window can be approximately assumed as the chirp signal.

It should be noted that in this chapter the Gaussian window function is employed to obtain closed-form expressions for the uncertainty principles of the LPFTs. Other types of window functions, such as the Hamming window function, can also be used in the LPFT to segment the signal. As shown in Figure 3.4, when the Hamming window function is used, similar results can be achieved as in Figure 3.3.

3.4.4 Concentration Comparisons

In this section, we will consider the performances achieved by the STFT, the WVD and the second-order LPFT of a chirp signal obtained from (3.1.2) with $P = 2$. Using the STFT, the corresponding mean frequency and bandwidth are [34]

$$\langle \omega \rangle_t = a_0 + \frac{\alpha a_1 t}{a+\alpha}, \qquad B_t^2 = \frac{a+\alpha}{2} + \frac{a_1^2}{2(a+\alpha)}. \tag{3.4.7}$$

The mean time $\langle \tau \rangle_t$ and the duration T_t^2 of the STFT are same as those of the LPFT. Therefore the uncertainty product of the STFT is

$$B_t^2 T_2^2 = \frac{1}{4} + \frac{a_1^2}{4(a+\alpha)^2}. \tag{3.4.8}$$

When $a_1 = 0$, the frequencies of the input signal do not change with time and the STFT achieves the lowest bound of the uncertainty product $B_t^2 T_t^2 = \frac{1}{4}$. Therefore, the STFT can provide the best resolution only for signals with constant frequencies. For the chirp signals, however, B_t^2 in (3.4.7) has a non-zero second term. Therefore, the uncertainty product $B_t^2 T_t^2$ of the STFT of signals having time varying frequencies must be larger than $\frac{1}{4}$. For the same input signal, if the polynomial parameter ω_1 of the LPFT is correctly estimated, we achieve the lowest bound of the uncertainty product $B_t^2 T_t^2 = \frac{1}{4}$, as seen in (3.3.21). Therefore the second-order LPFT achieves a more concentrated distribution in the time-frequency domain than the STFT.

Another important issue on the LPFT is about the estimation errors on ω_1. Although the PTFT is the maximum likelihood estimator, it is still possible to have some estimation errors, especially when the signals are corrupted by heavy noises. Because the second term of (3.3.11) is proportional to $(a_1 - \omega_1)^2$, the uncertainty product for the second-order LPFT of chirp signals is $B_t^2 T_t^2 > \frac{1}{4}$ if ω_1 is not correctly estimated. Comparison between (3.3.11) and (3.4.7) reveals that as long as $|a_1 - \omega_1| < |a_1|$, i.e., the estimation error of ω_1 is smaller than $|a_1|$, the LPFT of the chirp signal achieves a smaller bandwidth than the STFT. Therefore, the second-order LPFT can still achieve a more concentrated distribution in the time-frequency domain than the STFT. It should be noted that if the estimation error of ω_1 is larger than $|a_1|$, the resolution of the LPFT will become worse than that of the STFT. However such a case rarely happens when the PTFT is used to estimate the polynomial parameters, since the PTFT is the maximum likelihood estimator of the PPS's phase parameters and a satisfactory accuracy for parameter estimation can be easily achieved [90] as discussed in Section 2.3.2.1 of Chapter 2.

In addition to the STFT and LPFT, which are linear time-frequency transforms, another bilinear time-frequency transform, known as the WVD, is often used for many applications [34]. The WVD of the chirp signal is

$$\mathrm{WVD}(t,\omega) = \frac{1}{\pi}\exp\left\{-at^2 - \frac{(\omega - a_1 t - a_0)^2}{a}\right\}.$$

When a is small, the WVD is concentrated on $\omega = a_0 + a_1 t$. The associated mean frequency and bandwidth are [34]

$$\langle\omega\rangle_t = a_0 + a_1 t \qquad \text{and} \qquad B_t^2 = \frac{a}{2}.$$

It means that the WVD can provide a better frequency resolution for chirp signals as far as a is small enough. However, the WVD suffers from the cross terms for multicomponent signals. It is difficult to remove the cross terms without sacrificing the resolution of the signal representation, particularly for non-linear multicomponent chirp signals [34].

Figure 3.5 compares the signal concentration obtained from the FT, the STFT, the LPFT and the WVD. Figure 3.5(a) clearly shows that the FT fails to provide sufficient resolution to represent the chirp signal. For signals with constant frequency components, the STFT can provide the best frequency resolution, as shown in Figure 3.5(b). For chirp signals, with the same window length and window parameter a, however, the LPFT achieves the better frequency resolution than the STFT, as seen from Figure 3.5(c) and (d). Although the WVD has a higher frequency resolution, the cross terms between the two chirp components, as shown in Figure 3.5(e), can be easily mistaken as a valid frequency component. Therefore, the LPFT is the best choice for dealing with multicomponent chirp signals since it is free from the cross terms and also achieves a higher resolution than the STFT.

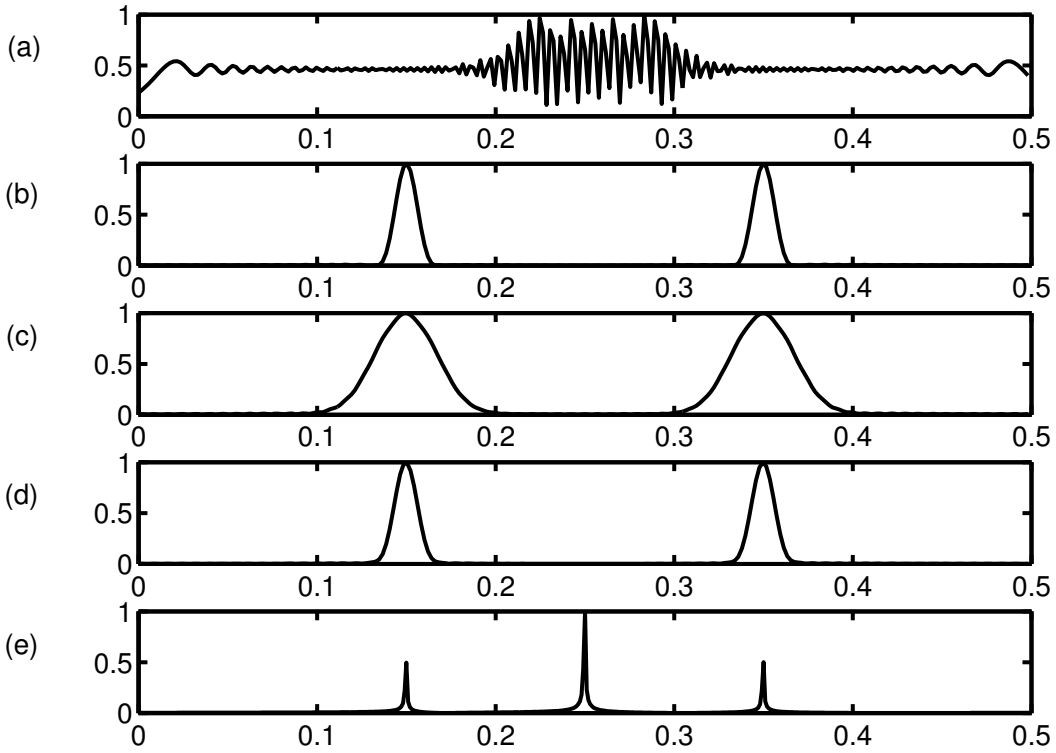

Figure 3.5: Comparison of the time-frequency representations. (a) the FT of the chirp signals, (b) the STFT of a signal with constant frequencies, (c), (d) and (e) the time-frequency representations of chirp signals using the STFT, the second-order LPFT, and the WVD, respectively. The horizontal axis is the normalized frequency and vertical axis is the amplitude.

Furthermore, some real signals are used to compare the resolution performances achieved by the STFT, the WVD and the LPFT. The first example is a speech segment "your mail", and the sampling frequency of the signal is 5512.5Hz. Figure 3.6 shows the speech segment using the STFT, the WVD and the LPFT. The window function is a Hamming window with a length of 512. Figure 3.6 shows that the STFT cannot provide a satisfactory representation of this signal, particularly between the time duration of $0.2 - 0.4$, while the WVD gives undesirable results due to many cross terms between harmonics. The LPFT can provide the best representation for the speech without cross terms. The concentration of the LPFT between $t = 0.2$ and 0.4 is much higher

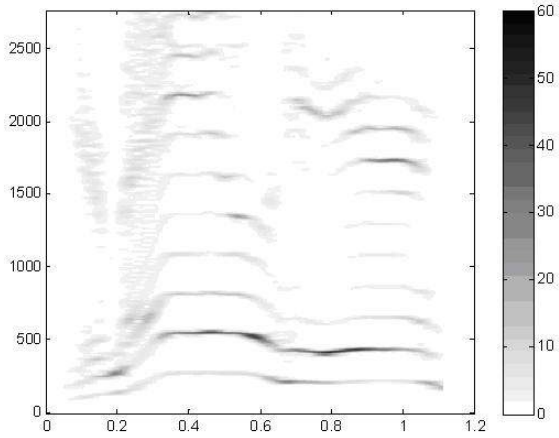

(a) $|\text{STFT}|^2$

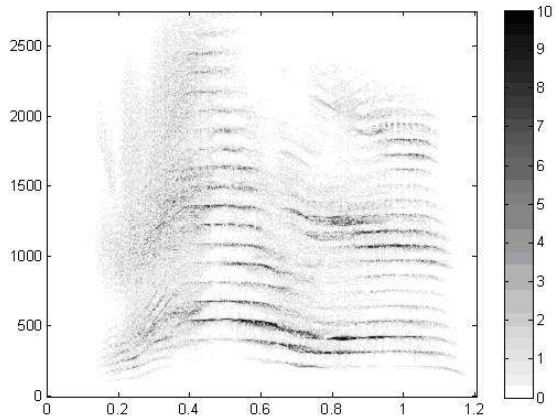

(b) WVD

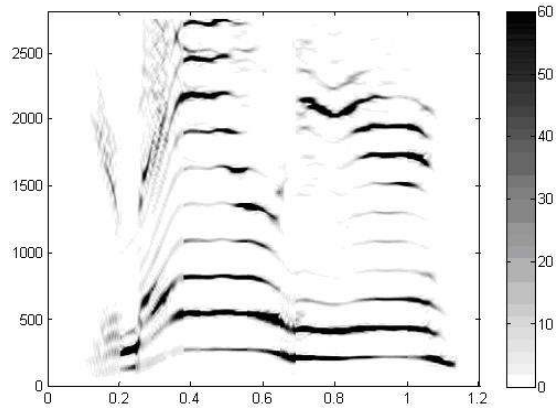

(c) $|\text{LPFT}|^2$

Figure 3.6: The $|\text{STFT}|^2$, WVD and $|\text{LPFT}|^2$ of a speech segment. The horizontal axis is the time instance and vertical axis is the frequency.

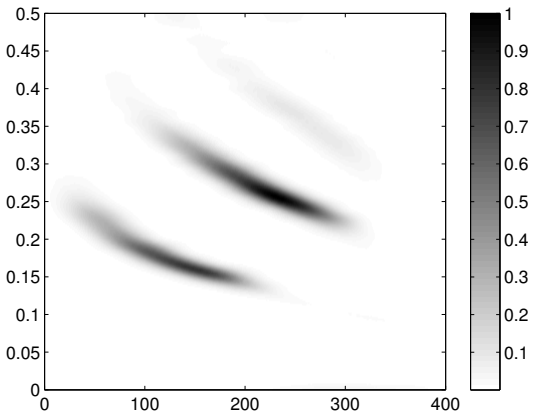

(a) $|\text{STFT}|^2$

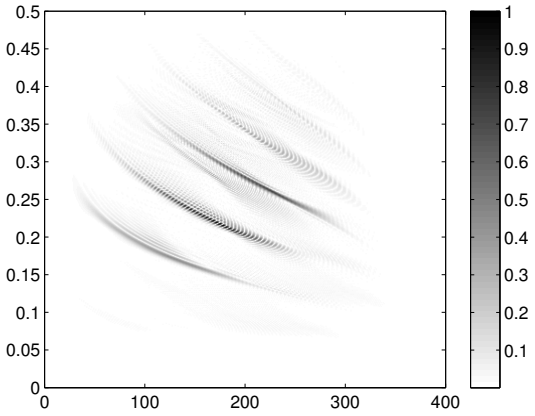

(b) WVD

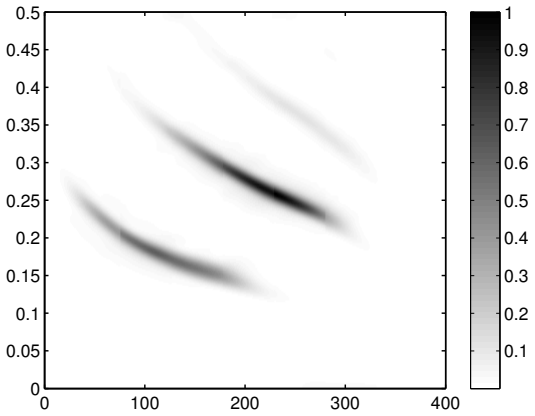

(c) $|\text{LPFT}|^2$

Figure 3.7: The $|\text{STFT}|^2$, WVD and $|\text{LPFT}|^2$ of a bat sound. The horizontal axis is the time instance and vertical axis is the normalized frequency.

than that achieved by the other two transforms, since the extra parameter ω_1 is employed.

The second example we consider is an echolocation pulse emitted by the big brown bat *eptesicus fuscus* [100]. Figure 3.7 illustrates joint time-frequency representations computed by the STFT, the WVD and the LPFT for the bat echolocation. The window function is a Hamming window with $q = \frac{N}{4}$. As shown in Figure 3.7, this sound sample basically consists of three time-varying tones. Compared with other methods, the LPFT not only has better time-frequency resolution but also is free from cross term interference.

3.5 Conclusion

In this chapter, the LPFT is shown to be limited by the uncertainty principle, and the uncertainty principles of various order LPFTs are derived to show the trade-off between the resolutions of signal representation in the time and frequency domains. The uncertainty product of an arbitrary order is determined by the signal parameters, the window function and the errors of estimating the polynomial coefficients. When Gaussian window function is employed to segment the signals, the uncertainty products of the LPFT are time independent under the condition that the polynomial parameters are accurately estimated. The effects of the window width, the estimation errors, and the order mismatch by using the second-order LPFT to process higher-order PPSs are discussed. Concentration comparisons with the STFT and the WVD are also provided to show the merits of the LPFT. Examples in speech and bat sound processing are demonstrated to show that, compared with the STFT and the WVD, the

LPFT is a better tool to deal with signals having time-varying frequencies.

3.6 Appendix: Derivation of the Uncertainty Product for the Mth-order LPFT

In this appendix, the uncertainty product is to be derived for the Mth-order LPFT. It is assumed that the input of the Mth-order LPFT is the PPS of the same order and Gaussian window defined in (3.3.2) is used. For simplicity, only the major steps of derivation are presented.

The phase of the Mth-order PPS defined in (3.1.2) is

$$\Phi = \sum_{m=1}^{M} \frac{a_{m-1}t^m}{m!}.$$

The normalized local signal segment is

$$\begin{aligned}\eta_t(\tau) &= (\frac{\alpha+a}{\pi})^{1/4} \exp\left\{-\frac{a^2t^2}{2(\alpha+a)} + j\omega t - j\sum_{m=2}^{M}\frac{\omega_{m-1}(\tau-t)^m}{m!}\right\} \\ &\quad \cdot \exp\left\{-\frac{(\alpha+a)\tau^2}{2} + a\tau t + j\sum_{m=1}^{M}\frac{a_{m-1}t^m}{m!}\right\}.\end{aligned}$$

With the definition in (3.2.4), we have

$$\begin{aligned}\eta^*(\tau)\frac{d}{d\tau}\eta_t(\tau) &= (\frac{\alpha+a}{\pi}) \exp\left\{-\frac{a^2t^2}{a+\alpha}\right\} \exp\left\{-(a+\alpha)\tau^2 + 2at\tau\right\} \\ &\quad \cdot \left\{-(a+\alpha)\tau + at + j\sum_{m=1}^{M}\frac{a_{m-1}\tau^{m-1}}{(m-1)!} - j\sum_{m=2}^{M}\frac{\omega_{m-1}(\tau-t)^{m-1}}{(m-1)!}\right\}.\end{aligned}$$

When the parameters of the LPFT, such as $\omega_1, \omega_2, ..., \omega_{M-1}$ are estimated correctly, i.e., $\omega_{M-1} = \Phi^{(M)} = a_{M-1}$, ... , $\omega_m = \Phi^{(m+1)}$, ... , $\omega_1 = \Phi^{(2)} =$

$\sum_{m=1}^{M} \frac{a_{m-1}t^{m-2}}{(m-2)!}$, where the superscript of $\Phi^{(m)}$ is the derivative order of Φ, we have

$$\begin{aligned}\eta^*(\tau)\frac{d}{d\tau}\eta_t(\tau) &= (\frac{\alpha+a}{\pi})\exp\left\{-\frac{a^2t^2}{a+\alpha}\right\}\exp\left\{-(a+\alpha)\tau^2+2at\tau\right\} \\ &\quad\cdot\left\{-(a+\alpha)\tau+at+j\sum_{m=1}^{M}\frac{a_{m-1}t^{m-1}}{(m-1)!}\right\}.\end{aligned}$$

Therefore,

$$\begin{aligned}\langle\omega\rangle_t &= \int \eta_t^*(\tau)\frac{1}{j}\frac{d}{d\tau}\eta_t(\tau)d\tau \\ &= \sum_{m=1}^{M}\frac{a_{m-1}t^{m-1}}{(m-1)!} \\ &= \Phi^{(1)},\end{aligned}$$

which is the instantaneous frequency of the Mth-order PPS.

Similarly with $\omega_{M-1} = \Phi^{(M)} = a_{M-1}$, ... , $\omega_m = \Phi^{(m+1)}$, ... , $\omega_1 = \Phi^{(2)} = \sum_{m=1}^{M} \frac{a_{m-1}t^{m-2}}{(m-2)!}$, we have

$$\begin{aligned}\langle\omega^2\rangle &= -\int \eta^*(\tau)\frac{d^2\eta_t(\tau)}{d\tau^2}d\tau \\ &= \int\left\{a+\alpha+\left[(a+\alpha)\tau-at-j\sum_{m=1}^{M}\frac{a_{m-1}t^{m-1}}{(m-1)!}\right]^2\right\} \\ &\quad\cdot\exp\left\{-(a+\alpha)\tau^2+2at\tau\right\}d\tau \\ &= \frac{a+\alpha}{2}+\left[\sum_{m=1}^{M}\frac{a_{m-1}t^{m-1}}{(m-1)!}\right]^2.\end{aligned}$$

Based on the above derivation, we can conclude that if the parameters of the polynomial phase are accurately estimated, the bandwidth obtained by the LPFTs of any order $M > 1$ can be derived to be $(a+\alpha)/2$. With the duration of the PPSs of any order in (3.3.7), the uncertainty product becomes 1/4.

Chapter 4

Quantitative SNR Analysis of the LPFT

4.1 Introduction

In addition to the study of a time-varying signal's frequency content changes, another important role of the time-frequency representations (TFRs) is that they usually increase the signal-to-noise ratio (SNR) in the time-frequency domain [60]. While random noise tends to spread evenly into the entire time-frequency domain, the signal energy is usually concentrated in a relatively small region. Consequently, the regional SNR could be substantially improved in the time-frequency domain. This feature makes the TFRs minimize the effect of noises and better detect and estimate the noisy signals [60]. It also motivates the time-frequency filtering to extract the useful information and reconstruct the signal in the time domain [18].

Quantitatively analyzing the SNR increase for time-frequency representa-

tions is an important issue in practical applications. Generally the SNR is defined as the ratio of the mean power of the signal over the mean power of the noise, where the mean is taken over the whole time domain. Suppose $y(\Omega)$ is a distorted signal

$$y(\Omega) \quad = \quad s(\Omega) + \eta(\Omega), \tag{4.1.1}$$

where the variable Ω is in a domain, such as the time domain, the frequency domain or the time-frequency domain, $s(\Omega)$ is the desired signal and $\eta(\Omega)$ is the additive white Gaussian noise with a mean of zero and a variance of σ^2. The SNR is expressed as

$$\text{SNR} = \frac{\int_0^N s^2(\Omega)}{N\sigma^2}, \tag{4.1.2}$$

where N is the length of the signal $s(\Omega)$. The higher the SNR, the easier the signal detection.

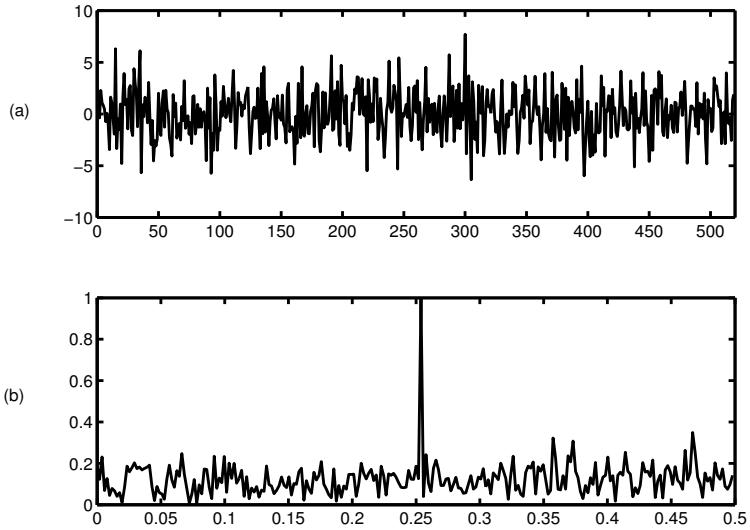

Figure 4.1: A signal with one constant frequency component buried in additive white Gaussian noise with SNR $= -10$dB in (a) time domain and (b) frequency domain.

According to this SNR definition, an orthogonal transform such as the

Fourier transform does not change the SNR [61]. This is because of the energy preservation property of orthogonal transforms. Thus, by taking the Fourier transform the SNR in the frequency domain is equal to the SNR in the time domain. Let us consider a signal with one constant frequency component buried in additive white Gaussian noise with the SNR $= -10$dB. In Figure 4.1 (a), in the time domain it will be impossible to detect the signal from the noise since the SNR is too low. According to the SNR defined in (4.1.2), the SNR of the signal in the frequency domain in Figure 4.1 (b) is still -10dB. However, we can clearly see the signal in the frequency domain. This suggests that the SNR definition in (4.1.2) is not suitable to judge the possibility of detecting the narrowband signals in the frequency domain, as shown in Figure 4.1 (b). It is also shown in [61] that this definition is not proper for time-varying signals in the time-frequency domain. For the time-varying signals, we are not interested in the average signal power but in the peak power of the signal.

Another definition of SNR, introduced in [61], is more suitable for signals in the time-frequency domain as well as in the time and frequency domains, respectively. Compared with the general SNR definition, this definition is transform-domain dependent and directly relates to the bandwidth of the signal [61].

Following the terminology in [61], the 3dB SNR is defined as the ratio of the 3dB mean power of the signal over the mean power of the noise,

$$\mathrm{SNR}^{3dB} = \frac{\int_ß |s(\Omega)|^2 d\Omega}{|ß|\sigma^2}. \tag{4.1.3}$$

Here $|ß|$ is the cardinality of the set ß, with

$$ß = \{t : |s(\Omega)|^2 > 0.5\max|s(\Omega)|^2)\}, \tag{4.1.4}$$

where the number 0.5 is from the 3dB bandwidth definition.

The definition of 3dB SNR is the same as the definition in communications, where only the signal in the 3dB bandwidth is considered. The superscript $3dB$ is used to represent the SNRs defined in (4.1.3) in the rest of the chapter. Following this transform-domain dependent SNR definition in (4.1.3), quantitative analysis on the SNRs achieved by the STFT [61] and the pseudo WVD [62] has been reported in the literature. Because the TFRs concentrate the time-varying signals better than the FT, the SNR increase in the time-frequency domain is higher than the one in the frequency domain due to the increase of the mean signal power. This property quantitatively explains the advantage of the TFRs over the FT for the ISAR imaging [63, 132].

As stated in Chapter 2, compared with the STFT, the local polynomial Fourier transform (LPFT) can further enhance the concentration of chirp signals while spreading the noise. In many different applications [10, 38, 49–53], compared with the FT and the STFT, the LPFT has shown its capability for improving the SNR. For example, in radar imaging, the LPFT can achieve more focused and clearer image than that using the STFT in cases of fast maneuvering targets [50, 51]. For nonstationary interference suppression in noise radar systems, the LPFT is able to achieve performance improvement in comparison with that obtained from the systems based on the STFT [117]. However, how much SNR improvement can be obtained with the LPFT has not been reported. The SNR analysis of the LPFT will help us quantitatively evaluate the SNR improvement of the LPFT.

The focus of this chapter is to present the quantitative analysis of SNRs achieved by using the LPFT based on the relationship between the LPFT and the WVD. Following the 3dB SNR definition in [61, 132], the SNR analysis of

the LPFT is to be investigated and compared with those of the FT, the STFT, and the WVD. Both theoretical analysis and simulation results will show that the use of the LPFT achieves a higher SNR than the FT, the STFT and the WVD.

This chapter is organized as follows. In Section 4.2, the quantitative 3dB SNR analysis of the Fourier transform (FT) and STFT is reviewed. Quantitative 3dB SNR analysis of the pseudo WVD (PWVD) in continuous-time form is presented in Section 4.3. In Section 4.4, quantitative 3dB SNR analysis of the LPFT is derived based on the relationship between the LPFT and the WVD. Section 4.5 presents comparisons on SNRs achieved by using the LPFT, the FT, the STFT and the WVD. Simulation results are presented in Section 4.6 to verify our theoretical analysis and comparisons. Finally, conclusion is given in Section 4.7.

4.2 Review on 3dB SNR Analysis of the FT and STFT

The 3dB SNR analysis of the FT and STFT has been presented in [61, 132] and will be briefly reviewed in this section. The analysis is based on the linear frequency modulated (LFM) signal. As an example, an LFM signal model with monocomponent is considered as:

$$y(t) = s(t) + \eta(t) = A \exp\left[j(a_1 t + \frac{b_1}{2} t^2)\right] + \eta(t) \tag{4.2.1}$$

where a_1 is the initial frequency, b_1 is the chirp rate of the signal, A is the signal amplitude, and $\eta(t)$ is the additive white Gaussian noise with the correlation

function defined as

$$R_\eta(t,\tau) = E[\eta(t)\eta^*(\tau)] = \sigma^2\delta(t-\tau). \tag{4.2.2}$$

Similarly, the signal model containing multiple chirp components with the same mean power is defined by

$$\begin{aligned} \tilde{y}(t) &= \sum_{i=1}^{K} s_i(t) + \eta(t) \\ &= \sum_{i=1}^{K} A\exp[j(a_i t + \frac{b_i}{2}t^2)] + \eta(t), \end{aligned} \tag{4.2.3}$$

where $K > 1$, $s_i(t)$ is the ith chirp component, a_i is the initial frequency, b_i is the chirp rate of different signal components and A is the signal amplitude.

4.2.1 3dB SNR Analysis of the FT

For the signal model containing multiple chirp components with the same mean energy defined in (4.2.3), suppose $S_i(f)$ is the Fourier transform of the LFM signal $s_i(t)$. The 3dB mean power of $S_i(f)$ is less than or equal to [61]

$$\frac{\text{Energy of } S_i(f)}{B_i}, \tag{4.2.4}$$

where B_i is the bandwidth of the $s_i(t)$, that is, $B_i = |b_i|\,T$ where T is the time interval length.

Since the Fourier transform is an orthogonal transform which preserves the signal energy, the energy of $S_i(f)$ is same as that of the $s_i(t)$, that is Energy of $S_i(f)$ = Energy of $s_i(t)$ = TA^2. Therefore, the 3dB SNR in the Fourier transform of $s_i(t)$ is

$$\text{SNR}_{FT} \leq \frac{TA^2}{B_i\sigma^2} \tag{4.2.5}$$

Since the bandwidth $B_i = |b_i|\,T$, the 3dB SNR in the frequency domain for the LFM signal $s_i(t)$ is

$$\mathrm{SNR}_{FT} \leq \frac{1}{|b_i|}\,\mathrm{SNR}_t, \tag{4.2.6}$$

where $\mathrm{SNR}_t = A^2/\sigma^2$ is the SNR of the signal defined in (4.2.1). Following the definition in [61], the overall 3dB SNR of the multicomponent signal can be defined using the overall average 3dB mean power of the signals and the overall noise. Therefore we can easily achieve that

$$\frac{\mathrm{SNR}_t}{\max_{1\leq i\leq K}|b_i|} \leq \max(\mathrm{SNR}_{FT}) \leq \frac{\mathrm{SNR}_t}{\min_{1\leq i\leq K}|b_i|}. \tag{4.2.7}$$

For the signal model containing mono chirp component, the 3dB SNR in the Fourier domain is [61]

$$\mathrm{SNR}_{FT} \leq \frac{1}{|b_1|}\,\mathrm{SNR}_t\,. \tag{4.2.8}$$

4.2.2 3dB SNR Analysis of the STFT

The square of $|\mathrm{STFT}(s;t,\omega)|$, that is the spectrogram, is related to the WVD by [60]:

$$|\mathrm{STFT}(s;t,\omega)|^2 = \int\int \mathrm{WVD}(s;x,y)\mathrm{WVD}(h;t-x,\omega-y)dxdy \tag{4.2.9}$$

where $\mathrm{WVD}(s;t,\omega)$ and $\mathrm{WVD}(h;t,\omega)$ denote the WVDs of the analyzed signal $s(t)$ and the window function $h(t)$, respectively.

Consider the STFT with a Gaussian window function

$$h(t) = (\frac{\alpha}{\pi})^{1/4}\exp(-\frac{\alpha}{2}t^2), \qquad \alpha > 0 \tag{4.2.10}$$

where α is a parameter controlling the width of the window.

For the LFM signal $s(t) = A\exp\left[j(a_1 t + \frac{b_1}{2}t^2)\right]$, the STFT can be achieved as [61, 132]

$$|\mathrm{STFT}(s;t,\omega)|^2 = \frac{2A^2\sqrt{\pi}}{\sqrt{\alpha + \frac{1}{\alpha}b_1^2}} \exp\left\{\frac{-(\omega - b_1 t - a_1)^2}{\alpha + \frac{1}{\alpha}b_1^2}\right\}. \tag{4.2.11}$$

When $\omega = b_1 t + a_1$, the maximum is achieved as

$$\max_{(t,\omega)} |\mathrm{STFT}(s;t,\omega)|^2 = \frac{2A^2\sqrt{\pi}}{\sqrt{\alpha + \frac{1}{\alpha}b_1^2}}. \tag{4.2.12}$$

The 3dB mean signal power is defined as

$$\mathrm{mean}_{(t,\omega)\in S} |\mathrm{STFT}(s;t,\omega)|^2 \tag{4.2.13}$$

where

$$S = \left\{(t,\omega) : |\mathrm{STFT}(s;t,\omega)|^2 > \frac{0.5 \times 2A^2\sqrt{\pi}}{\sqrt{\alpha + \frac{1}{\alpha}b_1^2}}\right\}. \tag{4.2.14}$$

Using (4.2.11) and (4.2.14), we have

$$S = \left\{|\omega - b_1 t - a_1|^2 < (\alpha + \frac{1}{\alpha}b_1^2)\ln 2\right\}. \tag{4.2.15}$$

Then, (4.2.13) becomes

$$\begin{aligned} &\mathrm{mean}_{(t,\omega)\in S} |\mathrm{STFT}(s;t,\omega)|^2 \\ &= \frac{2A^2\sqrt{\pi}}{\sqrt{(\alpha + \frac{1}{\alpha}b_1^2)}} \frac{1}{\sqrt{\ln 2}} \int_0^{\sqrt{\ln 2}} \exp(-u^2)du. \end{aligned} \tag{4.2.16}$$

Since the noise $\eta(t)$ is stationary, its mean power can be calculated in the sample space.

$$\begin{aligned} E|\mathrm{STFT}(\eta;t,\omega)|^2 &= E|\int \eta(t+s)h(s)\exp(-j\omega s)ds|^2 \\ &= \sigma^2. \end{aligned}$$

Therefore the 3dB SNR in the STFT domain is [132]

$$\begin{aligned} \mathrm{SNR}_{STFT}^{3dB} &= \frac{2\gamma\sqrt{\pi}A^2}{\sqrt{\alpha+\frac{1}{\alpha}b_1^2\sigma^2}} \\ &= \frac{2\gamma\sqrt{\pi}}{\sqrt{\alpha+\frac{1}{\alpha}b_1^2}}\mathrm{SNR}_t \end{aligned} \tag{4.2.17}$$

where

$$\gamma = \frac{1}{\sqrt{\ln 2}}\int_0^{\sqrt{\ln 2}} \exp(-u^2)du \approx 0.8.$$

The maximum of the $\mathrm{SNR}_{STFT}^{3dB}$, in terms of the parameter α in (4.2.10), is achieved when

$$\alpha = |b_1| \tag{4.2.18}$$

and the maximum is

$$\begin{aligned} \max_{\alpha}(\mathrm{SNR}_{STFT}^{3dB}) &= \frac{2\gamma\sqrt{\pi}}{\sqrt{2\,|b_1|}}\mathrm{SNR}_t \\ &= \frac{0.8\sqrt{2\pi}}{\sqrt{|b_1|}}\mathrm{SNR}_t. \end{aligned} \tag{4.2.19}$$

Thus,

$$\begin{aligned} &\max_{\alpha}(\mathrm{SNR}_{STFT}^{3dB}) > \mathrm{SNR}_t \\ &\text{when} \qquad |b_1| < 1.28\pi, \end{aligned} \tag{4.2.20}$$

which shows the condition that the 3dB SNR in the STFT domain is improved compared with the SNR_t. When the absolute value of the coefficient b_1 is not too large, the SNR in the STFT domain is greater than that in the time domain.

Because the STFT is linear, the above conclusions can be generalized for the signal model containing multiple chirp components with the same mean power defined in (4.2.3). The maximum of the $\mathrm{SNR}_{STFT}^{3dB}$ is bounded as [132]

$$\frac{0.8\sqrt{2\pi}\mathrm{SNR}_t}{\sqrt{\max_{1\le i\le K}|b_i|}} \le \max_{\alpha}(\mathrm{SNR}_{STFT}^{3dB}) \le \frac{0.8\sqrt{2\pi}\mathrm{SNR}_t}{\sqrt{\min_{1\le i\le K}|b_i|}}, \tag{4.2.21}$$

i.e., it is between the maximum and minimum of the components in (4.2.19).

The SNR analysis for the STFT using rectangular or Gaussian window function for discrete time signals was obtained in [61] in terms of the sampling rate. For a multicomponent signal with K monocomponents, the SNR in the discrete STFT domain is

$$\mathrm{SNR}_{tf}^{discrete} \approx D\frac{T_0}{K}\frac{N}{T_0}\mathrm{SNR}_t = D\frac{N}{K}\mathrm{SNR}_t, \tag{4.2.22}$$

where D is a constant, T_0 is the window length, and N/T_0 is the sampling rate. It can be observed that the SNR improvement in the STFT domain over the SNR in the time domain is in the order of N/K, and the sampling rate plays an important role in the SNR analysis.

4.3 Quantitative 3dB SNR Analysis of the PWVD

For the WVD expressed as

$$\mathrm{WVD}(s;t,\omega) = \int s(t+\tau/2)s^*(t-\tau/2)e^{-j\omega\tau}d\tau, \tag{4.3.1}$$

the lag variable τ may practically need to be truncated by a short window. Therefore the windowed version of the WVD, which is called the pseudo WVD (PWVD), defined as

$$\mathrm{PWVD}(s;t,\omega) = \int h(\tau)s(t+\tau/2)s^*(t-\tau/2)e^{-j\omega\tau}d\tau, \tag{4.3.2}$$

is often employed.

The 3dB SNR analysis for the PWVD has been presented in [62] in discrete-time form, which is expressed by

$$\mathrm{SNR}_{tf}^{discrete} \approx D\frac{N}{K^2}\mathrm{SNR}_t\,. \tag{4.3.3}$$

By comparing (4.3.3) with (4.2.22), we can observe that the SNR increase for the PWVD is in the order of N/K^2 while that for the STFT is in the order of N/K. This is because the PWVD is a bilinear transform, whereas the STFT is a linear one. K^2 in (4.3.3) is due to the cross terms for multicomponents in the PWVD [62].

In order to better compare the SNR of the LPFT with that of the PWVD, this section presents the quantitative analysis of the PWVD in continuous-time form.

Based on the definition of the PWVD in (4.3.2), we have

$$\begin{aligned} \mathrm{PWVD}(y;t,\omega) &= \int h(\tau)s(t+\tau/2)s^*(t-\tau/2)e^{-j\omega\tau}d\tau \\ &\quad + \int h(\tau)N(t;\tau)e^{-j\omega\tau}d\tau. \end{aligned} \tag{4.3.4}$$

where

$$N(t;\tau) = \eta(t+\frac{\tau}{2})\eta^*(t-\frac{\tau}{2}) + s(t+\frac{\tau}{2})\eta^*(t-\frac{\tau}{2}) + \eta(t+\frac{\tau}{2})s^*(t-\frac{\tau}{2}).$$

On the right hand side of (4.3.4), the first term is the PWVD of the signal and the second term is the PWVD of the noise and cross terms.

Using the Gaussian window function defined in (4.2.10) which is $h(t) = (\frac{\alpha}{\pi})^{1/4}\exp(-\frac{\alpha}{2}t^2)$, the PWVD of $s(t) = A\exp\left[j(a_1t + \frac{b_1}{2}t^2)\right]$ is

$$\begin{aligned} \mathrm{PWVD}(s;t,\omega) &= A^2(\frac{\alpha}{\pi})^{1/4}\int e^{-\frac{\alpha}{2}\tau^2 - j(\omega-a_1-b_1t)\tau}d\tau \\ &= A^2(\frac{\alpha}{\pi})^{1/4}\sqrt{\frac{2\pi}{\alpha}}e^{-\frac{(\omega-a_1-b_1t)^2}{2\alpha}}. \end{aligned} \tag{4.3.5}$$

The maximum of the $\mathrm{PWVD}(s;t,\omega)$, achieved with $\omega = a_1 + b_1t$, is

$$\max_{(t,\omega)}\mathrm{PWVD}(s;t,\omega) = A^2(\frac{\alpha}{\pi})^{1/4}\sqrt{\frac{2\pi}{\alpha}}. \tag{4.3.6}$$

The energy of the PWVD$(s;t,\omega)$ within the 3dB bandwidth is defined as

$$\text{mean}_{(t,\omega)\in ß}\,\text{PWVD}(s;t,\omega) \tag{4.3.7}$$

where

$$ß \;=\; \{(t,\omega):\text{PWVD}(s;t,\omega)>0.5\max_{(t,\omega)}\text{PWVD}(s;t,\omega)\}. \tag{4.3.8}$$

Using (4.3.5) and (4.3.6), we have

$$ß=\{(t,\omega):|\omega-a_1-b_1t|^2<2\alpha\ln 2\}. \tag{4.3.9}$$

Thus the 3dB mean of the PWVD in (4.3.7) becomes

$$\begin{aligned}\text{mean}_{(t,\omega)\in ß}\,\text{PWVD}(s;t,\omega) &= A^2(\frac{\alpha}{\pi})^{1/4}\sqrt{\frac{2\pi}{\alpha}}\frac{1}{\sqrt{\ln 2}}\int_0^{\sqrt{\ln 2}}e^{-u^2}du\\ &= 0.8\sqrt{2}A^2(\frac{\pi}{\alpha})^{1/4}.\end{aligned} \tag{4.3.10}$$

Since the noise $\eta(t)$ is stationary and independent of $s(t)$, the mean power of the noise terms in the PWVD domain is

$$E\left[\int h(\tau)N(t;\tau)e^{-j\omega\tau}d\tau\right]=E[\text{PWVD}(\eta;t,\omega)]=\sigma^2. \tag{4.3.11}$$

Thus from (4.3.10) and (4.3.11) we have

$$\text{SNR}_{PWVD}^{3dB}=0.8\sqrt{2}(\frac{\pi}{\alpha})^{1/4}\text{SNR}_t,$$

which means that the SNR of the PWVD is controlled by the window parameter α. When the α is not too big, the SNR in the PWVD domain is greater than that in the time domain.

4.4 Quantitative 3dB SNR Analysis of the LPFT

In this section, the relationship between the LPFT and the WVD will be derived. Based on this relationship, the 3dB SNR analysis of the LPFT will presented.

4.4.1 Relationship between the LPFT and WVD

It has been reported in [60] that the square of $|\mathrm{STFT}(s;t,\omega)|$ is related to the WVD by:

$$|\mathrm{STFT}(s;t,\omega)|^2 = \int\int \mathrm{WVD}(s;\tau,\theta)\mathrm{WVD}(h;t-\tau,\omega-\theta)d\tau d\theta \qquad (4.4.1)$$

where $\mathrm{WVD}(s;t,\omega)$ and $\mathrm{WVD}(h;t,\omega)$ denote the WVDs of the analyzed signal $s(t)$ and the window function $h(t)$, respectively.

Similarly the square of $|\mathrm{LPFT}(s;t,\omega)|$, that is also known as local polynomial periodogram (LPP) [38], can be written as:

$$|\mathrm{LPFT}(s;t,\omega)|^2 = \int\int \mathrm{WVD}(s;t-\tau,\omega-\omega_1\tau-\theta)\mathrm{WVD}(h;\tau,\theta)d\tau d\theta, \qquad (4.4.2)$$

which is the relationship between the LPFT and the WVD to be used to analyze the SNR achieved by using the LPFT. Here we assume that the window function $h(t)$ is real even window. This equality can be proved by expanding the right hand side of (4.4.2) as follows:

$$\begin{aligned}
&\int\int\int\int s(t-\tau+\frac{\mu}{2})s^*(t-\tau-\frac{\mu}{2}) \\
&\quad\cdot\exp[-j(\omega-\omega_1\tau-\theta)\mu]h(\tau+\frac{\nu}{2})h^*(\tau-\frac{\nu}{2})\exp[-j\theta\nu]d\mu d\nu d\tau d\theta \\
&=\int\int\int s(t-\tau+\frac{\mu}{2})s^*(t-\tau-\frac{\mu}{2}) \\
&\quad\cdot\exp[-j(\omega-\omega_1\tau)\mu]h(\tau+\frac{\nu}{2})h^*(\tau-\frac{\nu}{2})\delta(\nu-\mu)d\mu d\nu d\tau \\
&=\int\int s(t-\tau+\frac{\nu}{2})s^*(t-\tau-\frac{\nu}{2}) \\
&\quad\cdot h(\tau+\frac{\nu}{2})h^*(\tau-\frac{\nu}{2})\exp[-j(\omega-\omega_1\tau)\nu]d\nu d\tau. \qquad (4.4.3)
\end{aligned}$$

Let $a=\tau+\nu/2$ and $b=\tau-\nu/2$, we have $\tau=(a+b)/2$ and $\nu=a-b$.

With $d\nu d\tau = |J| da db$, where the Jacobian determinant is

$$J = \begin{vmatrix} \frac{\partial \tau}{\partial a} & \frac{\partial \tau}{\partial b} \\ \frac{\partial \nu}{\partial a} & \frac{\partial \nu}{\partial b} \end{vmatrix} = -1,$$

(4.4.3) becomes

$$\begin{aligned} &\int s(t-b)h^*(b)\exp(j\omega b)\exp(-j\frac{\omega_1}{2}b^2)db \\ &\quad \cdot \int s^*(t-a)h(a)\exp(-j\omega a)\exp(j\frac{\omega_1}{2}a^2)da \\ &= |\mathrm{LPFT}(s;t,\omega)|^2. \end{aligned}$$

In the next section, we will use the relationship in (4.4.2) between the LPFT and the WVD as the basis to develop the SNR analysis of the LPFT.

As introduced in Chapter 2, another popular time-frequency representation, which is called the ambiguity function (AF), is defined as

$$\mathrm{AF}(x;\theta,\tau) = \int x(t+\frac{\tau}{2})x^*(t-\frac{\tau}{2})e^{j\theta t}dt. \tag{4.4.4}$$

The WVD has a close relationship with the AF, and it can be expressed as a double Fourier transform of the AF. The relationship between the spectrogram and the AF has been reported as follows [133],

$$|\mathrm{STFT}(s;t,\omega)|^2 = \int\int \mathrm{AF}(s;\theta,\tau)\mathrm{AF}(h;\theta,\tau)e^{-j(\theta t+\omega\tau)}d\tau d\theta. \tag{4.4.5}$$

Following the similar procedure as the derivation of the relationship between the LPFT and WVD, we can derive the relationship between the LPFT and the ambiguity function, which is presented below without giving further details.

$$|\mathrm{LPFT}(s;t,\omega)|^2 = \int\int \mathrm{AF}(s;\tau,\theta-\omega_1\tau)\mathrm{AF}(h;\tau,\theta)e^{-j(\theta t+\omega\tau-\omega_1 t\tau)}d\tau d\theta \tag{4.4.6}$$

4.4.2 Derivation of the Quantitative 3dB SNR Analysis for the LPFT

Similar to that in [132], let us consider the LPFT with a Gaussian window function

$$h(t) = (\frac{\alpha}{\pi})^{1/4} \exp(-\frac{\alpha}{2}t^2), \qquad \alpha > 0 \tag{4.4.7}$$

where α is a parameter controlling the width of the window. Since the LPFT is a linear transformation, the LPFTs of the signal $s(t)$ and the noise $\eta(t)$ can be considered separately.

The WVD of the signal $s(t) = A\exp\left[j(a_1 t + \frac{b_1}{2}t^2)\right]$ is

$$\mathrm{WVD}(s;t,\omega) \approx A^2\delta(\omega - b_1 t - a_1). \tag{4.4.8}$$

The WVD of the Gaussian window function was reported to be [60],

$$\mathrm{WVD}(h;t,\omega) = 2\exp[-(\alpha t^2 + \frac{1}{\alpha}\omega^2)]. \tag{4.4.9}$$

Using (4.4.2), the LPP of the signal is

$$\begin{aligned}
&|\mathrm{LPFT}(s;t,\omega)|^2 \\
&= 2A^2 \int\int \delta[\omega - \omega_1 x - y - b_1(t-x) - a_1] \\
&\quad \cdot \exp[-(\alpha x^2 + \frac{1}{\alpha}y^2)]dxdy \\
&= \frac{2A^2\sqrt{\pi}}{\sqrt{\alpha + \frac{1}{\alpha}(\omega_1 - b_1)^2}} \exp\left\{\frac{-(\omega - b_1 t - a_1)^2}{\alpha + \frac{1}{\alpha}(\omega_1 - b_1)^2}\right\}.
\end{aligned} \tag{4.4.10}$$

The maximum of $|\mathrm{LPFT}(s;t,\omega,\omega_1)|^2$, achieved at $\omega = b_1 t + a_1$, is

$$\max_{(t,\omega)} |\mathrm{LPFT}(s;t,\omega)|^2 = \frac{2A^2\sqrt{\pi}}{\sqrt{\alpha + \frac{1}{\alpha}(\omega_1 - b_1)^2}}. \tag{4.4.11}$$

The energy of $|\text{LPFT}(s;t,\omega,\omega_1)|^2$ within the 3dB bandwidth is defined as

$$\text{mean}_{(t,\omega)\in S}\,|\text{LPFT}(s;t,\omega)|^2 \tag{4.4.12}$$

where

$$S=\left\{(t,\omega):|\text{LPFT}(s;t,\omega)|^2>\frac{0.5\times 2A^2\sqrt{\pi}}{\sqrt{\alpha+\frac{1}{\alpha}(\omega_1-b_1)^2}}\right\}. \tag{4.4.13}$$

Using (4.4.10) and (4.4.13), we have

$$S=\left\{|\omega-b_1t-a_1|^2<(\alpha+\frac{1}{\alpha}(\omega_1-b_1)^2)\ln 2\right\}. \tag{4.4.14}$$

Then, (4.4.12) becomes

$$\begin{aligned}&\text{mean}_{(t,\omega)\in S}\,|\text{LPFT}(s;t,\omega)|^2 \qquad (4.4.15)\\ &=\frac{2A^2\sqrt{\pi}}{\sqrt{(\alpha+\frac{1}{\alpha}(\omega_1-b_1)^2)}}\frac{1}{\sqrt{\ln 2}}\int_0^{\sqrt{\ln 2}}\exp(-u^2)du.\end{aligned}$$

Since the noise $\eta(t)$ is stationary, its mean energy can be found in the sample space.

$$\begin{aligned}E|\text{LPFT}(\eta;t,\omega)|^2 &= E|\int\eta(t+s)h(s)\exp(-j\omega s)\exp(-j\frac{\omega_1}{2}s^2)ds|^2\\ &= \sigma^2.\end{aligned}$$

Therefore the 3dB SNR in the LPFT domain is

$$\begin{aligned}\text{SNR}_{LPFT}^{3dB} &= \frac{2\gamma\sqrt{\pi}A^2}{\sqrt{\alpha+\frac{1}{\alpha}(\omega_1-b_1)^2\sigma^2}}\\ &= \frac{2\gamma\sqrt{\pi}}{\sqrt{\alpha+\frac{1}{\alpha}(\omega_1-b_1)^2}}\text{SNR}_t \qquad (4.4.16)\end{aligned}$$

where $\text{SNR}_t=A^2/\sigma^2$ is the SNR of the signal defined in (4.2.1), and

$$\gamma=\frac{1}{\sqrt{\ln 2}}\int_0^{\sqrt{\ln 2}}\exp(-u^2)du\approx 0.8.$$

The maximum of the $\mathrm{SNR}_{LPFT}^{3dB}$, in terms of the parameter α in (4.2.10), is achieved when

$$\alpha = |\omega_1 - b_1| \tag{4.4.17}$$

and the maximum is

$$\begin{aligned} \max_{\alpha}(\mathrm{SNR}_{LPFT}^{3dB}) &= \frac{2\gamma\sqrt{\pi}}{\sqrt{2|\omega_1 - b_1|}}\mathrm{SNR}_t \\ &= \frac{0.8\sqrt{2\pi}}{\sqrt{|\omega_1 - b_1|}}\mathrm{SNR}_t. \end{aligned} \tag{4.4.18}$$

Thus,

$$\begin{aligned} &\max_{\alpha}(\mathrm{SNR}_{LPFT}^{3dB}) > \mathrm{SNR}_t \\ \text{when} \quad &\frac{0.8\sqrt{2\pi}}{\sqrt{|\omega_1 - b_1|}} > 1, \end{aligned} \tag{4.4.19}$$

which shows the condition that the 3dB SNR in the LPFT domain is improved compared with the SNR_t.

The above analysis is for analog LFM signals, but in practical computations, the analog signals need to be sampled. Thus the sampling rate plays an important role in achieving the sufficient resolution. Since the LPFT is a generalized form of the STFT, the LPFT can be obtained by using an STFT procedure, i.e., by sliding the window $h(t)$ over the modulated signal $s(t+\tau)\exp(-j\omega_1\tau^2/2)$, and then implementing the FFT. Therefore, the SNR of the discrete LPFT domain can be expressed as [61],

$$\mathrm{SNR}_{tf}^{discrete} \approx D\frac{T_0}{K}\frac{N}{T_0}\mathrm{SNR}_t = D\frac{N}{K}\mathrm{SNR}_t \tag{4.4.20}$$

where D is a constant, K is the number of monocomponents in the signal, T_0 is the window length, and N/T_0 is the sampling rate. Let us discuss the

relationship among the SNR, the coefficient $|\omega_{1,i} - b_i|$, the sampling rate, and the window length.

For simplicity, let us consider the following sampled signal

$$s_T(\frac{k}{N}) = \exp\{j|\omega_1 - b_1|(T_0 k/N)^2\}, \tag{4.4.21}$$

where $k = 0, 1, ..., N-1$. In (4.4.21), it is equivalent that the coefficient $|\omega_1 - b_1|$ tends to be zero when the sampling rate N/T_0 tends to be infinity.

For the discrete LPFT of discrete-time signals in (4.4.20), the SNR in the LPFT domain tends to be infinity when the sampling rate approaches to infinity. For analog signals, in (4.4.18), the SNR in the LPFT domain becomes infinite when the coefficient $|\omega_1 - b_1|$ approaches to zero. As seen from the consideration on the sampled signal, these two results are equivalent, i.e., (4.4.20) is equivalent to (4.4.18) from the point view of SNR improvement.

Because the LPFT is linear, the above conclusions can be generalized for the signal model containing multiple chirp components with the same mean power defined in (4.2.3). The maximum of the SNR_{LPFT}^{3dB} is bounded as

$$\frac{0.8\sqrt{2\pi}\text{SNR}_t}{\sqrt{\max_{1\le i\le K}|\omega_{1,i} - b_i|}} \le \max_{\alpha}(\text{SNR}_{LPFT}^{3dB}) \le \frac{0.8\sqrt{2\pi}\text{SNR}_t}{\sqrt{\min_{1\le i\le K}|\omega_{1,i} - b_i|}}, \tag{4.4.22}$$

where $\omega_{1,i}$ denotes the chirp rate of LPFT of the ith component.

It is worth noting that when ω_1 is set to zero, the LPFT becomes the STFT, and the quantitative analysis for the LPFT becomes that for the STFT as given in [132].

4.5 Comparisons

In this section, the LPFT is compared with the FT, the STFT and the WVD in SNR analysis to show that the LPFT can achieve improved SNR performance than the FT, the STFT and the WVD.

The details of the 3dB SNR achieved by the LPFT was presented in Section 4.4.2, and the main results are rewritten here for the convenience of the readers to compare the LPFT with other transforms. The 3dB SNR in the LPFT domain is

$$\mathrm{SNR}_{LPFT}^{3dB} = \frac{1.6\sqrt{\pi}}{\sqrt{\alpha + \frac{1}{\alpha}(\omega_1 - b_1)^2}}\mathrm{SNR}_t\,. \tag{4.5.1}$$

The maximum of the $\mathrm{SNR}_{LPFT}^{3dB}$, achieved with $\alpha = |\omega_1 - b_1|$, is

$$\max_{\alpha}(\mathrm{SNR}_{LPFT}^{3dB}) = \frac{0.8\sqrt{2\pi}}{\sqrt{|\omega_1 - b_1|}}\mathrm{SNR}_t. \tag{4.5.2}$$

Because the 3dB SNR in the frequency domain is $\mathrm{SNR}_{FT}^{3dB} \leq \frac{1}{|b_1|}\mathrm{SNR}_t$ [132], we have

$$\begin{aligned} &\max_{\alpha}(\mathrm{SNR}_{LPFT}^{3dB}) > \mathrm{SNR}_{FT}^{3dB} \\ &\text{when} \qquad \frac{0.8\sqrt{2\pi}|b_1|}{\sqrt{|\omega_1 - b_1|}} > 1, \end{aligned} \tag{4.5.3}$$

which shows the condition that the 3dB SNR in the LPFT domain is improved compared with the SNR in the Fourier transform domain.

The maximum 3dB SNR in the STFT domain was [132]

$$\max_{\alpha'}(\mathrm{SNR}_{STFT}^{3dB}) = 0.8\frac{\sqrt{2\pi}}{\sqrt{b_1}}\mathrm{SNR}_t, \tag{4.5.4}$$

where $\alpha' = |b_1|$, which is optimal to achieve the maximum of $\mathrm{SNR}_{STFT}^{3dB}$. From

(4.5.2) and (4.5.4), we have

$$\frac{\max_{\alpha}(\mathrm{SNR}_{LPFT}^{3dB})}{\max_{\alpha'}(\mathrm{SNR}_{STFT}^{3dB})} = |\frac{b_1}{\omega_1 - b_1}| \tag{4.5.5}$$

which indicates that as long as $|\frac{b_1}{\omega_1 - b_1}| > 1$, the maximum of $\mathrm{SNR}_{LPFT}^{3dB}$ is larger than $\mathrm{SNR}_{STFT}^{3dB}$. When $\omega_1 = b_1$, the ratio in (4.5.5) becomes infinity, which means that the method based on the LPFT can achieve a significantly higher SNR than that based on the STFT.

The 3dB SNR achieved by the PWVD has been presented in Section 4.3 as

$$\mathrm{SNR}_{PWVD}^{3dB} = 0.8\sqrt{2}(\frac{\pi}{\alpha})^{1/4}\mathrm{SNR}_t,$$

Thus, we have

$$\frac{\max_{\alpha}(\mathrm{SNR}_{LPFT}^{3dB})}{\mathrm{SNR}_{PWVD}^{3dB}} = \left(\frac{\pi}{|\omega_1 - b_1|}\right)^{1/4} \tag{4.5.6}$$

which means that as long as $|\omega_1 - b_1| \leq \pi$, or $b_1 - \pi \leq \omega_1 \leq b_1 + \pi$, a higher $\mathrm{SNR}_{LPFT}^{3dB}$ than $\mathrm{SNR}_{PWVD}^{3dB}$ is obtained. Furthermore, when ω_1 is estimated correctly, the parameter $\alpha = |\omega_1 - b_1|$ approaches to zero. Under this condition, the maximum $\mathrm{SNR}_{LPFT}^{3dB}$ approaches to infinity.

From (4.5.3), (4.5.5) and (4.5.6), we can see that the estimation of the parameter ω_1 is very important. For example, for the comparison of the SNR of the LPFT and STFT in (4.5.5), as long as $|\omega_1 - b_1| < |b_1|$, that is the estimation error of ω_1 is smaller than $|b_1|$, the LPFT can achieve a better SNR than the STFT. It should be noted that if the estimation error of ω_1 is larger than $|b_1|$, the SNR of the LPFT will become worse than that of the STFT. However such a case rarely happens when the PTFT is used to estimate the polynomial parameters, since the PTFT is a maximum likelihood estimator of the PPS's

phase parameters and a satisfactory accuracy for parameter estimation can be easily achieved [90] as discussed in Section 2.3.2.1 of Chapter 2.

As shown in Section 4.4.2, for the signal model containing multiple chirp components with the same mean power defined in (4.2.3), the maximum of the $\mathrm{SNR}_{LPFT}^{3dB}$ is bounded as

$$\frac{0.8\sqrt{2\pi}\mathrm{SNR}_t}{\sqrt{\max_{1\le i\le K}|\omega_{1,i}-b_i|}} \le \max_{\alpha}(\mathrm{SNR}_{LPFT}^{3dB}) \le \frac{0.8\sqrt{2\pi}\mathrm{SNR}_t}{\sqrt{\min_{1\le i\le K}|\omega_{1,i}-b_i|}}, \quad (4.5.7)$$

clearly we have

$$\max_{\alpha}(\mathrm{SNR}_{LPFT}^{3dB}) > \mathrm{SNR}_t$$

when

$$\max_{1\le i\le K}|\omega_{1,i}-b_i| < 1.28\pi. \quad (4.5.8)$$

As shown in [132] that 3dB SNR in the frequency domain is $\mathrm{SNR}_{FT}^{3dB} \le \frac{1}{|b_i|}\mathrm{SNR}_t$, we have

$$\max_{\alpha}(\mathrm{SNR}_{LPFT}^{3dB}) > \mathrm{SNR}_{FT}^{3dB}$$

when

$$\frac{0.8\sqrt{2\pi}|b_i|}{\sqrt{|\omega_{1,i}-b_i|}} > 1. \quad (4.5.9)$$

It is shown that for the multiple chirp signal model, $\mathrm{SNR}_{STFT}^{3dB}$ is [132]

$$\max_{\alpha_i'}(\mathrm{SNR}_{STFT}^{3dB}) = 0.8\frac{\sqrt{2\pi}}{\sqrt{b_i}}\mathrm{SNR}_t.$$

where $\alpha_i' = |b_i|$.

Thus for multiple chirp signals the condition for

$$\max_{\alpha_i}(\mathrm{SNR}_{LPFT}^{3dB}) > \max_{\alpha_i'}(\mathrm{SNR}_{STFT}^{3dB})$$

is

$$\frac{|b_i|}{\max_{1\leq i\leq K}|\omega_{1,i}-b_i|}>1.$$

It can be concluded that as long as ω_1 is estimated correctly, the use of LPFT indeed achieves a significant performance improvement compared to those achieved by using the FT and the STFT.

For signals having multiple components, the WVD generally has cross terms that often lead to incorrect interpretation of signal content. The LPFT, as a linear transform, is free from the cross terms. Therefore, the LPFT of signals having multiple components can still achieve higher 3dB SNR than the WVD, which will be shown using simulations in Chapter 5.

4.6 Simulations

In this section, simulation results are presented to verify the theoretical analysis presented in the above sections. The simulation uses the signal $s(t)=\exp[j(2t+8t^2)]+\eta(t)$ with a sampling rate 333 Hz and $\text{SNR}_t=-3$dB. Figure 4.2 shows that the maximum 3dB SNR is obtained when $\omega_1=16$, which indicates that the 3dB SNR in the time-frequency domain reaches the maximum value when the chirp rate of LPFT ω_1 matches the signal chirp rate b_1.

Figures 4.3, 4.4 and 4.6 present the ratios between SNR_{LPFT}^{3dB} and SNR_{FT}^{3dB}, between SNR_{LPFT}^{3dB} and SNR_{STFT}^{3dB}, and between SNR_{LPFT}^{3dB} and SNR_{PWVD}^{3dB}, respectively. In all figures, the simulation results (solid curves) closely match the theoretical results (dashed curves). More importantly, these figures illustrate that the maximum gain in SNR is achieved when the chirp rate ω_1 used by the LPFT matches the signal chirp rate b_1, compared with those achieved by using

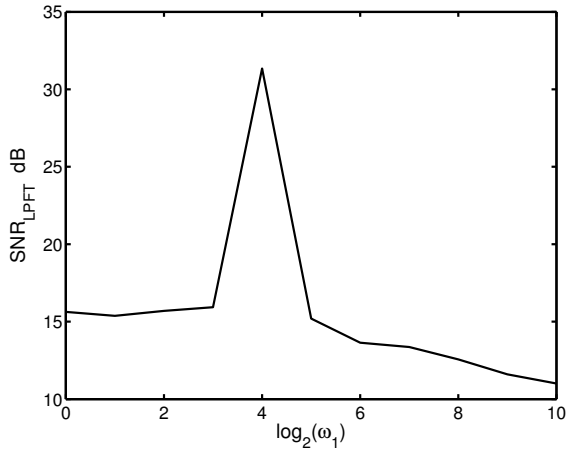

Figure 4.2: The $\mathrm{SNR}_{LPFT}^{3dB}$ versus ω_1.

the FT, the STFT and the PWVD. In order to observe how the estimation of the parameter ω_1 affects the SNR ratios, we take the ratio between the SNR of the LPFT to that of the STFT as an example. As shown in Figure 4.5, we enlarge Figure 4.4 and add the horizontal line to indicate the case when the SNR of the LPFT is equal to that of the STFT. We can see that when ω_1 is smaller than 32, that is the estimation error of the ω_1 is smaller than the signal's chirp rate b_1, the SNR of the LPFT will become bigger than that of the STFT. However, when ω_1 is bigger than 32, that is the estimation error of the ω_1 is bigger than the signal's chirp rate b_1, the SNR of the LPFT will become smaller than that of the STFT. The observation is consistent with our theoretical analysis as shown in (4.5.5).

It should be noted that the SNR analysis for the LPFT is based on the LFM signals. Other kind of time-varying signals such as the sinusoidal FM signals have widely used in applications. For example, when an oscillating object is illuminated with an incident laser, radio frequency, or acoustic wave, sinusoidal FM signals will arise [134]. In helicopter recognition problems, the reflected signal from the helicopter is characterized by sinusoidal FM signals

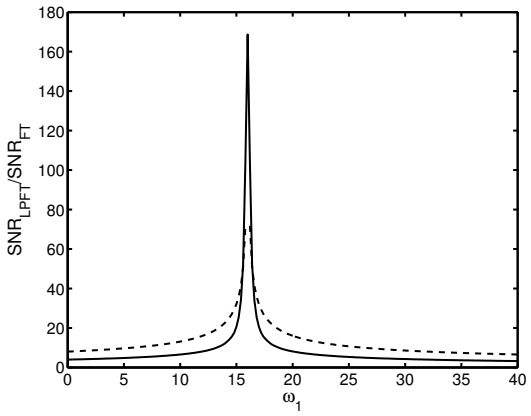

Figure 4.3: The ratio between $\mathrm{SNR}_{LPFT}^{3dB}$ and SNR_{FT}^{3dB}.

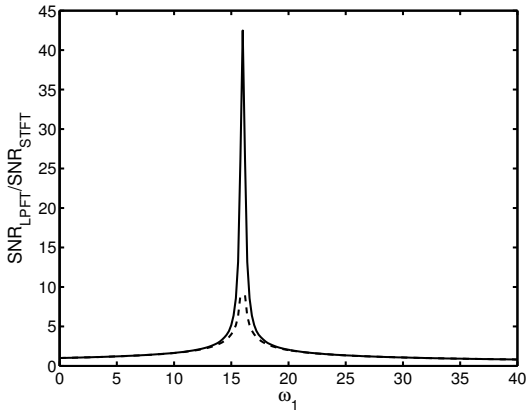

Figure 4.4: The ratio between $\mathrm{SNR}_{LPFT}^{3dB}$ and $\mathrm{SNR}_{STFT}^{3dB}$.

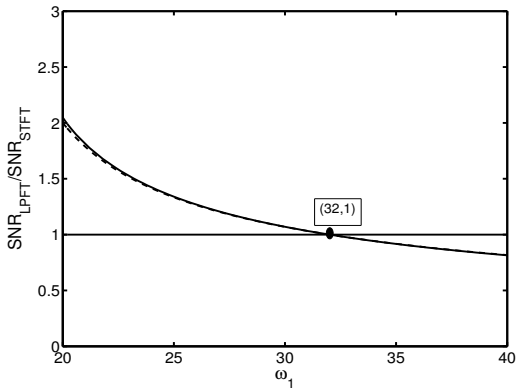

Figure 4.5: Enlarged figure of Figure 4.4 with the ratio between $\mathrm{SNR}_{LPFT}^{3dB}$ and $\mathrm{SNR}_{STFT}^{3dB}$.

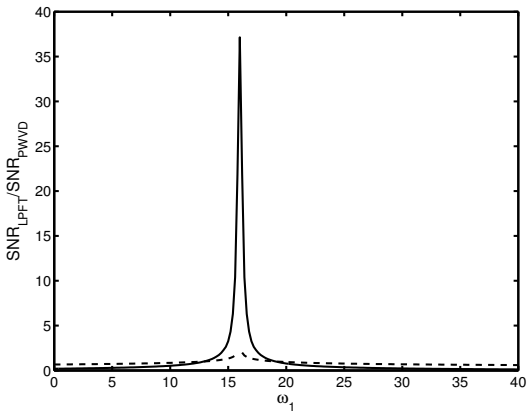

Figure 4.6: The ratio between $\mathrm{SNR}^{3dB}_{LPFT}$ and $\mathrm{SNR}^{3dB}_{PWVD}$.

[135]. Validated by real data collected in pulse-Doppler radars, sinusoidal FM signals also appear as a result of the so-called jet engine modulation phenomenon [136]. For this kind of time-varying signals such as sinusoidal FM signals or parabolic FM signals, we can use the window function to segment the signals so that each segment within the window can be assumed to be the LFM signal. In this way, the LPFT can still achieve high SNR improvement for higher-order time-varying signals. Consider a parabolic FM signal $s(t) = \exp[j2\pi(0.4t - 0.00135t^2 + 0.00000173t^3)]$ with $\mathrm{SNR}_t = -3\mathrm{dB}$. Figure 4.7 presents the signal in different domains. It can be seen that the LPFT can provide improved SNR performance than the methods in other domains such as time domain, frequency domain, STFT domain and WVD domain. Similar conclusion can be drawn for the sinusoidal FM signal as shown in Figure 4.8, as well as for signal with multicomponents as shown in Figure 4.9.

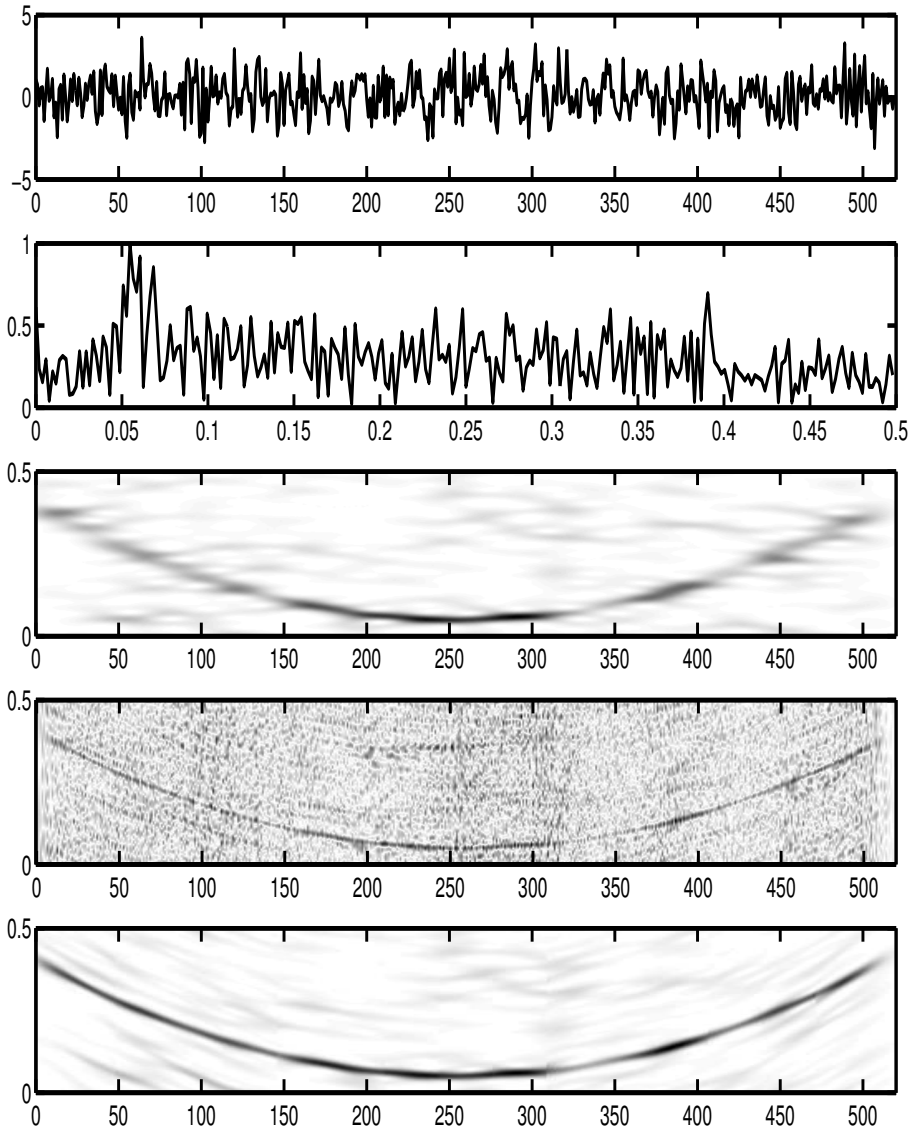

Figure 4.7: The representations of the parabolic FM signal in different domains. From top to bottom: time domain, frequency domain, STFT domain, WVD domain, and LPFT domain. SNR $= -3$dB.

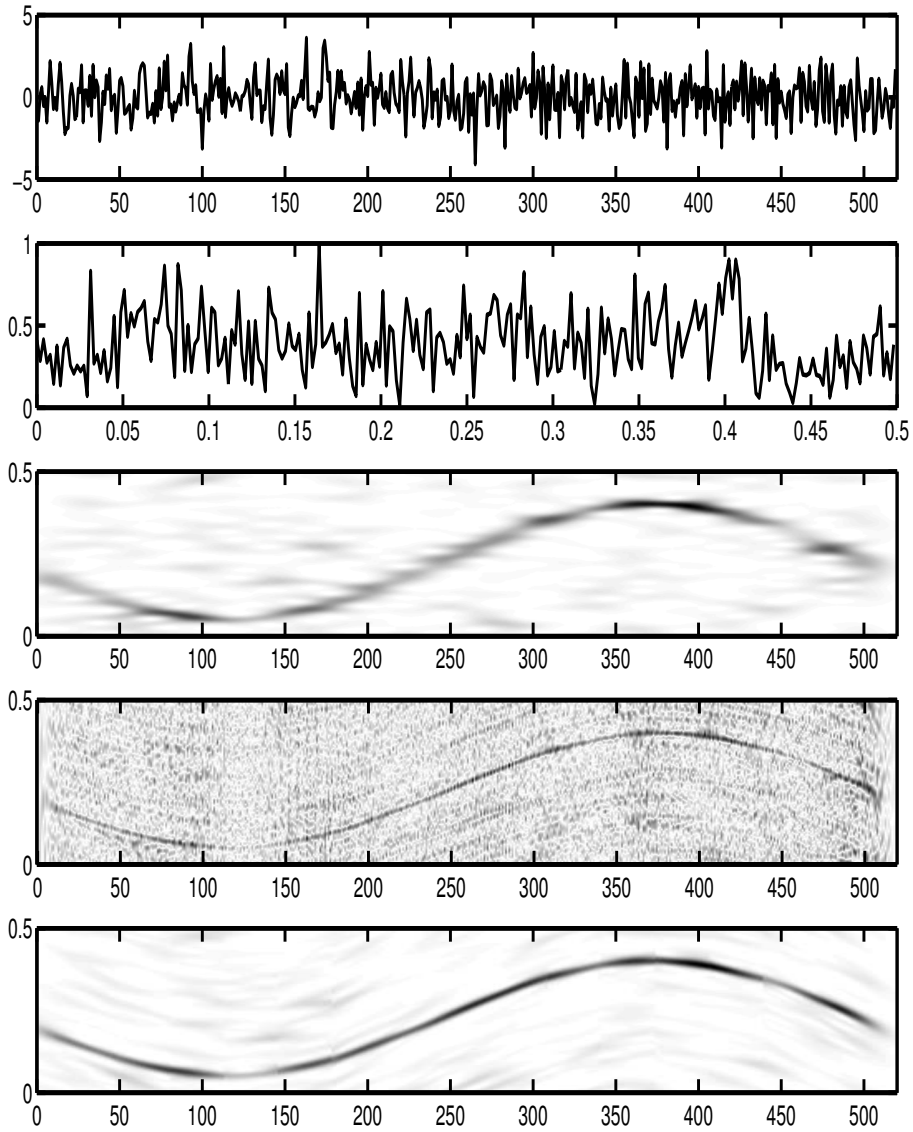

Figure 4.8: The representations of the sinusoidal FM signal in different domains. From top to bottom: time domain, frequency domain, STFT domain, WVD domain, and LPFT domain. SNR $= -3$dB.

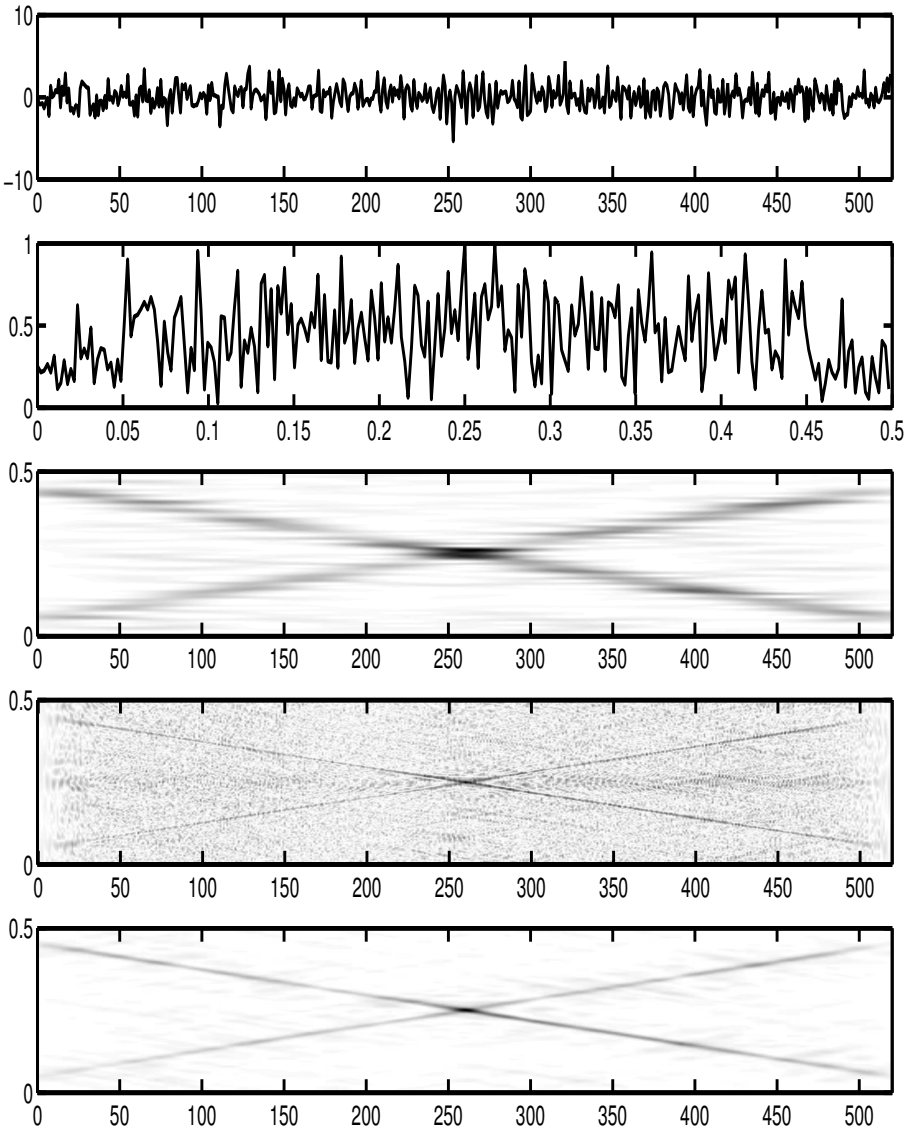

Figure 4.9: The representations of a signal with multiple components in different domains. From top to bottom: time domain, frequency domain, STFT domain, WVD domain, and LPFT domain. SNR = 0dB.

4.7 Conclusion

In this chapter, the 3dB SNR definition, which is transform-domain dependent and directly relates to the bandwidth of the signal, is employed to quantitatively analyze the SNR increase for TFRs. Based on the relationship between the LPFT and WVD, this chapter presents the analysis of 3dB SNR achieved by using the LPFT. The quantitative analysis of the PWVD in continuous-time form is presented as well. Comparisons are made among the SNRs achieved by using the LPFT, the FT, the STFT and the WVD. Both theoretical analysis and simulations show that substantial SNR performance improvements are obtained by using the LPFT.

Chapter 5

Applications of the LPFT in ISAR Imaging and LFM Signal Detection

5.1 Introduction

In Chapter 3 and Chapter 4, theoretical analysis on the LPFT is given on its uncertainty principle and SNR analysis. It has been shown that the LPFT can achieve higher resolution than the STFT and is free from the cross terms that exist in the WVD. Moreover the LPFT can provide higher SNR improvement compared with other transforms such as the STFT and the WVD. The LPFT has been found to be a better tool to deal with signals having time-varying frequencies and has been employed in a variety of practical applications. The following are some examples.

- The LPFT is useful for interference suppression in communication sys-

tems to achieve performance improvement [52, 53], compared with that obtained from the systems based on the STFT.

- A new form of beamformer based on the LPFT is derived in [118] for source localization and tracking in nonstationary environment, which can resolve closely spaced sources provided that their velocities are sufficiently different.

- Motion parameters in video sequences, such as the velocity and acceleration, can be estimated using the LPFT [10].

In this chapter some more applications using the LPFT are presented to show the advantage of the LPFT and verify the theoretical SNR analysis of the LPFT presented in Chapter 4. This chapter will focus on two application examples, i.e., inverse synthetic aperture radar (ISAR) imaging and LFM signal detection. As presented in Chapter 4, the LPFT can provide higher SNR than other transforms such as the FT, STFT and PWVD. It should be noted that the SNR increase in the LPFT domain is due to the mean signal power increase. It is because that the LPFT can concentrate the LFM signals better than the FT, STFT and PWVD. This property indicates that better ISAR imaging quality using the LPFT can be achieved over the one using the FT and STFT. Moreover, it indicates that the LPFT can achieve more concentrated representation for LFM signals in heavy noise. Therefore, in this chapter, we first use the example in ISAR imaging to show that the LPFT can achieve more focused image than the FT and STFT, followed by the application in chirp detection to show that the LPP can be employed for signals in heavy noise for which the PWVD cannot provide clean presentation.

This chapter is organized as follows. In Section 5.2, the application of the LPFT in ISAR imaging is presented and compared with the FT and the STFT. Simulations which use two sets of radar imaging data to produce the ISAR images are presented to illustrate that the resolution of the ISAR images are improved by using the LPFT. Furthermore, the improvement on imaging performance is obtained by the non-overlapping approach to minimize the required computational complexity. In Section 5.3, the squared LPFT is combined with the Hough transform therefore achieving the LPP-Hough transform (LHT) for LFM signal detection. Numerical examples show that, compared with the pseudo Wigner-Hough transform (PWHT), the LHT achieves significantly better performances for signals corrupted by heavy additive white Gaussian noise (AWGN) and impulsive noise. In addition, the computation time needed by the LHT can be further reduced by using the time-frequency filtering. Conclusion is given in Section 5.4. Appendix in Section 5.5 provides details of the theoretical detection probability of Hough detector.

5.2 ISAR Imaging

5.2.1 Introduction

Radar is an instrument used for the detection and location of targets, such as aircraft, ships, ground vehicles, and terrain. It transmits electromagnetic energy to a target and receives the reflected signal from the target. From the received radar signal, target-related information, such as position and velocity, can be accurately measured. Synthetic aperture radar (SAR), as an airborne or space-borne radar, generates a high-resolution map of stationary surface targets and

terrain, while inverse synthetic aperture radar (ISAR) uses a geometrically inverse operation where the radar is stationary and targets are moving to generate image of targets [19].

To construct images of radar targets from recorded complex data, radar image formation is often required [63], which is a mapping of a three-dimensional (3D) target onto a two-dimensional (2D) range and cross-range plane. The conventional radar image formation is based on the Fourier transform (FT). In ISAR, because the movements of radar targets are usually complicated, motion compensations are generally needed to obtain focused images by using the FT. If the motion compensation is not sufficient, the resulting image can still be blurred when the FT is applied. However, the problem of using the FT can be circumvented if it is replaced by a time-frequency transform (TFT). Various TFTs have been used to mitigate image blurring for improvement on the quality of ISAR images. Although the short-time Fourier transform (STFT) [25] is simple and easy to implement, its resolution is inherently limited by the uncertainty principle. High resolution TFTs, such as Wigner-Ville distribution (WVD) [25] and continuous wavelet transform [64], were studied for ISAR image applications. The approaches based on the adaptive chirplet decomposition and spectral subtraction have been proposed in [137] for detecting a manoeuvring air target in strong sea clutter. However the performances achieved by using some of these transforms generally suffer from the cross-term interferences. Adaptive Gaussian representation [26] and smoothed pseudo WVD [111] were reported to obtain better performances with reduced cross-term interferences. However, these methods need complex computation and require much more computation time than the STFT. In principle, any TFT can be employed for radar image formation. However, a desired TFT should satisfy the following requirements:

i) it should have high resolution in the time-frequency domain, ii) it should accurately reflect the instantaneous frequency (IF) of the analyzed signal, and iii) it should have low cross terms. The LPFT, as introduced in Chapter 2, can provide high resolution for time-varying signals with a local polynomial function approximating to the IF characteristic of the analyzed signals. In addition, it is free from the cross terms due to its linearity. Therefore, in this section the LPFT will be employed as the TFT to obtain higher resolution images.

In radar systems, signals having wide bandwidth are generally required to achieve high range resolution. Widely used wideband signals include linear frequency modulated (LFM) signals and stepped frequency signals. The ISAR signal model that employs stepped frequency modulation has been recently developed in [138], and it has been shown that ISAR imaging reconstruction algorithms based on stepped frequency and linear frequency modulation waveforms attain almost the same performance. In this section the LFM signal model is employed for ISAR imaging using the second-order LPFT. The simulation with the radar data shows that the imaging resolution achieved by using the LPFT is substantially better than that obtained by using other transforms.

This section is organized as follows. After briefly reviewing the ISAR imaging model based on time-frequency transform in Section 5.2.2, simulation results are presented in Section 5.2.3 to illustrate the improvements achieved by using the LPFT on ISAR images.

5.2.2 ISAR Imaging Based on TFTs

To generate an image with radar systems, three major components, i.e., transmitter, target, and receiver, are needed [63]. The transmitter emits a sequence

of pulses to the target to be imaged; then the receiver records the reflected pulses from the target and processes the recorded data to reconstruct an image of the target. For example, to generate the image of the target, the radar transmitter emits a sequence of N pulses and the range resolution is determined by the bandwidth of the pulse. For each transmitted pulse, the total number of range cells, M, is determined by the maximum range covered and the range resolution. The total number of pulses, N, for a given imaging integration time determines Doppler or cross-range resolution. The radar data sequence is formed as a complex 2D array $G(r_{m,n}), (m = 0, 1, \cdots, M-1; n = 0, 1, \cdots, N-1)$, where M is the number of range cells and N is the number of pulses. The 2D radar data used in this chapter can be downloaded from [139].

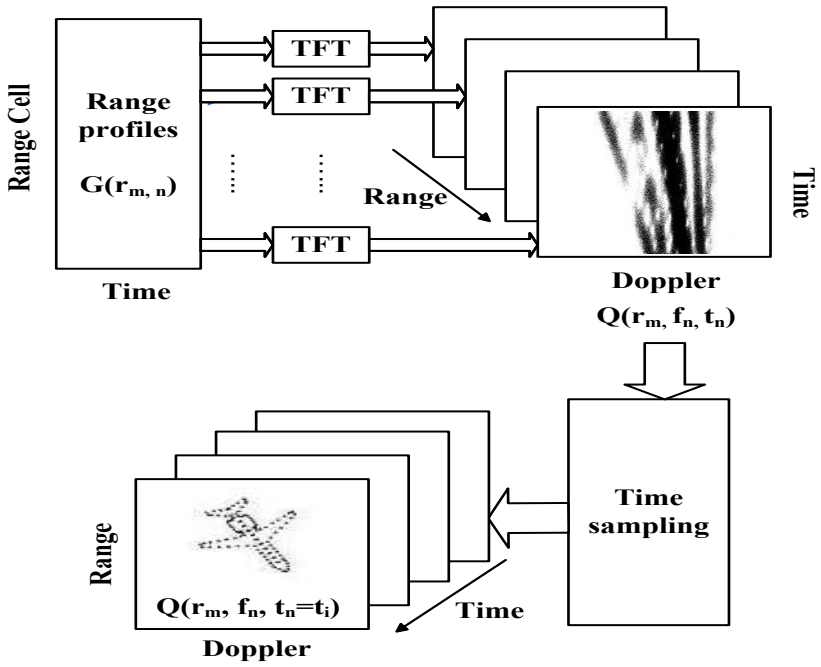

Figure 5.1: Illustration of ISAR imaging using time-frequency transform

Based on the TFTs, Figure 5.1 illustrates the process of radar image formation [63]. Standard motion compensation is needed before the image forma-

tion. An $N \times N$ Doppler-time distribution is generated by performing the TFT at each range cell. Then the $M \times N \times N$ range-Doppler-time cube, $Q(r_m, f_n, t_n) = \mathrm{TFT}_n G(r_{m,n})$, can be formed by combining the Doppler-time distributions at the M range cells. By time sampling from the cube $Q(r_m, f_n, t_n)$, a range-Doppler image frame $Q(r_m, f_n, t_n = t_i)$ can be obtained for a particular time instant t_i. Each of the N image frames represents a full range-Doppler image with a better resolution at a particular time instant [63]. In contrast, the imaging formation based on Fourier transform generates only one blurred 2D $M \times N$ range-Doppler ISAR image frame from the $M \times N$ radar data set. Therefore, by replacing the Fourier transform with the TFT, a 2D range-Doppler image becomes a 3D time-range-Doppler image cube. By taking time sampling, a temporal sequence of 2D range-Doppler images can be achieved. The time-varying properties of the recorded signals can also be observed from these image frames at various time instants.

5.2.3 Simulations

In this section, simulation results are presented to show the advantage of the LPFT and verify the theoretical SNR analysis presented in Chapter 4.

A heavy computational load may be required if a significant overlap between consecutive signal segments is used to deal with long data sequences by using the LPFT, as reported in [50]. However, based on the method in [48], this section shows that even without overlapping between consecutive signal segments, the performance improvement on the resolution of ISAR images can still be achieved by using the LPFT. Thus it is possible to significantly reduce the required computational complexity for the applications of ISAR imaging. It

should be pointed out that for ISAR imaging using the LPFT, in this section ω_1 is estimated from PTFT as reported in [48]. In contrast, the estimation of ω_1 reported in [50] is based on maximizing the concentration measure.

Let us now consider the improvement on ISAR images by using the LPFT. The first simulation uses the simulated aircraft B727 data [63] with $\text{SNR}_t = -5\text{dB}$. The TFT shown in Figure 5.1 is replaced by the LPFT. It is assumed that the center frequency of the radar is 9 GHz and the bandwidth is 150 MHz. The total number of pulses used to form the image is 256.

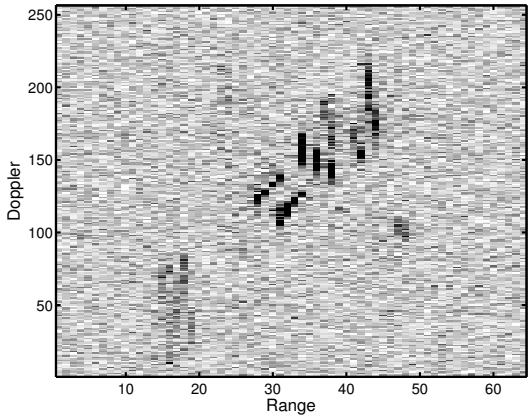

Figure 5.2: ISAR image of B727 formed by using the FT

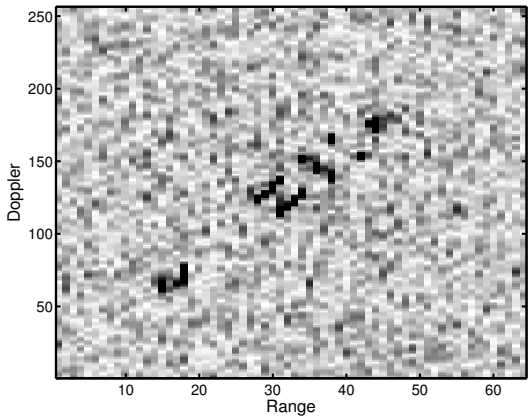

Figure 5.3: ISAR image of B727 formed by using the STFT (64th temporal frame)

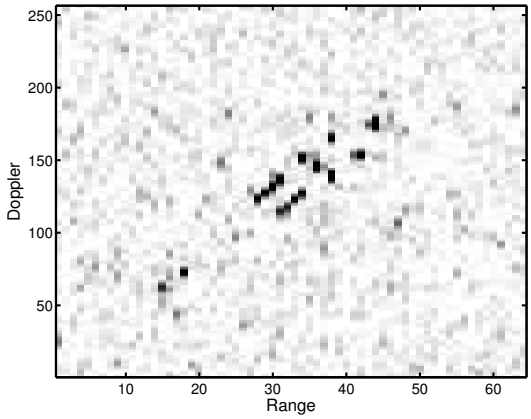

Figure 5.4: ISAR image of B727 formed by using the LPFT (64th temporal frame and $(Q-1)$-point overlapping)

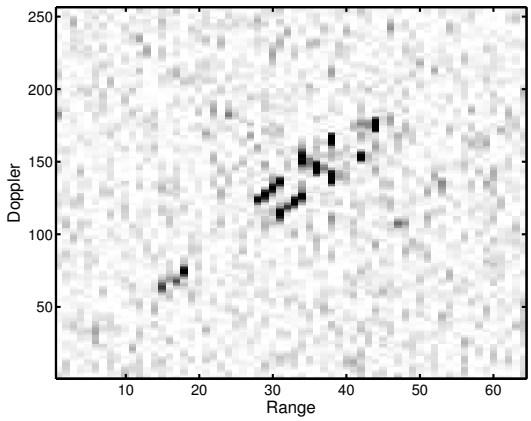

Figure 5.5: ISAR image of B727 formed by using the LPFT (64th temporal frame and no overlapping)

Following the method reported in [48], the initial window length Q is selected to be small enough (for example, $Q = 63$ in this case) to provide an acceptable accuracy of the approximation and the actual length of the window is increased according to the properties of consecutive signal segments. In our experiment, the lengths of overlap between adjacent data segments are set to be the maximum overlapping, i.e., by $(Q-1)$-points, and no overlapping, respectively. Figure 5.2 presents the blurred ISAR image of B727 data constructed by using the FT, and Figure 5.3 is the blurred ISAR image constructed by using the

STFT. Figures 5.4 and 5.5 show the ISAR images formed by using the LPFT with an overlap of $(Q-1)$-points and no overlap, respectively. It is observed that the ISAR achieved by using the LPFT is much better than that achieved by using the STFT and the FT. Furthermore, the difference between Figures 5.4 and 5.5 is hardly visible.

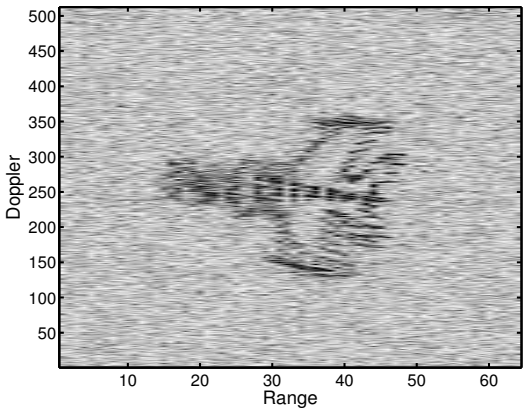

Figure 5.6: ISAR image of MIG-25 formed by using the FT

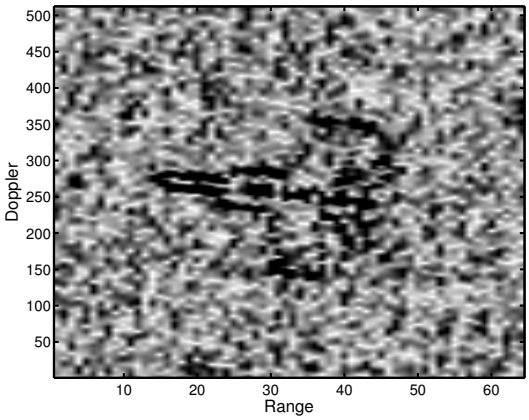

Figure 5.7: ISAR image of MIG-25 formed by using the STFT (64th temporal frame)

The next experiment uses the simulated aircraft MIG-25 ISAR data [63] with $\text{SNR}_t = -5$dB. The simulated aircraft is composed of 120 point scatters of equal reflectivity and the operating frequency is centered at 9 GHz. The 64 stepped

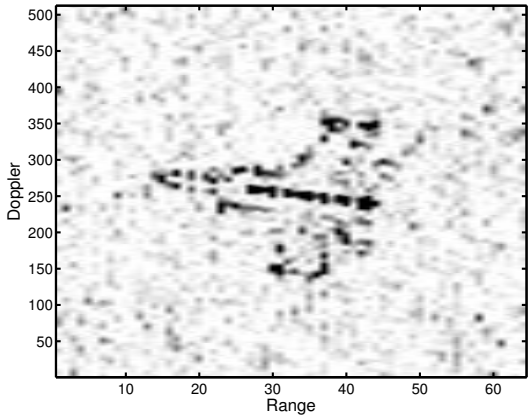

Figure 5.8: ISAR image of MIG-25 formed by using the LPFT (64th temporal frame and $(Q-1)$-point overlapping)

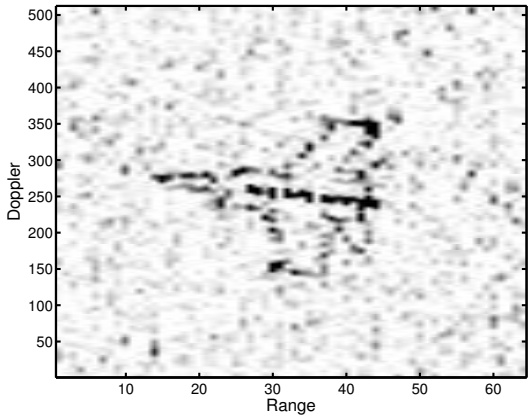

Figure 5.9: ISAR image of MIG-25 formed by using the LPFT (64th temporal frame and no overlapping)

frequencies with 8 MHz intervals and 512 samples of the time history series are used. It is assumed that the aircraft has only a fast rotational motion and the translational motion is perfectly compensated. The overlapping setting is the same as that for the previous experiment. Figure 5.6 is the ISAR image of MIG 25 constructed by using the FT and Figure 5.7 is the ISAR image constructed by using the STFT. Figures 5.8 and 5.9 are the ISAR images obtained by using the LPFT with different lengths of overlapping, respectively. Similar observations can be made as those from Figure 5.2 to Figure 5.5. Such observations are

expected because the LPFT can concentrate the LFM signals better than the FT and the STFT, therefore the use of the LPFT effectively improves the SNRs, as indicated by our analysis in Chapter 4. This property indicates that better ISAR imaging quality using the LPFT can be achieved than the one using the FT and STFT.

Table 5.1: Computational time needed by the STFT and the LPFT for radar imaging

Data	STFT (s)	LPFT without overlap (s)	LPFT with max overlap (s)
B727	13.1389	25.8929	1038.8
Mig25	15.5146	104.2623	5094.4

Table 5.1 compares the computational time needed by the STFT, the LPFT without overlap and the LPFT with the maximum overlap for the radar imaging. The computations are under the Window XP operating system and the programming environment of MATLAB 7.1. The computer is Pentium 4 with a clock rate of 2.66 GHz and a RAM size of 512 MBytes. The simulation results may not be accurate for actual computation time, but they are sufficient for relative comparisons on the computational complexity. The simulation results show that the computation with an overlap of $Q-1$ points needs the most computation time. Because the signal concentration is not sensitive to the length of the overlap, improved concentration can be achieved by using the LPFT with a zero overlap length between the adjacent signal segments. In this way, the performance on signal concentration can be improved without requiring a significant increase in computational complexity compared to that needed by the STFT. More details on the reduction of overlap length can be found in [48].

5.3 LFM Signal Detection

5.3.1 Introduction

Linear frequency modulated (LFM) signals, also known as chirp signals, are often encountered in many applications such as in radar, sonar and communications. Detection and estimation of the LFM signals in a noisy environment are of great importance. Although the generalized likelihood ratio test (GLRT) is assumed to be optimal for chirp detection [140], it requires too much computational complexity to be used for practical applications. Therefore other suboptimal approaches, such as the multiple frequency tracker [141], the recursive least squares (RLS) algorithm [142], the least mean squares (LMS) algorithm [143], neural networks [144] and time-frequency based methods [67–69], are proposed.

The time-frequency-based methods have been reported to be effective for detecting and estimating chirp signals [67–69, 145, 146]. Among all the time-frequency representations, the bilinear Wigner-Ville distribution (WVD) can provide a superior performance on localization of the chirp signal [34]. Therefore an optimal WVD-based detector was designed to detect the LFM signals corrupted by noises [145]. The optimal detector was shown to be equivalent to quadrature matched filtering or the dechirp method [147]. Other time-frequency-based methods for detecting and estimating the LFM signals are also presented. For instance, the Radon-ambiguity transform [68], by applying the Radon transform to the ambiguity function, can detect multiple LFM signals embedded in noise. This approach considers the case that the chirp rate is the only parameter of interest and reduces the detection of LFM signals to the location of maxima over chirp rates only. The pseudo-Wigner-Hough

transform (PWHT) was also proposed in [146] as an estimator for the phase parameters of FM signals, with both good numerical properties and statistical performance. Moreover, the WVD has been combined with the Hough transform, i.e., the Wigner-Hough transform (WHT), to detect the chirp signals [67], with the application to suppressing wideband interferences in spread spectrum communications [12]. Although the WHT can decrease the undesirable cross terms for multicomponent signals, it cannot provide the desirable performance for signals distorted in a heavy noise environment, due to the inherent noise threshold effect problem of the WVD [37]. The Hough transform, combined with the linear STFT, was reported to detect a weak and low rate chirp signal [69]. The detector in the Hough transform domain is close to the optimal detector GLRT for chirp signals corrupted by AWGN and powerful noisy tones [69]. For these methods which combine the time-frequency representation with the Hough transform, a signal representation in the time-frequency domain should be firstly obtained, then it is further processed by the Hough transform, which is a method widely used in image processing for shape detection and feature extraction. Because chirp signals can be described as straight lines in the time-frequency domain, the Hough transform, which integrates along all these lines, is used to convert the task of tracking straight lines in the time-frequency domain into locating the maximum peak in the signal parameter domain. Therefore, for chirp detection, a proper processing method is needed to obtain an appropriate line representation in the time-frequency domain.

Unlike the WVD, due to its linearity the LPFT is free from the cross terms for multicomponent signals. Moreover, for signals with time-varying frequencies the LPFT can provide a higher resolution than the STFT since it employs extra parameters to describe the polynomial phase of the signal. Consider an LFM

signal expressed as

$$s(t) = Ae^{j(a_1 t + \frac{b_1}{2}t^2)}, \tag{5.3.1}$$

using the Gaussian window $h(t) = (\frac{\alpha}{\pi})^{1/4} e^{-\frac{\alpha}{2}t^2}$, the modulus of the LPFT of the LFM signal has been derived in Chapter 4 and is rewritten here as

$$|\mathrm{LPFT}(s;t,\omega)| = \sqrt{2}A \sqrt[4]{\frac{\pi}{\alpha + \frac{1}{\alpha}(b_1 - \omega_1)^2}}\, e^{-\frac{(\omega - a_1 - b_1 t)^2}{2(\alpha + \frac{1}{\alpha}(b_1 - \omega_1))^2}}. \tag{5.3.2}$$

Therefore the LPFT is concentrated along the instantaneous frequency of the LFM signal $\omega = a_1 + b_1 t$, for $\omega_1 = b_1$. The parameter ω_1, which is proportional to the chirp rate of the signal, can be estimated from the location coordinates of the maximum in the polynomial time frequency transform (PTFT) [39, 40]. Since the PTFT is the maximum likelihood estimator and asymptotically achieves the CRLB [78], it can be used to estimate, with a satisfactory accuracy, the parameters of the signal phase which is modelled as a polynomial function. In this section, we will focus on the detection of the LFM signals. Details on parameter estimation of chirp signals can be referred to [39, 40].

It has been shown in Chapter 4 that the LPFT can achieve higher SNR improvement than the PWVD. Therefore the Hough transform becomes more effective on detecting the chirp signals with very low SNRs when the LPFT is used for the image formation. By combining the LPP with the Hough transform, we achieve the new chirp detection method LPP-Hough transform (LHT). The LHT can be indicated as a mapping of the signal from the time-frequency domain onto the signal parameter domain. Based on the combination of the LPP with the Hough transform, this section reports a detailed evaluation of this detection method. It shows that the LHT achieves significant improvements on detecting the chirp signals in very low SNR environments. Moreover the time-frequency filtering can be used to reduce the computation complexity.

This section is organized as follows. Section 5.3.2 provides a review of the Hough transform and the time-frequency filtering. In Section 5.3.3, simulation results for signals in AWGN and impulsive noises are given to show the advantages of the LHT.

5.3.2 Reviews on Hough Transform and Time-Frequency Filtering

5.3.2.1 Hough Transform

The Hough transform is a feature extraction technique to detect lines in an image, which has been widely used in image analysis, computer vision and digital image processing [148]. It converts a difficult global detection problem in image space into a more easily solved local peak detection problem in a parameter space. The Hough transform has many desirable features [149]. First, each point in the image can be treated independently and therefore the Hough transform can be implemented using more than one processing unit; that is, parallel processing of all points is possible. Therefore the Hough transform is an algorithm suitable for real-time applications. Second, the Hough transform can recognize partial or slightly deformed shapes. Occlusion is a severe problem for most other shape detection methods but the Hough transform degrades gracefully because the size of a parameter peak is directly proportional to the number of matching points. Third, the Hough transform is very robust to the extraneous noise due to the line integration operation. The Hough transform was also generalized to detect arbitrary shapes, such as circles, ellipse and parabolas [150]. The Hough transform has been used in a variety of applications, as reported in the

literature [69, 151–154]. For example, the Hough transform has been used to extract detections and simultaneous tracks from multi-dimensional radar data maps [151]. Compared with other traditional techniques, this technique offers many advantages including improved detection, flexibility of implementation, a solution to the range walk problem and automatic track acquisition without revisit. For moving target with rotating parts the Hough transform has been employed as an imaging method to detect the straight lines and the sinusoids, which correspond to the nonrotating parts and the rotating parts, respectively [152]. Thus the spectrum components of the rotating parts can be eliminated and the focused ISAR image as well as the information of the extracted rotating parts can be obtained. Besides its application in image processing, the Hough transform was also applied to nonimage data and parameter estimation [153]. Its efficiency has been confirmed by comparison with the Least Square Method. Moreover, the Hough transform has been used to detect lines and curves in pictures [154], as well as for chirp detection [69].

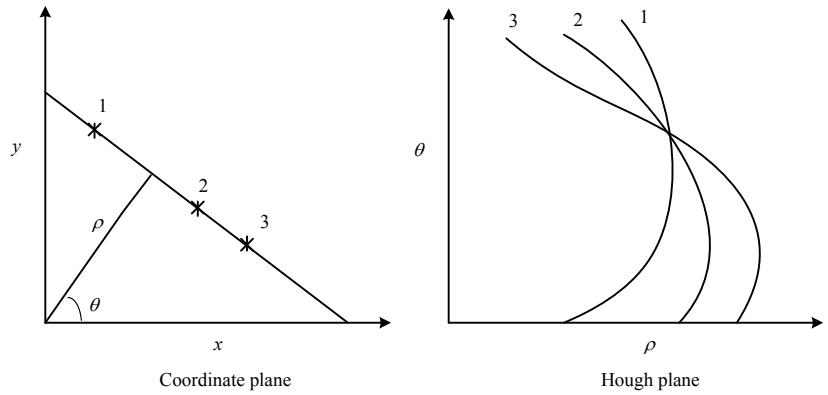

Figure 5.10: Illustration of Hough transform

In the time-frequency domain, the polar parameterization of a line can be

expressed as

$$x\cos\theta + y\sin\theta = \rho, \tag{5.3.3}$$

where ρ and θ are the distance and angle of the normal vector to the line from the origin, respectively. The Hough transform associates with each point (x, y) in the time-frequency domain with a sinusoid in the (ρ, θ) domain, as shown in Figure 5.10 [149]. If N points are concentrated along a straight line in the time-frequency domain, they will correspond to N sinusoidal curves intersecting at the same point in the (ρ, θ) domain. The integration along the line produces a maximum and its coordinates in the (ρ, θ) domain are directly related to the parameters of the lines. A comprehensive review on the Hough transform is available in [149].

The Hough transform combined with the WVD, known as the Wigner-Hough transform (WHT), is an effective tool to detect and estimate the parameters of the LFM signal [67]. After the chirp signal is represented with a two-dimensional image of straight lines by using the WVD, the Hough transform is employed to process the image to better reveal important features of the chirp signal for detection and estimation. The WHT of multicomponent chirp signals can also reduce the effects of cross terms on the final estimates [67].

It is noted that the WVD has an inherent noise threshold effect problem [37] and therefore cannot give satisfactory representations of the LFM signals in heavy noises. As shown in Chapter 4, the LPP has a much better noise resistance capability than the WVD and is able to obtain desirable signal representations in the time-frequency domain even in a very low input SNR environment. Therefore, when the LPP is used for the image formation to detect the chirp signals with very low SNRs, the Hough transform, which converts

a difficult global detection problem in image space into a more easily solved local peak detection problem in the parameter space, becomes more effective. The algorithm proposed for the detection of chirp signals, with the unknown parameters and embedded in AWGN, consists of the following steps:

(a) estimate ω_1 for the LPFT using the PTFT;

(b) compute the LPP of the signal;

(c) compute the Hough transform of the LPP;

(d) compare the values achieved by the Hough transform with a given threshold for each pair of ρ and θ.

When a certain value exceeds the threshold, a detection is made on the presence of a chirp signal.

5.3.2.2 Time-Frequency Filtering

In many practical applications, it is necessary to extract signals from noises. Since the signals may overlap either in the time domain or in the frequency domain, a conventional time-domain windowing or frequency-domain windowing may not be adequate. However, under this situation we can use the time-frequency filtering to extract the useful signal information in the time-frequency domain and suppress the noise effect [18].

The time-frequency filtering has been used in many different applications. For instance, it has been used as an approach for sonar target classification [155], which is more robust to reverberation and background noise perturbations. Combined with the LPFT and STFT, the time-frequency filtering is

employed for jammer rejection in the spread spectrum communications to improve the desired signal receiving performances [52], as well as for nonstationary interference suppression in noise radar systems [117]. The time-frequency filtering is also applied to audio time-scale and pitch modification [156]. In [157], the concept of time-frequency filtering is extended to nonstationary space-varying filtering to demonstrate superiority over the space-invariant filters. The time-frequency filtering with the S-transform is explored in [158] to filter nonstationary signals in a better way than the Fourier-domain filtering. For multicomponent noisy signals, the S-method can be used as a tool for the filter's region of support estimation [159].

To design a time-frequency filter, we first need to estimate the instantaneous frequency of the signal, for example, based on peak detection in the time-frequency domain [18]. Then the time-frequency filtering, also known as the "mask", can be defined as

$$M(t,\omega) = \begin{cases} 1, & \text{for } (t,\omega) \in R \\ 0, & \text{for } (t,\omega) \notin R \end{cases} \tag{5.3.4}$$

where R is the instantaneous frequency region.

In the following, some simulations are given to show how the time-frequency filtering works. Various signals corrupted by AWGN with SNR = 0dB are considered, such as the sinusoidal FM signal, the parabolic FM signal, the signal with two parallel chirp components, and the signal with two cross chirp components. From Figure 5.11, it is observed that the time-frequency filtering can help to suppress the noise effect and extract the useful information.

In this application for LFM chirp detection, the time-frequency filtering is used for the representation in the time-frequency domain to obtain a much

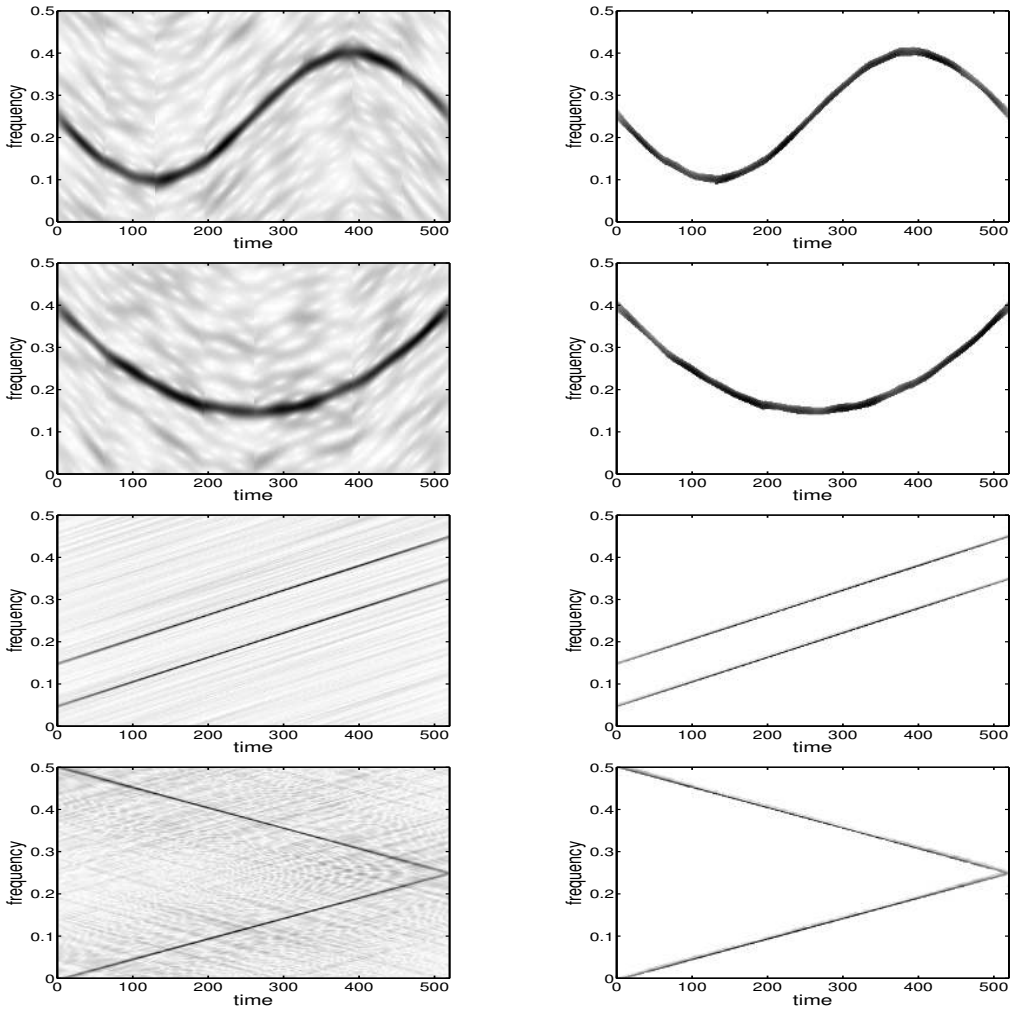

Figure 5.11: Illustration of the time-frequency filtering. The plots in the left column are the LPPs of the noisy signals, and the plots in the right column are the filtered LPP of the corresponding signals, using the time-frequency filtering.

cleaner representation. Then the filtered representation is followed by the Hough transform for chirp detection. Applying the time-frequency filtering to the time-frequency representation can help to filter out the points in the time-frequency domain which have relatively small amplitude and do not contribute much to the detection. Considerable Hough transform effort can be saved when these points are filtered out, which therefore can greatly reduce the computation complexity of the detection. This time-frequency filtering operation is similar to the idea

of introducing the primary threshold in the detection, as shown in [69, 151].

5.3.3 Simulations

In this section, signals in AWGN and impulsive noise are processed respectively to demonstrate the merits of the LHT. Various level of SNR are used for signals in additive white noise and the impulsive noise. With different SNRs in the simulations we try to illustrate that the methods can still provide good performance even with the low SNRs. With the help of the time-frequency filtering, the corresponding computation complexity of detection can be minimized while the performances remain almost the same. It should be noted that in this section ω_1 is estimated in presence of the stated noise, using the maximum likelihood estimator PTFT which has been introduced in Chapter 2.

5.3.3.1 Signals in Additive White Gaussian Noise

We will consider a few signals containing mono- and multi-component chirps corrupted by AWGN with various values of SNR.

(a). Monocomponent chirp signal

Consider a monocomponent 256-point chirp signal

$$s(t) = e^{j2\pi(0.00078t^2)}. \tag{5.3.5}$$

Figure 5.12 shows the PWVD and the LPP of the monocomponent chirp signal defined in (5.3.5) with SNR $= -10$dB. It is seen that the LPP achieves a much better noise suppression than the PWVD for a usable representation

in the time-frequency domain. The PWHT and LHT of this signal are given in Figure 5.13 to show that the LHT has a much larger noise margin than the PWHT for correctly detecting the chirp component. When the time-frequency filtering is employed to suppress the noise effect, the representation of the chirp in Figure 5.12(b) becomes much cleaner, and therefore the noise shown in Figure 5.13(b) can be further suppressed.

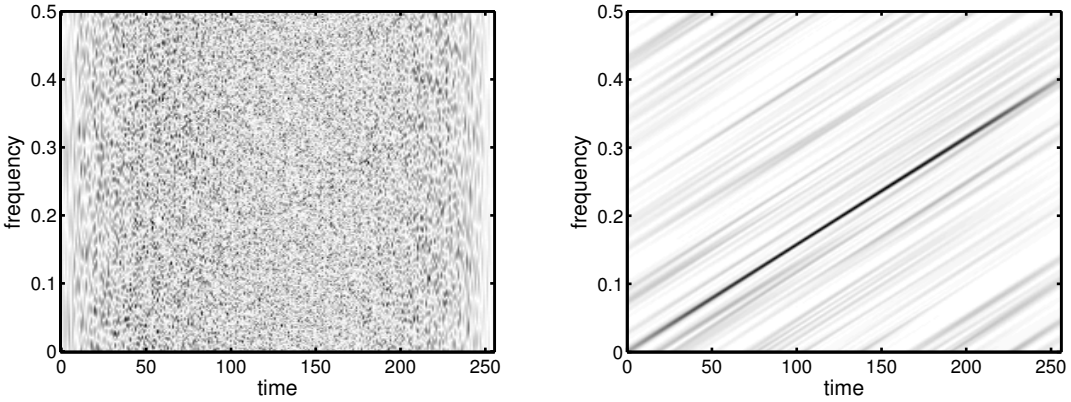

(a) PWVD (b) LPP

Figure 5.12: The PWVD and LPP of a monocomponent chirp signal (SNR = −10dB).

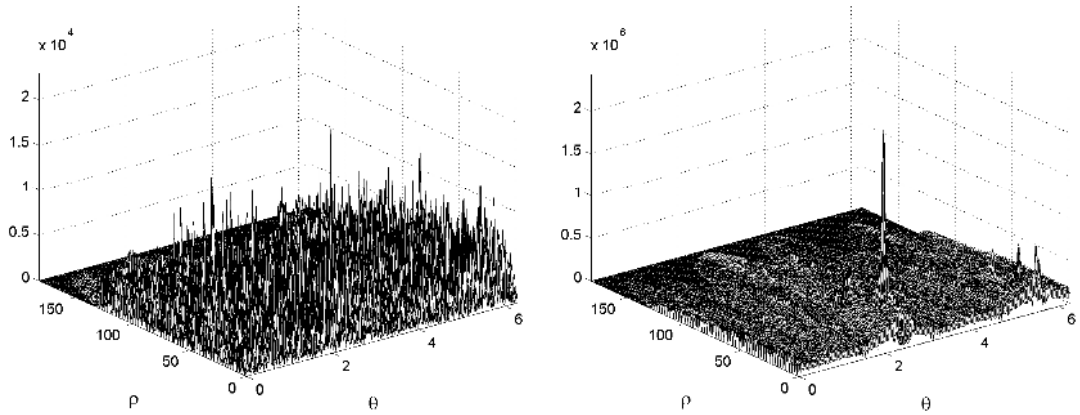

(a) PWHT (b) LHT

Figure 5.13: The PWHT and LHT of a monocomponent chirp signal (SNR = −10dB)

We will evaluate the performance in terms of the probability of detection, P_d, for the signal in (5.3.5) embedded in AWGN with different SNRs. Let us define a grid containing 3 point by 3 point as the expected location of the peak. A detection is successful when the peak above the threshold is within this grid. We also assume that the probability of false alarm is 10^{-2}, from which the threshold of detection can be calculated. Theoretical analysis of the Hough detector was presented in [69]. For the convenience of readers, Appendix in Section 5.5 summarizes the main details of theoretically deriving the detection probability.

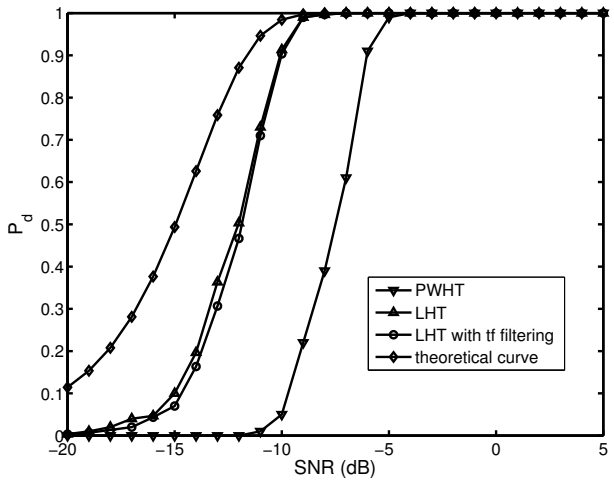

Figure 5.14: Detection performance comparison of LHT and PWHT under the probability of false alarm 10^{-2}.

From Figure 5.14, it is observed that the performance of the LHT for $P_d > 0.99$ is close to that of the theory. For signal with a low SNR between -6 and -12dB, the probability of detection using the LHT is much higher than that of the PWHT. Compared with the LHT without time-frequency filtering, the detection performance of the LHT with the time-frequency filtering is almost the same. However, with the help of the time-frequency filtering, the computation complexity is greatly reduced, which will be shown later. Since the

time-frequency filtering helps to filter out the points that do not contribute much to the detection, the LHT with the time-frequency filtering can save the computation time but cannot further improve the detection performance, compared with the LHT without the time-frequency filtering.

It should be noted that the probability of detection, P_d, is related to the signal length. We can always increase the signal length and/or increase the SNR to improve the detection performance.

(b). Multicomponent chirp signal

To further demonstrate the advantage of the LHT, let us now consider a two-component chirp signal,

$$s(t) = e^{j2\pi(0.000488t^2)} + e^{j2\pi(0.2t-0.000488t^2)}$$

with SNR $= -8$dB.

Figure 5.15 shows that this signal is almost invisible from its PWVD, but the two chirp components are clearly seen with some noise disturbances by using the LPP. The PWHT and LHT of this signal are shown in Figure 5.16. The PWHT can hardly be used for a correct detection of the two chirp components because it has many peaks of similar magnitudes. However, there exist two peaks with a large noise margin in the LHT for correct detection of the two chirp components. Therefore, the LHT gives a significantly better peak detection than the PWHT for multicomponent chirp signals corrupted by heavy noises.

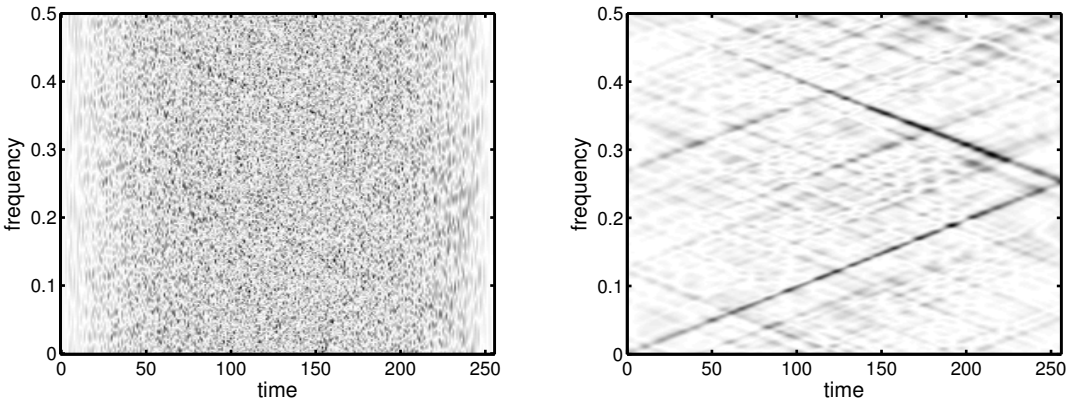

(a) PWVD (b) LPP

Figure 5.15: The PWVD and LPP of a multicomponent chirp signal (SNR = −8dB).

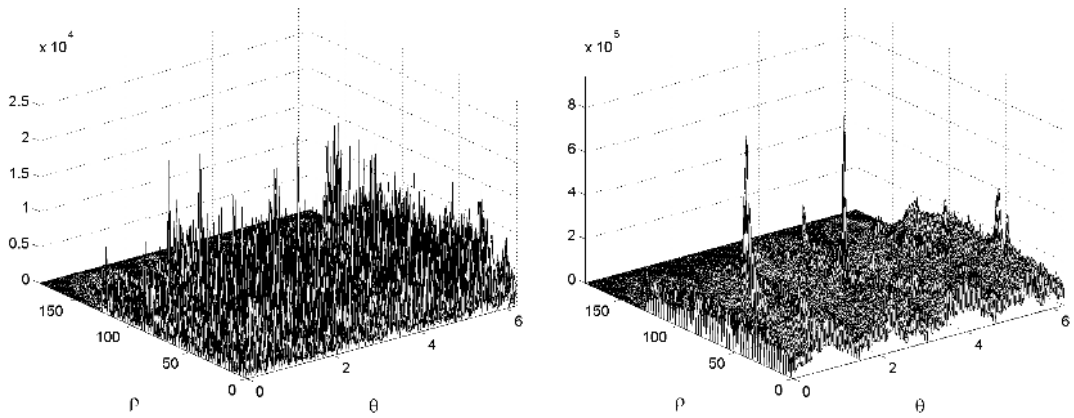

(a) PWHT (b) LHT

Figure 5.16: The PWHT and LHT of a multicomponent chirp signal (SNR = −8dB).

It should be noted that compared with the PWVD, the LPFT or LPP generally needs more computation time since it employs the PTFT to estimate the extra parameter ω_1. However, the LPP can achieve a much clearer representation for signals in a heavy noise environment compared with the PWVD. This advantage has a direct impact on the computation of Hough transform of these time-frequency representations. For the monocomponent chirp signal

discussed in Figures 5.12 and 5.13, for example, the computational times required by the LHT and PWHT are 7.2175s and 9.0718s, respectively. For the multicomponent chirp signal related to Figures 5.15 and 5.16, the computation times of the LHT and the PWHT are 9.2815s and 9.2433s, respectively. The above reported computation times on the LHT and the PWHT were the averages of 50 measurements of the computations. The reason that the LHT needs less computation time than PWHT is that although the LPP needs more computation time than the PWVD, the Hough transform generally needs a much less computational complexity for the cleaner images provided by the LPP. The computational complexity of the LHT can be further reduced with the help of the time-frequency filtering. For the same monocomponent and multicomponent signals, the computation times required by the LHT with the time-frequency filtering are reduced to 3.7473s and 5.6860s respectively. Besides, the LHT with time-frequency filtering can also achieve comparable performance as the LHT without filtering.

5.3.3.2 Signals in Impulsive Noise

In many practical applications involving communications and imaging, signals are often corrupted by impulsive noise. To better process signals in the impulsive noise environment, the robust M-estimation [160] and the robust estimation in the marginal-median form [73] are proposed. However, because they use the iterative and sorting procedures, respectively, these two robust methods require heavy computational complexities. Clipper is a standard tool to deal with impulsive noises due to its natural ability to eliminate the outliers with a simple computational procedure [161]. The clipper method has been compared with

other methods such as the M-estimation and L-estimation based forms of signal transforms in [162]. It has been shown that the clipper method can provide similar performance as the M-estimation and L-estimation based methods, and reduce the computation complexity significantly. Thus in this section for the signals corrupted by impulsive noise, we first use the clipper to reduce the effect of impulsive noise before applying the LHT to detect the chirp signals. In this way, the LHT, which was previously used for signals in AWGN, can be used to process signals corrupted by impulsive noises.

Let us consider the α-stable impulsive noise $n(t) = \alpha(w_1^3(t) + w_2^3(t))$, where $w_1(t)$ and $w_2(t)$ are independent Gaussian random variables with unit variances. The variance of the impulsive noise is $\sigma_n^2 = 30\alpha^2$ [163], leading to a SNR of -28.75dB when $\alpha = 5$, for example.

In Figures 5.17 to 5.20, the mono- and multi-component signals are corrupted by the impulsive noises with $\alpha = 5$ and 3.5, respectively. From these figures, it is observed that the LPPs of the clipped mono- and multi-component chirp signals achieve a better representation than their PWVDs. Thus the corresponding LHTs can provide a more accurate peak detection of the chirp components than the PWHT. Since the clipping method does not increase the computational complexity significantly, the LPPs of the clipped signals require almost the same computation time as those for the signals corrupted by the AWGN. For the monocomponent chirp signal mentioned above, the LHT and the PWHT require the computation times 8.6674s and 9.9389s, respectively. For the multicomponent chirp signal, the computation times required by the LHT and PWHT are 10.2533s and 9.7493s, respectively. With the time-frequency filtering, the computation complexity can be reduced to 3.9820s and 4.1139s,

respectively.

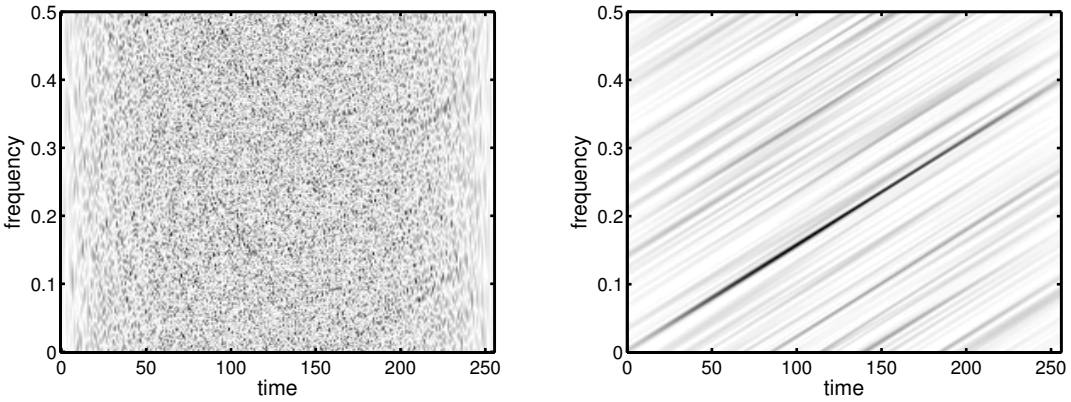

(a) PWVD (b) LPP

Figure 5.17: The PWVD and LPP of a monocomponent chirp signal in impulsive noise ($\alpha = 5$).

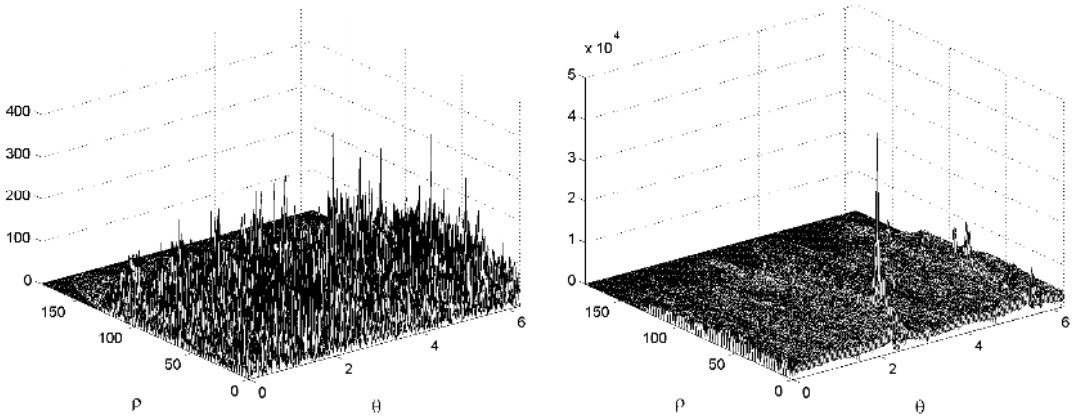

(a) PWHT (b) LHT

Figure 5.18: The PWHT and LHT of a monocomponent chirp signal in impulsive noise ($\alpha = 5$).

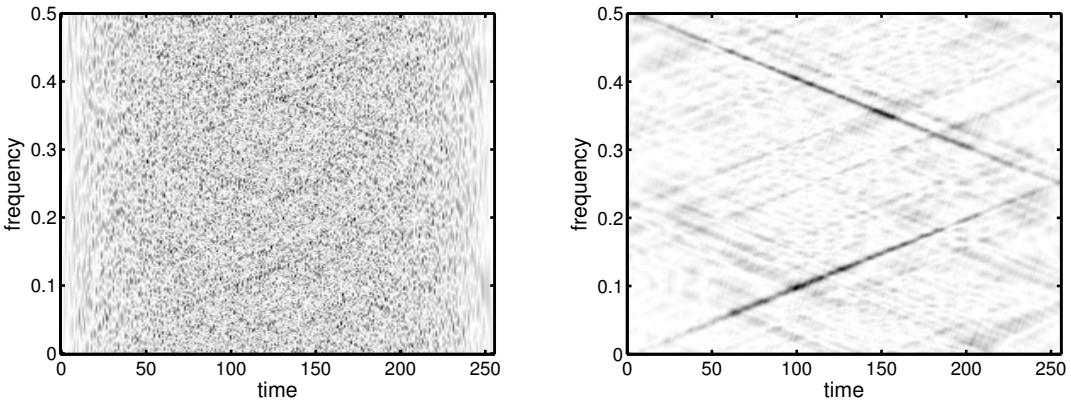

(a) PWVD (b) LPP

Figure 5.19: The PWVD and LPP of a multicomponent chirp signal in impulsive noise ($\alpha = 3.5$)

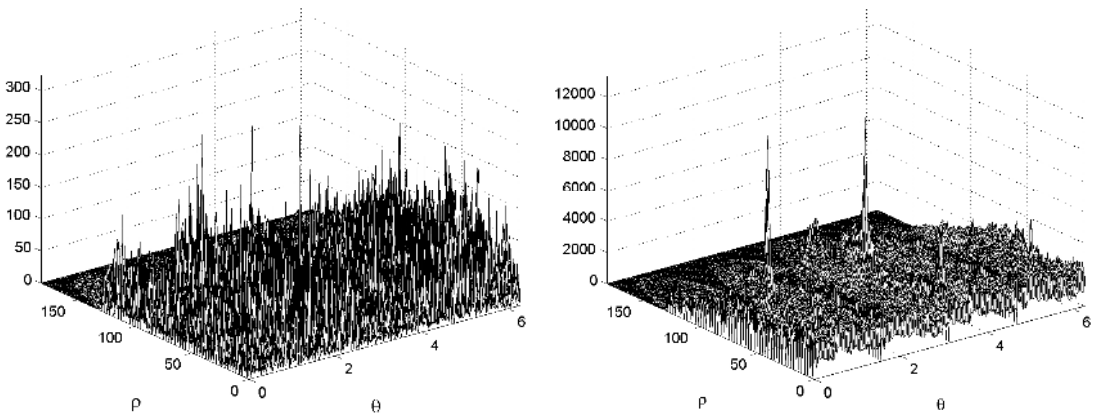

(a) PWHT (b) LHT

Figure 5.20: The PWHT and LHT of a multicomponent chirp signal in impulsive noise ($\alpha = 3.5$)

For comparisons, the results of the PWVD and the LPP without the use of clipper are demonstrated in Figure 5.21 and Figure 5.22 for the monocomponent signal and the multicomponent signal, respectively. It can be seen that without the use of the clipper, neither the PWVD nor the LPP can provide clean representation for the signals corrupted by the impulsive noise. This is because that without the clipper the standard PWVD and LPP are not the proper represen-

tations to process signals corrupted by the impulsive noise, as demonstrated in literature [74]. Accordingly, the PWHT and LHT cannot provide useful peak detection for monocomponent and multicomponent chirp signals corrupted by heavy impulsive noises.

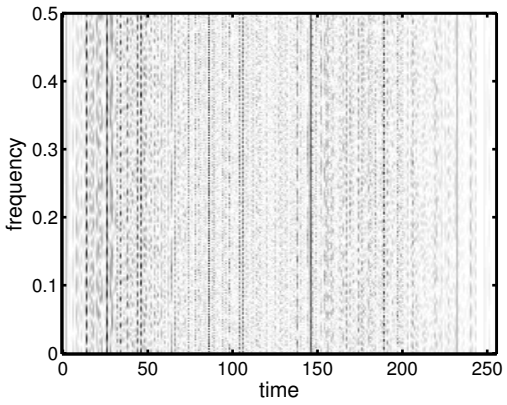

(a) PWVD

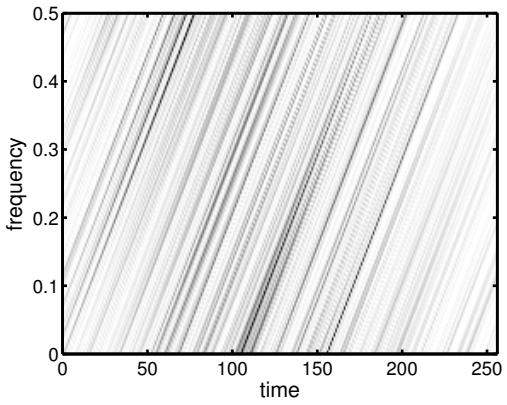

(b) LPP

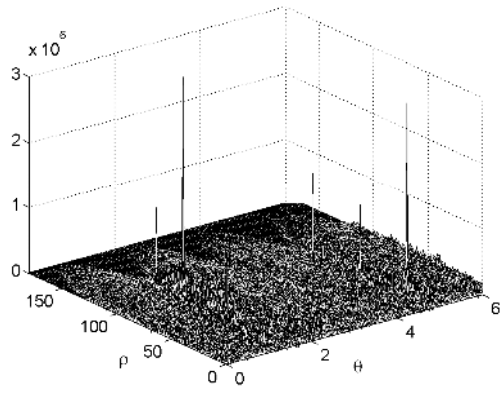

(c) PWHT

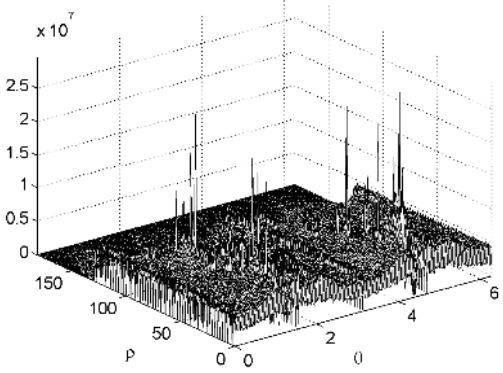

(d) LHT

Figure 5.21: The PWVD, LPP, PWHT and LHT of a monocomponent chirp signal in impulsive noise ($\alpha = 5$), without the use of clipper.

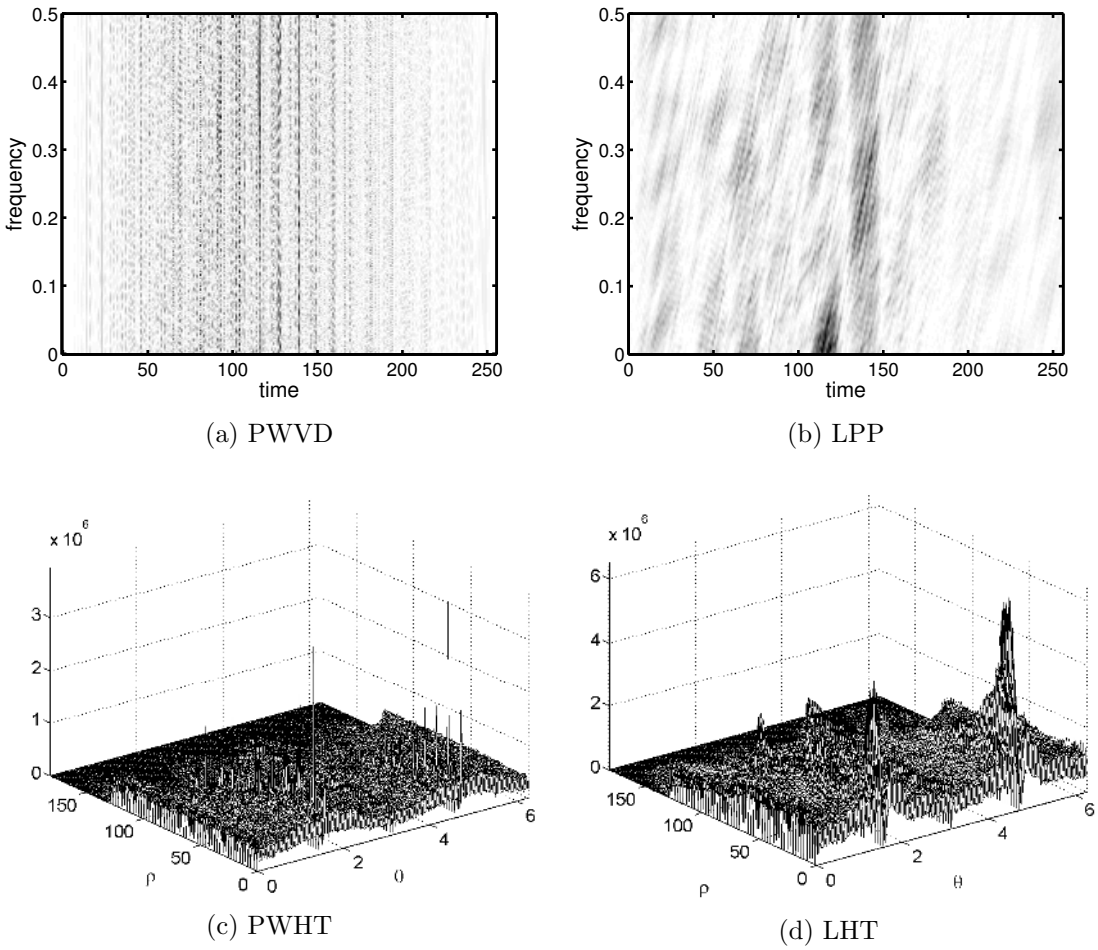

(a) PWVD (b) LPP

(c) PWHT (d) LHT

Figure 5.22: The PWVD, LPP, PWHT and LHT of a multicomponent chirp signal in impulsive noise ($\alpha = 3.5$), without the use of clipper.

5.4 Conclusion

Application examples in ISAR imaging and LFM signal detection are presented to show the advantage of the LPFT and verify the theoretical SNR analysis of the LPFT. It shows that compared with the FT and the STFT, the resolution of the ISAR images is improved by using the LPFT. Furthermore, the improvement on imaging performance can be achieved with reduced computa-

tional complexity by using the non-overlapping approach. Since it can provide a better noise suppression than the PWVD, the LPP is a better tool to be combined with the Hough transform to detect the LFM signals. Numerical examples show that, compared with the PWHT, the LHT achieves significantly better performances for signals corrupted by heavy AWGN and impulsive noise. In addition, the computation time needed by the LHT can be further reduced by using the time-frequency filtering.

5.5 Appendix: Analytical Performance of the Hough Detector

Based on the materials given in [69], this appendix presents the theoretical derivation of the probability of detection for the convenience of the readers. The detection of chirp signal can be symbolically modelled as

$$\begin{aligned} H_0 : x_n &= w_n \\ H_1 : x_n &= w_n + Ae^{j2\pi(f+kn)n}, \end{aligned}$$

where H_0 is the noise-only hypothesis, H_1 is the signal-present hypothesis for $n = 0, 1, \ldots, L_s - 1$, and L_s is the length of the signal. The complex noise term, $\{w_n\}$, is assumed to be independent identically distributed (i.i.d.) and with both real and imaginary parts having distribution $\mathcal{N}(0, 1)$.

Assuming all the points in the Hough plane are independent, the amplitude of the point under H_0 has the chi-square distribution χ^2_{2L} with $2L$ degrees of freedom, where L is the number of FFTs in the time-frequency domain. The amplitude of the point, under H_1, corresponding to the signal in the Hough

plane has the noncentral chi-square distribution with $2L$ degrees of freedom and the noncentrality parameter as $NE(A)^2L$, where N is the FFT length in the time-frequency domain; other point distributions are same as those under H_0.

With the given probability of false detection, P_{fa}, the detection threshold τ can be calculated as

$$\tau = {G_{2L}^2}^{-1}((1 - P_{fa})^{1/K}) \tag{5.5.1}$$

where G_{2L}^2 is the cumulative distribution function of the chi-square distribution with $2L$ degrees of freedom and K is the number of active points in the Hough plane. An active point is that in the Hough plane which has a corresponding line in the data plane. For the given threshold τ, the probability of detection can be calculated as

$$P_d = \int_{\tau}^{\infty} f(t)dt \tag{5.5.2}$$

where $f(t) = \chi_{2L}^{\prime 2}(NE(A)^2L)$.

Chapter 6

The Reassigned Local Polynomial Periodogram

6.1 Introduction

To better process the time-varying signals, the essential requirement of a good TFR is to obtain a sufficient concentration of the signal components to represent the signal as accurate as possible. As introduced in Chapter 1, although the LPFT can provide concentrated presentation for the time-varying signals, ways to further improve the concentration are always desired. Therefore in this chapter we will focus on the ways to further improve the concentration of the LPFT.

The reassignment method is an effective operation to improve signal concentration in the time-frequency domain. It has been generalized to deal with the bilinear time-frequency and time-scale distributions [70], the affine class [71] and S-method [72]. The reassignment method has also been employed in

many practical applications. It was combined with the multi-tapering for better estimating time-varying spectra with possibly localized components [164]. In [165] the reassignment method was adopted to improve the bandwidth-enhanced additive sound model to produce a sharper and more robust additive representation. Moreover, the reassignment method was used to process broadband scattering data from an open-ended waveguide cavity [166]. It was also applied to study the micro-Doppler features of a moving human [167]. Furthermore, it has been used in many other areas, such as speech analysis [168], musical transcription [169, 170] and seismic analysis [171]. Recursive algorithms were provided in [172, 173] to make the reassignment methods well suited for real-time implementations. More detailed information on the reassignment method can be found in [70, 174, 175].

Although the reassignment method generally provides a higher concentration in the time-frequency domain, it cannot remove the cross terms [70]. Therefore, selection of a proper kernel for a TFR becomes essential to the reassignment method to achieve both high concentration and low cross terms between the signal components. In general, a more readable reassigned TFR can be obtained if the kernel of a TFR better fits the analyzed signal. As introduced in Chapter 2, the LPFT has a kernel that is able to more accurately describe the time-varying signals. Furthermore, the LPFT is a linear transform that has no cross terms between signal components. The local polynomial periodogram (LPP), which is the modulus square of the LPFT, is the energy distribution of the LPFT. Similar to the spectrogram (SP) which is the modulus square of the STFT, the LPP is a bilinear transform, therefore it has the cross terms. Since the LPFT is a generalization of the STFT, the cross terms in the LPP is similar to that in the SP. For multicomponent signals, unlike the cross terms in

the WVD, the cross terms in the SP, which depend on the signal structure and the window used, occur at the intersection of their respective STFT space [176]. Since the LPFT can achieve higher resolution than the STFT, the cross terms in the LPP is also much less conspicuous than the SP. The LPP is free from the cross terms as long as the signal components do not intersect and the window length used in the LPP is sufficient [177]. Therefore the reassignment method based on the LPP is able to give an improved resolution for signals containing more than one closely located components. The second-order LPFT, with one extra parameter ω_1, is particularly suitable to process chirp signals. It can also be used to process higher-order time-varying signals with a small window to ensure that each signal segment is approximated as a chirp signal. Therefore in this chapter, the reassignment method is applied to the LPP, which is the reassigned LPP (RLPP), to deal with various time-varying signals with a better concentrated representation.

The rest of the chapter is organized as follows. Section 6.2 provides some related background information on the reassigned method. Section 6.3 mathematically defines the RLPP and investigates its properties. Numerical examples for some of the properties and performance improvements are also provided in Section 6.3. The reassignment method is extended to the robust LPP in Section 6.4. The performance comparisons among the LPP-related methods are given in Section 6.5. Conclusions are given in Section 6.6. The expressions of the reassignment operators for the RLPP and some of its properties are proved in Section 6.7.

6.2 Review on the Reassignment Method

As introduced in Chapter 2, the spectrogram (SP), WVD, smoothed pseudo WVD (SPWVD) and many other bilinear counterparts can be written in a general form, known as the Cohen's class, expressed as [60]

$$\mathrm{TFR}(x;t,\omega) = \frac{1}{4\pi^2}\int\int \phi(u,\Omega)\mathrm{WVD}(x;t-u,\omega-\Omega)dud\Omega, \quad (6.2.1)$$

where $\mathrm{WVD}(x;t,\omega)$ is the WVD of a given signal $x(t)$ and $\phi(u,\Omega)$ is the distribution kernel which determines the distribution and its properties. Many members in the Cohen's class are able to suppress the cross terms of the WVD, but with undesirable effects of broadening the signal components in the time-frequency domain. In order to minimize such undesirable effects, a reassigned time-frequency representation (RTFR) is used to improve the concentration of the signal component by reallocating its energy distribution in the time-frequency domain. By moving the attribution point of the average operation to the gravitational center of the energy contribution, the RTFR is defined as

$$\begin{aligned}\mathrm{RTFR}(x;t',\omega') = &\int\int \mathrm{TFR}(x;t,\omega) \\ &\cdot\delta(t'-\hat{t}(x;t,\omega))\delta(\omega'-\hat{\omega}(x;t,\omega))dtd\omega,\end{aligned} \quad (6.2.2)$$

where $\hat{t}(x;t,\omega)$ and $\hat{\omega}(x;t,\omega)$ are the coordinates of the gravitational center, by way of analogy to a mass distribution. In [178] these coordinates are demonstrated to represent the center of gravity of Rihaczek's complex energy distri-

bution. They are also known as reassignment operators, defined as [70]:

$$\hat{t}(x;t,\omega) = t - \frac{\int\int u\ \phi(u,\Omega)\mathrm{WVD}(x;t-u,\omega-\Omega)dud\Omega}{\int\int \phi(u,\Omega)\mathrm{WVD}(x;t-u,\omega-\Omega)dud\Omega}, \quad (6.2.3)$$

$$\hat{\omega}(x;t,\omega) = \omega - \frac{\int\int \Omega\ \phi(u,\Omega)\mathrm{WVD}(x;t-u,\omega-\Omega)dud\Omega}{\int\int \phi(u,\Omega)\mathrm{WVD}(x;t-u,\omega-\Omega)dud\Omega}. \quad (6.2.4)$$

For the well known SP, the reassignment operators of its reassigned form, the RSP, are expressed as [174],

$$\begin{aligned}\hat{t}(x;t,\omega) &= t - \frac{\int\int u\ \mathrm{WVD}\left(h;u,\Omega\right)\mathrm{WVD}\left(x;t-u,\omega-\Omega\right)dud\Omega}{\int\int \mathrm{WVD}\left(h;u,\Omega\right)\mathrm{WVD}\left(x;t-u,\omega-\Omega\right)dud\Omega} \\ &= t - \mathrm{Re}\left\{\frac{\mathrm{STFT}_{Th}(x;t,\omega)}{\mathrm{STFT}_{h}(x;t,\omega)}\right\} \quad (6.2.5)\end{aligned}$$

$$\begin{aligned}\hat{\omega}(x;t,\omega) &= \omega - \frac{\int\int \Omega\ \mathrm{WVD}\left(h;u,\Omega\right)\mathrm{WVD}\left(x;t-u,\omega-\Omega\right)dud\Omega}{\int\int \mathrm{WVD}\left(h;u,\Omega\right)\mathrm{WVD}\left(x;t-u,\omega-\Omega\right)dud\Omega} \\ &= \omega + \mathrm{Im}\left\{\frac{\mathrm{STFT}_{Dh}(x;t,\omega)}{\mathrm{STFT}_{h}(x;t,\omega)}\right\}, \quad (6.2.6)\end{aligned}$$

where Re and Im indicate the real part and imaginary part, respectively, and the subscripts h, Th and Dh indicate that the associated STFTs use the window $h(t)$, the time ramped window $t \cdot h(t)$, and the first derivative of the window $\frac{dh(t)}{dt}$, respectively.

6.3 The Reassigned LPP

This section focuses on the theoretical studies of the RLPP. The definition of the RLPP is given and its properties are presented with mathematical proofs. It is

shown that the RLPP has several interesting properties such as non-negativity, non-bilinearity, time and frequency shifts invariance, time-scaling, time-folding, symmetry, and energy conservation. In particular, our analysis shows that the RLPP is able to perfectly localize the chirp and impulse signals, which proves the effectiveness of the RLPP on improving signal concentration. The proposed RLPP has the same property as that of the RSP and the reassigned smoothed pseudo WVD (RSPWVD) to localize the chirp and impulse signals. It is well known that the RSPWVD cannot mitigate the cross terms resulted from the WVD and that the RSP cannot separate closely localized chirp components in the time-frequency domain. In contrast, because the use of the extra parameter for the phase of the signal helps to obtain a higher resolution in the time-frequency domain, the cross terms in the RLPP are negligible and the RLPP is also able to provide a better resolution than the RSP for the closely located chirp components. Due to these desirable properties, it will be shown in the simulation that compared with the RSP and RSPWVD, the RLPP achieves a better signal concentration for chirp signals, especially for closely located chirps, as well as for higher-order PPSs and other time-varying signals.

6.3.1 Definition of the Reassigned LPP

We will consider the definitions of the reassignment methods based on the second-order LPP. Since ω_1 can be estimated from the PTFT, the LPP is a bilinear TFR and the reassignment method can be extended to the LPP to obtain performance improvement [179]. Therefore, the RLPP is defined as

$$\begin{aligned} \mathrm{RLPP}(x;t',\omega') &= \int\int \mathrm{LPP}\left(x;t,\omega\right)\delta\left(t'-\hat{t}(x;t,\omega)\right) \\ &\quad \cdot\delta\left(\omega'-\hat{\omega}\left(x;t,\omega\right)\right)dtd\omega. \end{aligned} \tag{6.3.1}$$

The expressions of the reassignment operators for the RLPP are given in (6.3.2) and (6.3.3), and their proofs are presented in Appendix in Section 6.7.1.

$$\begin{aligned}
&\hat{t}(x;t,\omega) \\
&= t - \frac{\int\int u\ \mathrm{WVD}\left(h;u,-\frac{\omega_1}{2}u+\Omega\right)\mathrm{WVD}\left(x;t-u,\omega-\frac{\omega_1}{2}u-\Omega\right)dud\Omega}{\int\int \mathrm{WVD}\left(h;u,-\frac{\omega_1}{2}u+\Omega\right)\mathrm{WVD}\left(x;t-u,\omega-\frac{\omega_1}{2}u-\Omega\right)dud\Omega} \\
&= t - \mathrm{Re}\left\{\frac{\mathrm{LPFT}_{Th}(x;t,\omega)\ \mathrm{LPFT}_h^*(x;t,\omega)}{|\mathrm{LPFT}_h(x;t,\omega)|^2}\right\} \\
&= t - \mathrm{Re}\left\{\frac{\mathrm{LPFT}_{Th}(x;t,\omega)}{\mathrm{LPFT}_h(x;t,\omega)}\right\}
\end{aligned} \tag{6.3.2}$$

$$\begin{aligned}
&\hat{\omega}(x;t,\omega) \\
&= \omega - \frac{\int\int \left\{\begin{array}{l}\left(\Omega-\frac{\omega_1}{2}u\right)\ \mathrm{WVD}\left(h;u,-\frac{\omega_1}{2}u+\Omega\right) \\ \cdot\mathrm{WVD}\left(x;t-u,\omega-\frac{\omega_1}{2}u-\Omega\right)\end{array}\right\}dud\Omega}{\int\int \mathrm{WVD}\left(h;u,-\frac{\omega_1}{2}u+\Omega\right)\mathrm{WVD}\left(x;t-u,\omega-\frac{\omega_1}{2}u-\Omega\right)dud\Omega} \\
&= \omega + \mathrm{Im}\left\{\frac{\mathrm{LPFT}_{Dh}(x;t,\omega)\ \mathrm{LPFT}_h^*(x;t,\omega)}{|\mathrm{LPFT}_h(x;t,\omega)|^2}\right\} \\
&= \omega + \mathrm{Im}\left\{\frac{\mathrm{LPFT}_{Dh}(x;t,\omega)}{\mathrm{LPFT}_h(x;t,\omega)}\right\}
\end{aligned} \tag{6.3.3}$$

Because the WVD is always real-valued, the reassignment operators in (6.3.2) and (6.3.3) are also real-valued. It is noted that when $\omega_1 = 0$, the LPFT becomes the STFT, and the reassignment operators of the LPP in (6.3.2) and (6.3.3) become those of the RSP as in (6.2.5) and (6.2.6).

6.3.2 Properties of the Reassigned LPP

The RLPP has a number of properties that can be derived from (6.3.2) and (6.3.3). Some of their proofs are presented in Appendix in Section 6.7.2.

(a) Non-negativity

Since the LPP is the square of the LPFT, the non-negativity is preserved so that the RLPP yields non-negative TFR. The non-negative distributions are preferred because they can be interpreted as true energy densities to assure accurate signal representation to be obtained.

(b) Non-bilinearity

Bilinear distributions are obtained by kernels that are functionally independent of the signal [34]. Because the reassignment operations depend on the signal, as seen in (6.3.2) and (6.3.3), the RLPP is not bilinear. However, it is noted that the bilinearity is sacrificed for the benefit of perfectly localizing the chirp and impulse signals.

(c) Time and frequency shifts invariance

Let us consider a signal $y(t) = x(t - t_0)e^{j\omega_0 t}$. According to the time and frequency shift properties of the WVD [34], it is known that

$$\mathrm{WVD}(y; t, \omega) = \mathrm{WVD}(x; t - t_0, \omega - \omega_0).$$

Thus

$$\hat{t}(y; t, \omega) = \hat{t}(x; t - t_0; \omega - \omega_0) + t_0,$$

$$\hat{\omega}(y; t, \omega) = \hat{\omega}(x; t - t_0; \omega - \omega_0) + \omega_0,$$

lead to

$$\mathrm{RLPP}(y; t', \omega') = \mathrm{RLPP}(x; t' - t_0, \omega' - \omega_0),$$

which means that when the signal is shifted in time and/or frequency domain, the reassignment operators in (6.3.2) and (6.3.3), and the associated RLPP are

shifted accordingly.

(d) Time-scaling property

For a signal $y(t) = x(at)$, where a is a non-zero constant, the WVD of $y(t)$ becomes [34]

$$\mathrm{WVD}(y; t, \omega) = \frac{1}{|a|}\mathrm{WVD}(x; at, \frac{\omega}{a}).$$

Applying this property to (6.3.2) and (6.3.3), we have

$$\hat{t}(y; t, \omega) = \frac{1}{a}\hat{t}(x; at, \frac{\omega}{a}),$$

$$\hat{\omega}(y; t, \omega) = a\hat{\omega}(x; at, \frac{\omega}{a}).$$

Thus

$$\mathrm{RLPP}(y; t', \omega') = \frac{1}{|a|}\mathrm{RLPP}(x; at', \frac{\omega'}{a}).$$

It means that the time-scaled signal with a constant $|a| > 1$ has an RLPP that is reduced in magnitude, squeezed in the time domain and expanded in the frequency domain. Similarly, the RLPP is increased in magnitude, expanded in the time domain and squeezed in the frequency domain when $0 < |a| < 1$.

Based on the above time-scaling property, when $a = -1$, i.e., $y(t) = x(-t)$, we have

$$\hat{t}(y; t, \omega) = -\hat{t}(x; -t, -\omega),$$

$$\hat{\omega}(y; t, \omega) = -\hat{\omega}(x; -t, -\omega).$$

Thus

$$\mathrm{RLPP}(y; t', \omega') = \mathrm{RLPP}(x; -t', -\omega'),$$

which shows that the RLPP of a time-folded signal is the folded version of the RLPP of the original signal in both time and frequency domains.

(e) Symmetry

When the signal is an even or odd function, i.e., $x(t) = x(-t)$ or $x(t) = -x(-t)$, based on the property of the WVD, it is known that for both cases,

$$\mathrm{WVD}(x;t,\omega) = \mathrm{WVD}(x;-t,-\omega).$$

Therefore we can easily have

$$\hat{t}(x;t,\omega) = -\hat{t}(x;-t,-\omega),$$

$$\hat{\omega}(x;t,\omega) = -\hat{\omega}(x;-t,-\omega).$$

Thus

$$\mathrm{RLPP}(x;t',\omega') = \mathrm{RLPP}(x;-t',-\omega'),$$

which means that when the signal $x(t)$ is even or odd symmetrical, the RLPP is also symmetrical in time and frequency domains.

(f) Energy conservation

The energy reallocation by the RLPP is consistent with the energy conservation, i.e.,

$$\int\int \mathrm{RLPP}(x;t',\omega')dt'd\omega' = \int |x(t)|^2 dt,$$

when

$$\int\int \mathrm{WVD}\left(h;u,-\frac{\omega_1}{2}u+\Omega\right)dud\Omega = 1.$$

This property shows that the signal energy in the time-frequency domain after reassignment operation is equal to the energy of the signal in the time domain provided that the window function $h(t)$ is of unit energy.

(g) Perfect localization on chirp and impulse signals

For a chirp signal $x(t) = Ae^{j(\omega_0 t+\alpha t^2/2)}$, we have

$$\mathrm{WVD}(x;t,\omega) = A^2\delta(\omega-\omega_0-\alpha t).$$

When ω_1 is estimated exactly, we have

$$\hat{\omega}(x;t,\omega) = \omega_0+\alpha t,$$

which is exactly the instantaneous frequency (IF) of the chirp signal. Thus

$$\mathrm{RLPP}(x;t',\omega') = \int\int \mathrm{LPP}(x;t,\omega)\delta(\omega'-\omega_0-\alpha t)\delta\left[t'-\hat{t}(x;t,\omega)\right]dtd\omega.$$

It shows that with ω_1 estimated exactly, the RLPP of a chirp signal is totally concentrated along the instantaneous frequency of the signal, that is

$$\omega' = \omega_0+\alpha t.$$

For an impulse signal $x(t) = A\delta(t-t_0)$, we have

$$\mathrm{WVD}(x;t,\omega) = A^2\delta(t-t_0),$$

and $\hat{t}(x;t,\omega) = t_0$. Thus

$$\mathrm{RLPP}(x;t',\omega') = \delta(t'-t_0)\int\int \mathrm{LPP}\left(x;t,\omega\right)\delta\left[\omega'-\hat{\omega}\left(x;t,\omega\right)\right]dtd\omega,$$

which demonstrates that the RLPP of an impulse signal is totally concentrated at the time of occurrence, that is $t' = t_0$.

The localization properties show that the RLPPs in (6.3.2) and (6.3.3) will always perfectly localize the chirp and impulse signals. It should be mentioned that there are very few representations having such properties. Among the Cohen's class, for instance, only the WVD perfectly localizes a chirp signal

on its instantaneous frequency [60]. However, the cross terms of the WVD deteriorate the obtained time-frequency representation.

There are two simplified variations of the RLPP. One is the reassigned LPP along the frequency direction (RfLPP), defined as:

$$\mathrm{RfLPP}(x;t,\omega') = \int \mathrm{LPP}(x;t,\omega)\delta[\omega' - \hat{\omega}(x;t,\omega)]d\omega, \qquad (6.3.4)$$

in which no reassignment is made in the time direction. The other one is the reassigned LPP along the time direction (RtLPP), defined as:

$$\mathrm{RtLPP}(x;t',\omega) = \int \mathrm{LPP}(x;t,\omega)\delta[t' - \hat{t}(x;t,\omega)]dt, \qquad (6.3.5)$$

in which no reassignment is made in the frequency direction.

The RfLPP and RtLPP share with the RLPP on the properties of non-negativity, non-bilinearity, time-scaling, energy conservation, time folding and symmetry. Moreover, the RfLPP particularly has the properties of frequency shift invariance and perfectly localizing the chirp components, while the RtLPP has the properties of time shift invariance and perfectly localizing the impulse components. It means that the RfLPP is responsible for perfectly localizing the chirps and the RtLPP is for perfectly localizing the impulse. It will be shown in the simulations that for signals containing only the chirp components, the RfLPP can achieve an even better signal concentration than the RLPP. The reason is as follows. In the RLPP, $\omega' = \omega_0 + \alpha t$ is obtained under the condition that the parameter ω_1 is estimated exactly. While in the RfLPP, even when ω_1 is not exactly estimated, we can still obtain $\omega' = \omega_0 + \alpha t$ with $t' = t$, which is exactly the IF of the chirp signal. Thus on the theoretical basis, the RfLPP of the chirp signal is able to represent chirp components more accurately than the RLPP with an easy implementation and less computation complexity, especially

for signals corrupted by the noise. On the other hand, if a signal only contains impulse components, the RtLPP, instead of the RLPP, can be used. For a signal containing both chirp and impulse components, the RLPP can generally achieve a good performance that is compromised for both types of signal components. These conclusions are to be confirmed in the simulations presented in the next section.

6.3.3 Simulations

This section presents simulation results demonstrating some properties of the RLPP and comparisons on the signal concentration performances achieved by using different reassigned methods. Although most simulations use chirp signals for the demonstration, considerations are also given for more general or higher-order signals. The window function used in this section is the Hamming window. The length of the signal is 520 points.

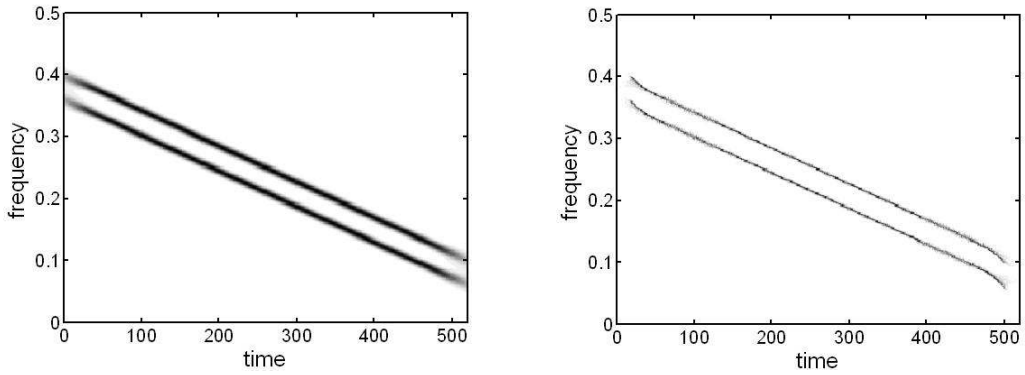

(a) LPP (b) RLPP

Figure 6.1: The LPP and RLPP of a signal with two parallel chirp components.

To demonstrate the property of perfectly localization, a signal

$$x(t) = e^{j2\pi(-0.00029t^2+0.4t)} + e^{j2\pi(-0.00029t^2+0.36t)},$$

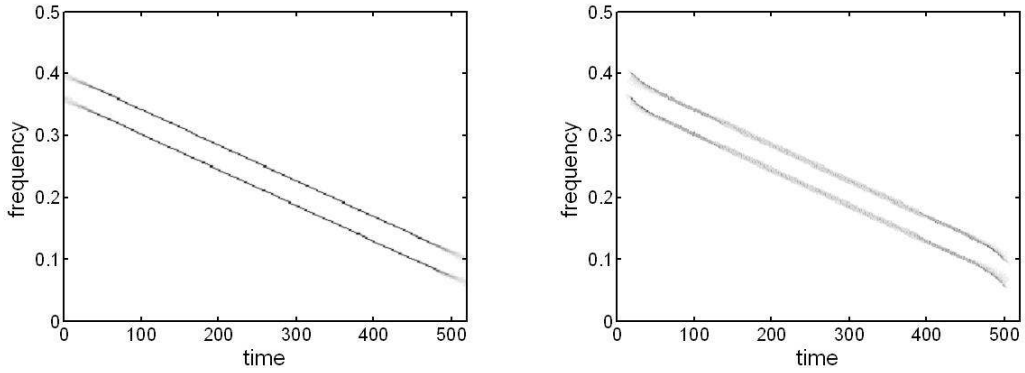

(a) RfLPP (b) RtLPP

Figure 6.2: Localizing chirp signals with RfLPP and RtLPP.

containing two parallel chirp components is used. Figure 6.1 shows its LPP and RLPP obtained by using a window of 131 points. It is observed that both the LPP and RLPP can localize the two chirp components. However, the RLPP achieves a significant improvement on signal concentration.

Figure 6.2 presents the RfLPP of the same signal as that used in Figure 6.1. It is seen that the RfLPP can perfectly localize the chirp signals as the RLPP in Figure 6.1(b) and the RtLPP becomes blurred. Both Figure 6.1(b) and Figure 6.2 (a) clearly show that the RLPP and RfLPP excellently localize the chirp components.

Figure 6.3 gives the LPP, RLPP, RfLPP and RtLPP of a signal containing two impulses, defined as $x(t) = \delta(t - 169.5) + \delta(t - 205.5)$. It clearly shows that the RLPP and the RtLPP achieves a more concentrated representation. It should be noted that the impulses can be perfectly localized in theory. In practice, however, the impulse may be observed with some errors when the time instant of the impulse is not coincident with the valid point in the time axis. The magnitude of the error is closely related to the resolution in the time direction of the reassigned representation and the deviation of the impulse time instant

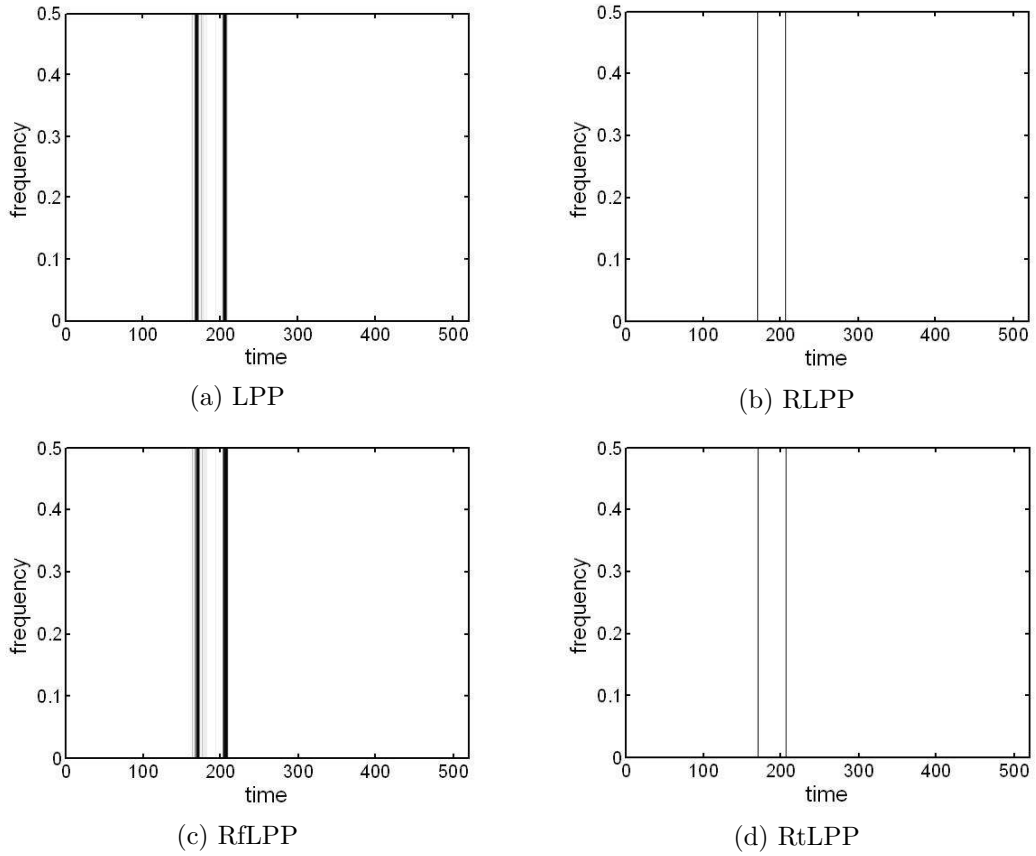

(a) LPP (b) RLPP

(c) RfLPP (d) RtLPP

Figure 6.3: Localizing impulse signals using LPP, RLPP, RfLPP and RtLPP.

away from the valid point in the time axis.

To further demonstrate the property of perfect localization, a signal with one chirp and one impulse is considered in Figure 6.4 to show that the RLPP achieves a better signal concentration than the LPP, RfLPP and RtLPP. From Figures 6.2, 6.3, and 6.4, it is concluded that, if a signal only contains chirp components, the RfLPP is preferred to achieve a better signal concentration with a reduced computation complexity. On the other hand, if a signal only contains impulse components, the RtLPP can be used instead of the RLPP. For a signal containing both chirp and impulse components, the RLPP achieves the best signal concentration performance for all components.

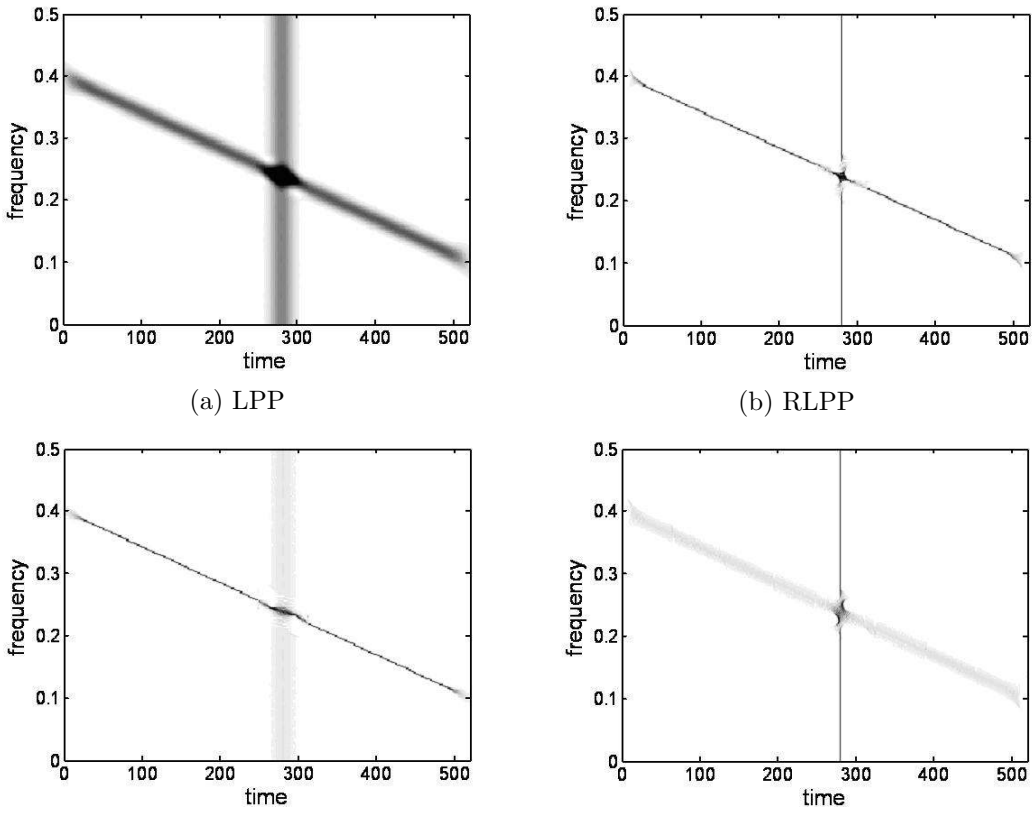

(a) LPP (b) RLPP

(c) RfLPP (d) RtLPP

Figure 6.4: Localizing a signal with chirp and impulse components using the LPP, RLPP, RfLPP and RtLPP.

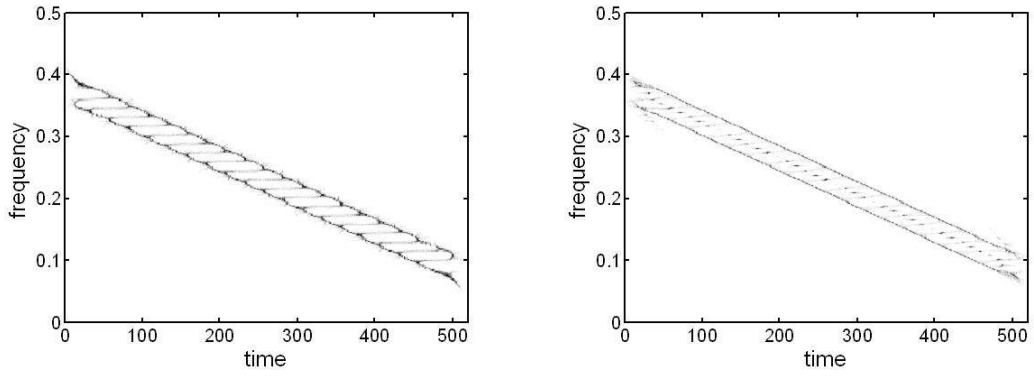

(a) RSP (b) RSPWVD

Figure 6.5: RSP and RSPWVD of a signal with two parallel chirp components.

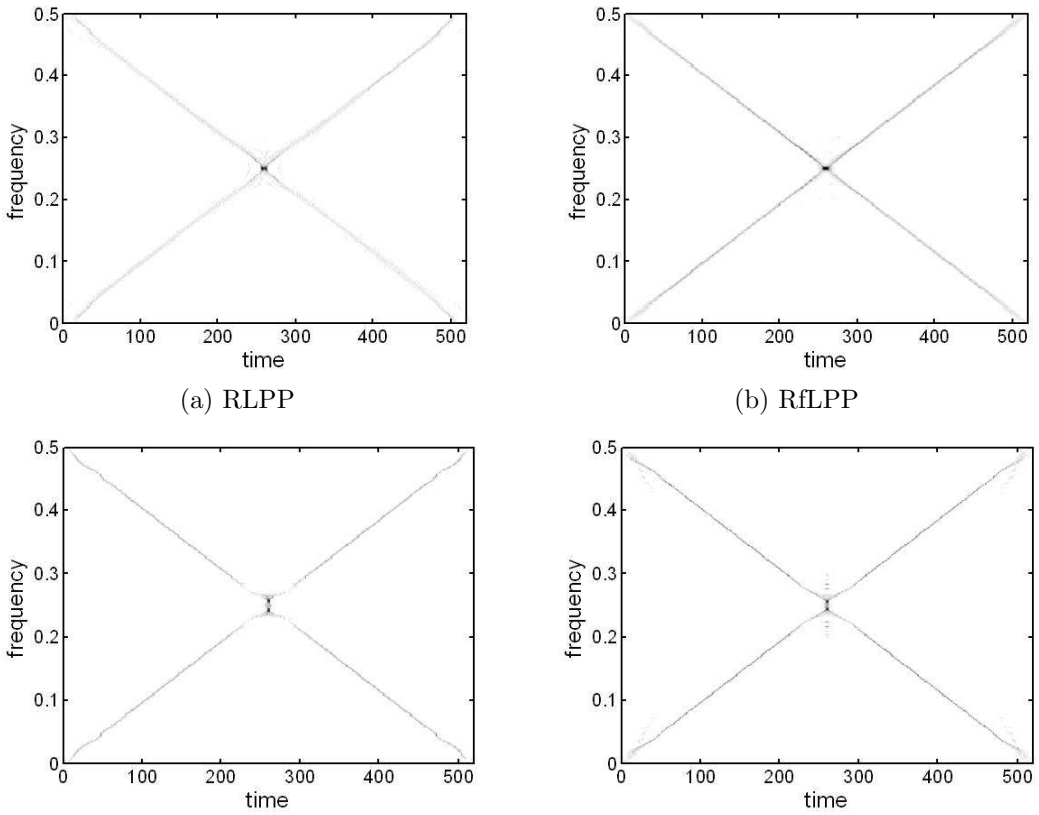

(a) RLPP (b) RfLPP

(c) RSP (d) RSPWVD

Figure 6.6: The RLPP, RfLPP, RSP and RSPWVD of a signal containing two crossed chirp components.

Figure 6.5 gives the RSP and RSPWVD of the signal used in Figure 6.1 to clearly demonstrate that the RSP cannot separate two closely located chirp components, and the RSPWVD suffers from the existence of cross term interferences. The RLPP in Figure 6.1 and the RfLPP in Figure 6.2 can achieve a much better time-frequency representation than the RSP and RSPWVD in Figure 6.5 with more concentrated signal components and without any cross terms. Furthermore, the RfLPP uses much less computation time than the RLPP because the reassignment is performed along the frequency direction only.

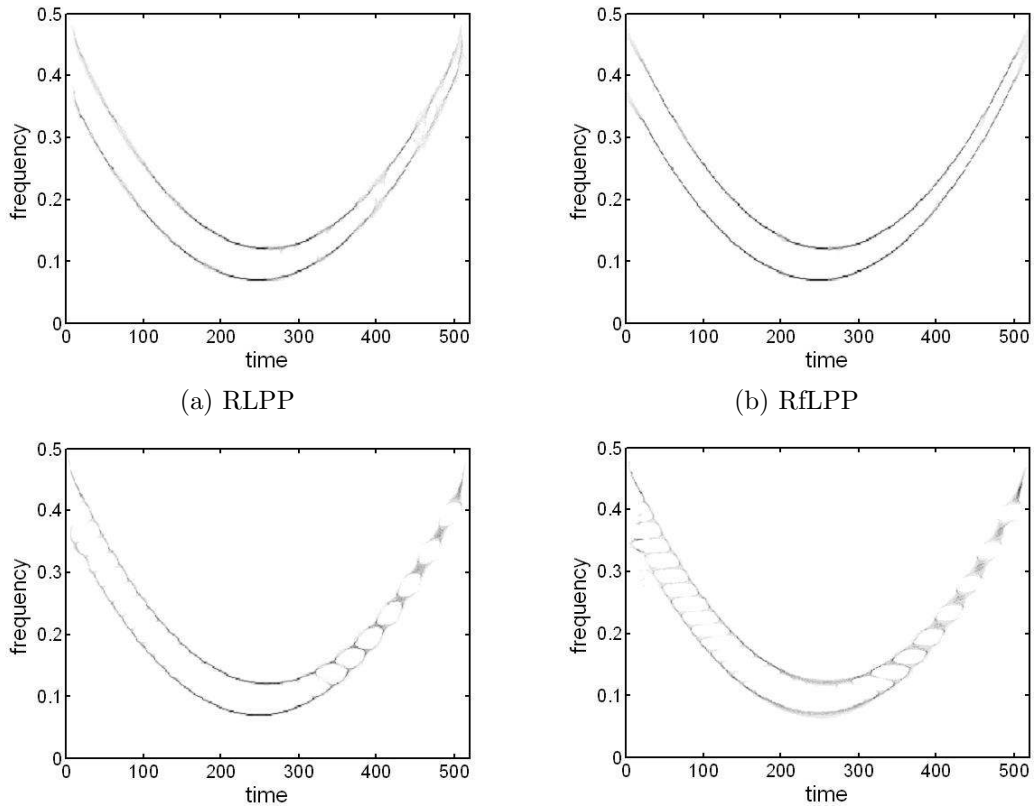

(a) RLPP (b) RfLPP

(c) RSP (d) RSPWVD

Figure 6.7: The RLPP, RfLPP, RSP and RSPWVD of a signal containing two parabolic frequency modulated components.

Next we will consider a signal

$$x(t) = e^{j2\pi(0.00048t^2)} + e^{j2\pi(-0.00048t^2+0.5t)},$$

containing two chirp components with different chirp rates. The window length used in this case is 131 points.

Figure 6.6 shows the RLPP, RfLPP, RSP and RSPWVD. It is seen that the RfLPP achieves the signal representation even better than the RLPP, which verifies the conclusion in Section 6.3 that the RfLPP is able to represent chirp components more accurately than the RLPP.

To show the efficiency of the RLPP for the higher-order time-varying signals,

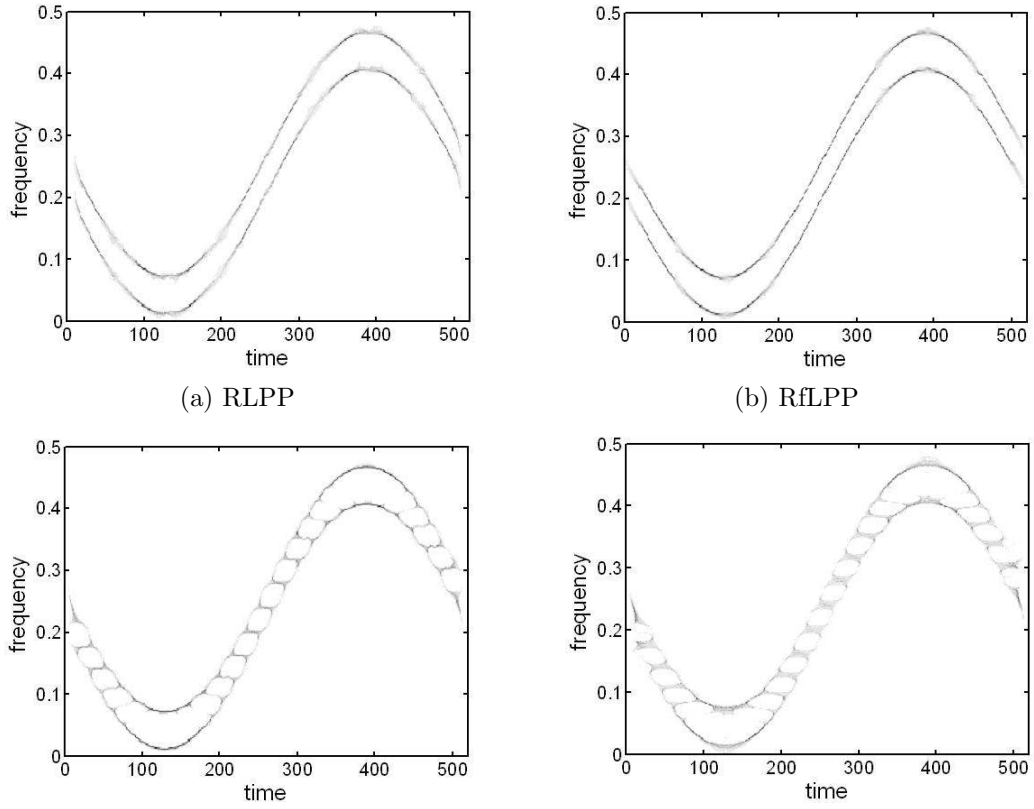

(a) RLPP (b) RfLPP

(c) RSP (d) RSPWVD

Figure 6.8: The RLPP, RfLPP, RSP and RSPWVD of a signal containing two sinusoidal frequency modulated components.

a signal with two parabolic frequency modulated components,

$$x(t) = e^{j2\pi(0.38t - 0.00125t^2 + 0.00000168t^3)} + e^{j2\pi(0.48t - 0.00135t^2 + 0.00000178t^3)},$$

is used with a window length of 65 points. Figure 6.7 shows the RLPP, RfLPP, RSP and RSPWVD. It is observed that the RSP and RSPWVD can also obtain concentrated representations, but cannot separate two closely located components. In contrast, the RLPP and RfLPP can provide much clean representations. Since the segment within each window size is assumed to be a chirp, the RfLPP can still achieve a better representation than the RLPP. Similar results can be achieved for signal with two sinusoidal frequency modulation components with a window length of 65 points, as shown in Figure 6.8.

In general a long window length used in the LPFT provides a higher frequency resolution and a lower time resolution. For the higher-order time-varying signals, the window length should be small enough so that each segment within the window can be assumed to be the chirp signal. When this condition is satisfied, it is possible to use the second-order LPFT to process higher-order time-varying signals such as the sinusoidal frequency modulation signals shown in Figure 6.8. Then, the use of the proposed reassignment method can effectively improve the concentration of the signal components.

6.4 The Reassigned Robust LPP

In practice, the signals under consideration are always embedded in noise. For signals corrupted by additive white Gaussian noise (AWGN), the required performance can be achieved with the standard methods, such as the STFT and the LPFT [48]. However, in some situations such as in the applications of communications and imaging, signals are corrupted by impulsive noise. In this case, these standard methods have difficulties in obtaining sufficient signal concentration and resolution. To minimize the effects of impulsive noise, Huber proposed the robust estimation methods to obtain the parameters of the corrupted signals [180]. The robust STFT based on median filtering [73] was also introduced recently to achieve significantly better performance in impulsive noise environments. Similarly, the robust LPFT was proposed to produce highly concentrated representations of time-varying signals in impulsive noise [74].

6.4.1 Review on the Standard and Robust Methods

The STFT form of a signal $x(t)$ is defined by the following minimization problem [180]:

$$\text{STFT}(t,\omega) = \arg\min_{m} J(t,\omega;m), \tag{6.4.1}$$

where

$$J(t,\omega,m) = \sum_{n} h(nT)F[e(t,\omega,n;m)], \tag{6.4.2}$$

$h(nT)$ is a real and even window function, $F(e)$ is a loss function and $e(t,\omega,n;m)$ is the error function given by

$$e(t,\omega,n;m) = x(t+nT)e^{-j\omega nT} - m, \tag{6.4.3}$$

where T is the sampling period and m is an estimated expectation of the sample average of $x(t+nT)\ e^{-j\omega nT}$.

Listed below are definitions of the standard STFT, LPFT and their robust variations.

A. Standard STFT and standard LPFT

The standard STFT, which is a solution to (6.4.1) with a loss function $F(e) = |e|^2$, is defined as

$$\text{STFT}(t,\omega) = \text{FT}\{x(t+nT)h(nT)\}, \tag{6.4.4}$$

where FT is the Fourier transform operator. The spectrogram is defined as $|\text{STFT}|^2$.

As a generalized form of the STFT, the LPFT of an input $x(t)$ is defined as [38]:

$$\text{LPFT}(t,\omega,\omega_1,\cdots,\omega_{M-1}) = \text{FT}[x(t+nT)h(nT)\ e^{-j\sum_{m=2}^{M}\omega_{m-1}\frac{(nT)^m}{m!}}]. \quad (6.4.5)$$

When $M = 2$, we have the second-order LPFT defined as

$$\text{LPFT}(t,\omega,\omega_1) = \text{FT}[x(t+nT)h(nT)\ e^{-j\omega_1(nT)^2/2}],$$

which is particularly suitable to deal with chirp signals. Here ω_1 can be estimated from the location coordinates of the maximum in the PTFT, defined as [39, 40]

$$\text{PTFT}(\omega,\omega_1) = \text{FT}[x(nT)\ e^{-j\omega_1(nT)^2/2}]. \quad (6.4.6)$$

The second-order LPP with $M = 2$, which is proper to process the chirp signals, is defined as $|\text{LPFT}|^2$.

B. Robust STFT and robust LPFT

With the loss function $F(e) = |e|$ or $F(e) = |\text{Re}(e)| + |\text{Im}(e)|$, the robust M-STFT [160] or the robust STFT with the median filtering [73] can be obtained. The computation of the robust M-STFT needs the iterative procedures and therefore generally requires a heavy computational load [160]. The robust STFT with the median filtering has a simpler solution because it uses a sorting procedure [73]. Therefore the robust method based on median filtering is employed in this chapter. The robust STFT is defined as [73]

$$\begin{aligned}\text{rSTFT}(t,\omega) &= \text{median}\{\text{Re}[x(t+nT)h(nT)\exp^{-j\omega nT}]\} \\ &\quad +j\text{median}\{\text{Im}[x(t+nT)h(nT)\exp^{-j\omega nT}]\}. \quad (6.4.7)\end{aligned}$$

The robust spectrogram is defined as $|\text{rSTFT}|^2$.

The robust LPFT of the input $x(t)$ is defined as [74]:

$$\begin{aligned} \text{rLPFT}(t,\omega,\omega_1) &= \text{median}\{\text{Re}[x(t+nT)h(nT)\ e^{-j\omega nT - j\omega_1 (nT)^2/2}]\} \\ &+ j\text{median}\{\text{Im}[x(t+nT)h(nT)\ e^{-j\omega nT - j\omega_1 (nT)^2/2}]\}. \end{aligned} \tag{6.4.8}$$

In this case, the robust PTFT is used to estimate ω_1 for signals corrupted by impulsive noise. The estimation performances achieved by using the PTFT and robust PTFT of the signals in impulsive noise were compared in [48]. It was shown that the peaks from the robust PTFT are more easily identified than from the PTFT. Similarly the robust LPP is defined as $|\text{rLPFT}|^2$.

In general, the standard transforms are used as the maximum likelihood estimators for signals in AWGN, and the robust methods based on median filtering produces good representations of the signals corrupted by impulsive noise [73, 74]. For signals corrupted by the mixture of AWGN and impulsive noises, however, the L-estimation-based transforms outperform the standard and the robust transforms [181].

6.4.2 Definition of the Reassigned robust SP and LPP

In this section, the reassignment method is extended to the robust spectrogram and the robust LPP to obtain a good distribution concentration for signals embedded in impulsive noise. The operators of the reassigned robust spectrogram (RrSP) are defined as:

$$\hat{t}(x;t,\omega) = t - \text{Re}\left\{\frac{\text{rSTFT}_{Th}(x;t,\omega)}{\text{rSTFT}_h(x;t,\omega)}\right\}, \tag{6.4.9}$$

$$\hat{\omega}(x;t,\omega) = \omega + \text{Im}\left\{\frac{\text{rSTFT}_{Dh}(x;t,\omega)}{\text{rSTFT}_h(x;t,\omega)}\right\}. \tag{6.4.10}$$

The reassignment operators of the reassigned robust LPP (RrLPP) are defined as:

$$\hat{t}(x;t,\omega) = t - \text{Re}\left\{\frac{\text{rLPFT}_{Th}(x;t,\omega)}{\text{rLPFT}_{h}(x;t,\omega)}\right\}, \tag{6.4.11}$$

$$\hat{\omega}(x;t,\omega) = \omega + \text{Im}\left\{\frac{\text{rLPFT}_{Dh}(x;t,\omega)}{\text{rLPFT}_{h}(x;t,\omega)}\right\}. \tag{6.4.12}$$

The reassigned robust LPP along the frequency direction (RfrLPP) is given by:

$$\text{RfrLPP}(x;t,\omega') = \int \text{rLPP}(x;t,\omega)\delta[\omega' - \hat{\omega}(x;t,\omega)]d\omega.$$

In general, the use of the robust LPFT in robust LPP is similar to the use of the robust STFT in the robust spectrogram. One additional requirement for the robust LPFT is that the parameter ω_1 in (6.4.8) has to be estimated from the robust PTFT of each signal segment.

6.5 Performance Comparisons

In this section, we compare the performances of those methods discussed in Sections 6.3 and 6.4. The comparisons are made in terms of the readability of signal components, the required computational complexity, the ratio of distribution concentration, and the mean squared errors (MSEs) of the instantaneous frequency estimation.

Let us consider a parabolic FM signal,

$$x(t) = e^{j2\pi(0.5t - 0.00173t^2 + 0.0000022t^3)}, \tag{6.5.1}$$

which is assumed to be corrupted by impulsive noise, $n(t) = \alpha[w_1^3(t) + jw_2^3(t)]$, where $\alpha = 0.5$, $w_1(t)$ and $w_2(t)$ are independent Gaussian random variables with

unit variances. The variance of the impulsive noise is $\sigma_n^2 = 30\alpha^2$ [163], leading to a signal-to-noise ratio (SNR) of -8.75dB when $\alpha = 0.5$. The probability density function of the noise is $g(x) = 1/3\sqrt{2\pi}e^{-|x|^{2/3}/2}|x|^{-2/3}$, which was used to model many real-life engineering problems [73] [74] . A Hamming window of 65 points is used in the simulations. Within the window duration, each signal segment of the signal can be approximately assumed to be a chirp.

A. Readability

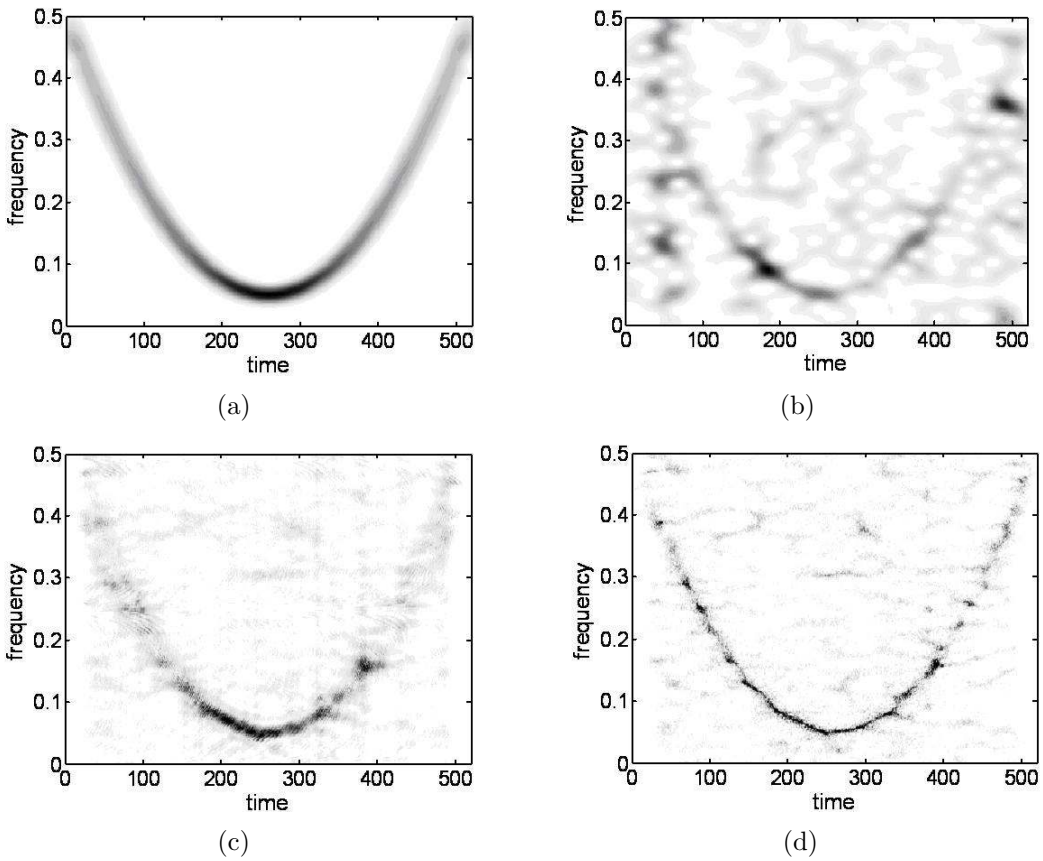

Figure 6.9: The spectrogram-related representations of the parabolic FM signal in impulsive noise; (a) spectrogram of a clean signal, (b) spectrogram of a corrupted signal, (c) robust spectrogram of a corrupted signal and (d) reassigned robust spectrogram of a corrupted signal.

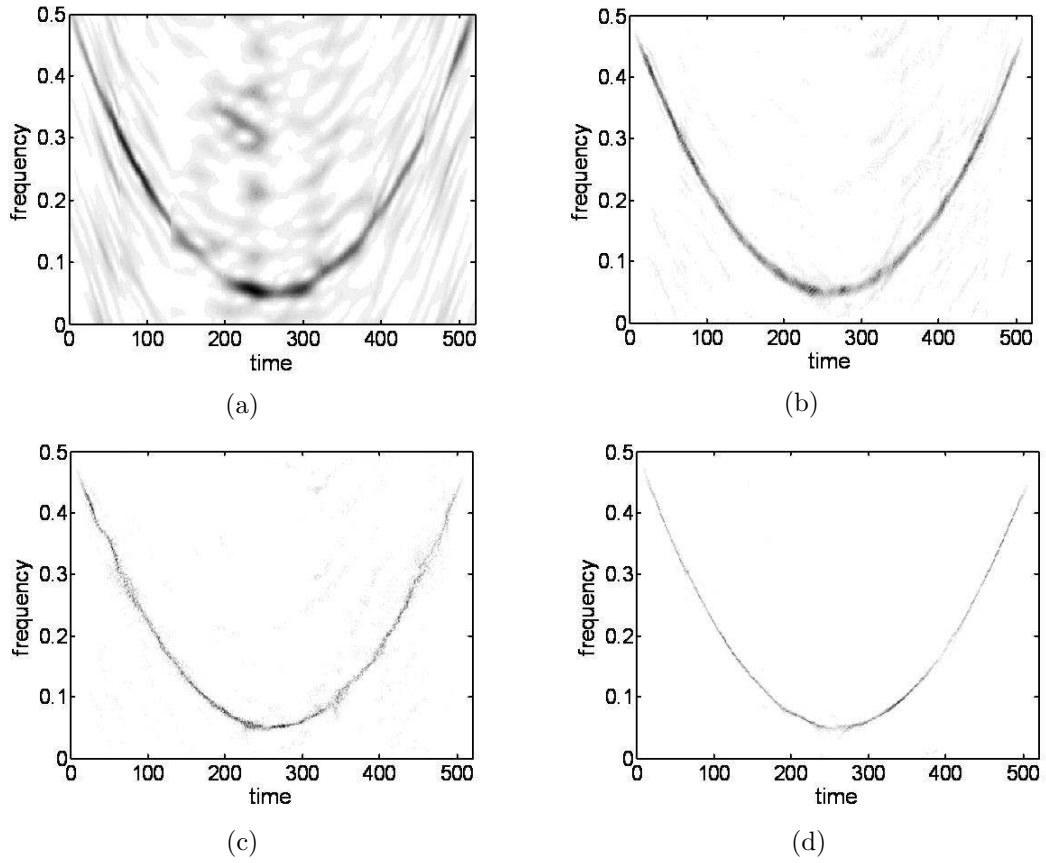

Figure 6.10: The LPP-related representations of the parabolic FM signal in impulsive noise; (a) LPP, (b) robust LPP, (c) reassigned robust LPP, and (d) reassigned robust LPP along the frequency direction.

Figure 6.9(a) shows the standard spectrogram of a clean signal $x(t)$ and Figure 6.9(b) gives the standard spectrogram of the signal corrupted by impulsive noise. The robust spectrogram of the corrupted signal is given in Figure 6.9(c) to show the improvement on signal concentration compared with that in Figure 6.9(b). Finally, Figure 6.9(d) gives the reassigned robust spectrogram of the signal in the same noise environment. Although better visual representation on the signal component is achieved by applying the reassignment and robust operations to the spectrogram, further improvements on signal concentration and resolution in the time-frequency domain are still desired for practical ap-

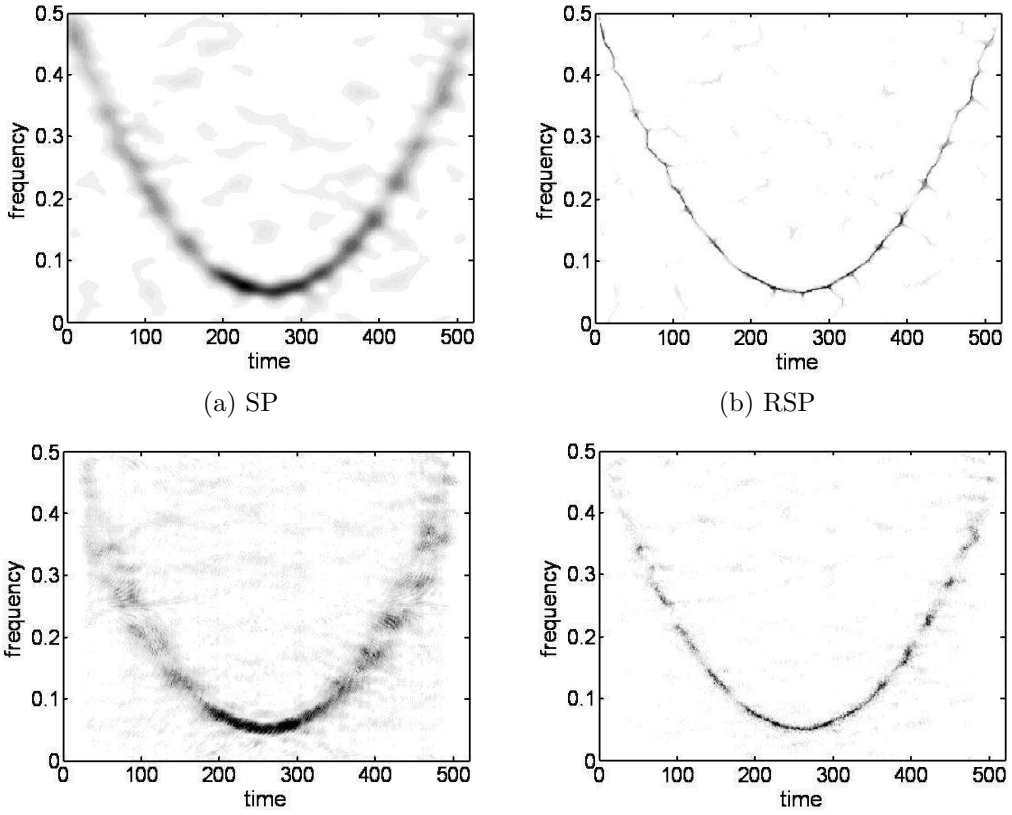

(a) SP (b) RSP

(c) Robust SP (d) RrSP

Figure 6.11: The spectrogram-related representations of the parabolic FM signal in AWGN.

plications.

We now consider the LPP-related representations for the same corrupted signal, as shown in Figure 6.10. The comparison between Figure 6.9(b) and Figure 6.10(a) shows that the latter achieves an obvious improvement on signal concentration, which is expected because the LPP uses the parameter ω_1 to more accurately describe the change of the signal frequencies. It is also observed that in Figure 6.10(b) the robust LPP achieves a substantial improvement on signal representation in the time-frequency domain. Furthermore, Figures 6.10(c) and (d) show that the reassignment operations on the robust LPP are effective to

improve the concentration in the time-frequency domain. The RfrLPP in Figure 6.10(d) appears to be more concentrated than the RrLPP in Figure 6.10(c).

Both Figure 6.9 and Figure 6.10 show that, compared with the standard methods, the robust SP and robust LPP using median filtering are effective to remove the effects of impulsive noise. Then with the reassignment operations, the concentration of the signal component can be further improved.

Figure 6.11 and Figure 6.12 show the representations based on the SP and LPP, respectively, for signal $x(t)$ embedded in AWGN $n(t) = 0.75[w_3(t) + jw_4(t)]$, where $w_3(t)$ and $w_4(t)$ are independent Gaussian random variables with unit variances. Again, it is seen that the LPP-related representations achieve better performances than their spectrogram-related counterparts. It is also observed that the RrLPP in Figure 6.12(d) achieves slightly degraded representation than the RLPP in Figure 6.12(b). It is because that although the median filtering used in robust methods is effective to reduce the effects of impulsive noise, it is not useful for minimizing the effects of AWGN. This observation is consistent with the conclusion in [74]. Meanwhile, Figure 6.11 and Figure 6.12 show that all the reassigned representations achieve improvement on signal concentration compared with their counterparts without the reassignment. In particular, both the RfLPP in Figure 6.12(e) and the RfrLPP in Figure 6.12(f) achieve sufficiently concentrated representations.

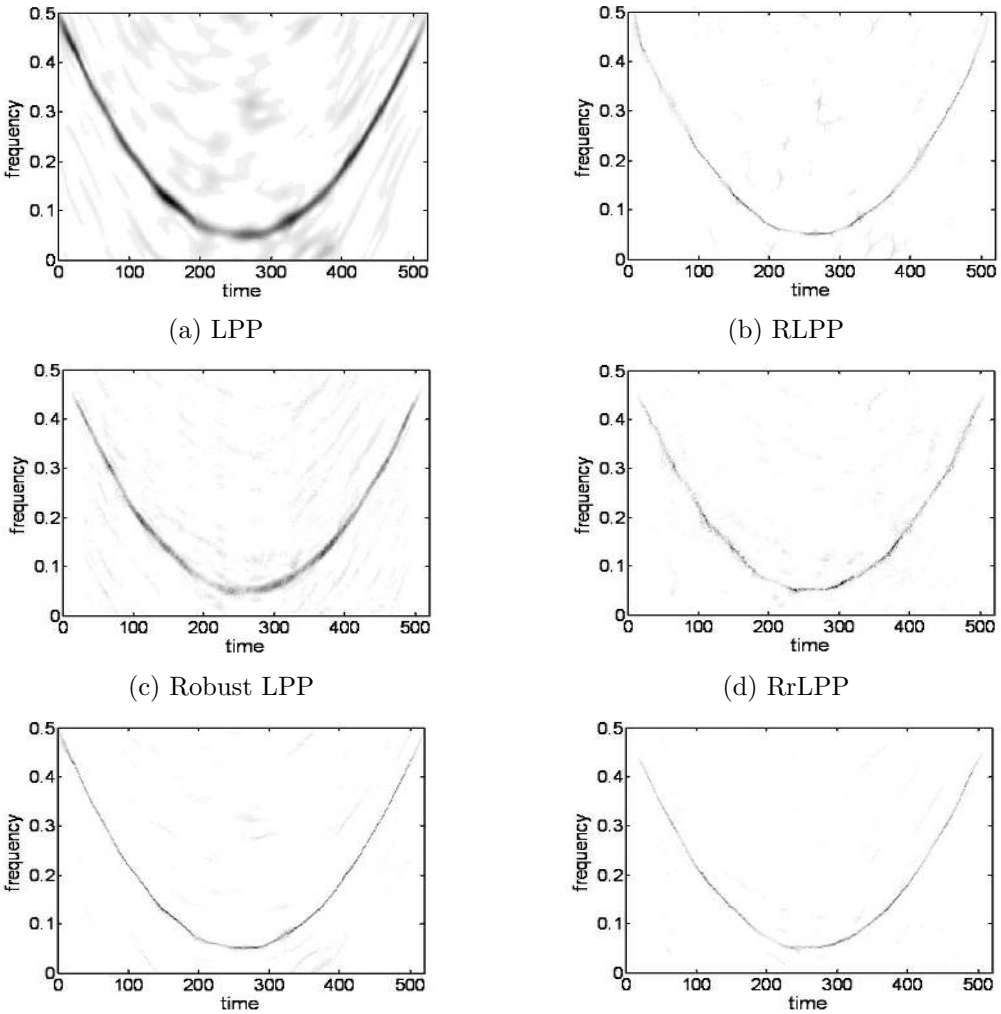

(a) LPP (b) RLPP

(c) Robust LPP (d) RrLPP

(e) RfLPP (f) RfrLPP

Figure 6.12: The LPP-related representations of the parabolic FM signal in AWGN.

B. Computational complexity

For the spectrogram-related methods that are used for Figure 6.9 and Figure 6.11, the maximum overlap between adjacent segments is necessary to achieve good signal representations. The maximum overlap is accomplished by sliding the window by one data point to obtain each succeeding signal segment. It was reported in [48] that even without any overlap between adjacent segments, a good approximation to the signal components can be achieved by the LPFT as

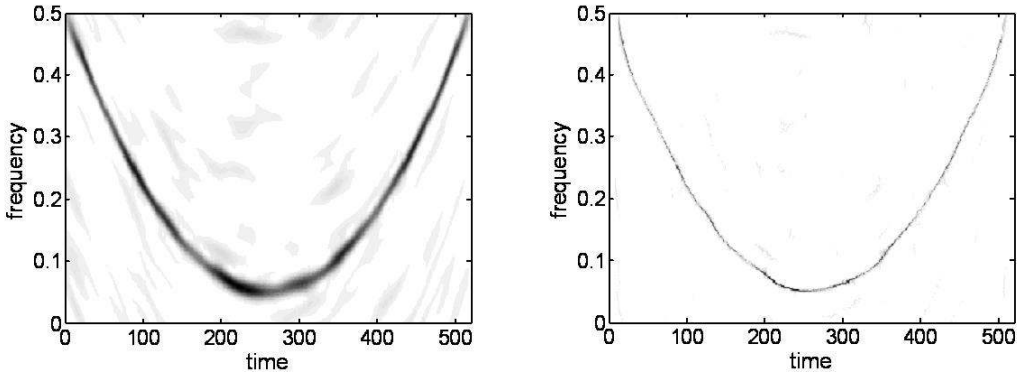

(a) LPP (b) RLPP

Figure 6.13: The LPP and RLPP of the parabolic FM signal, with the maximum overlap between signal segments.

long as the window is short enough, as demonstrated in Figure 6.10 and Figure 6.12. For the sake of comparison, Figure 6.13 gives the LPP and RLPP that are computed with the maximum overlap. Visual inspections show that the LPP and RLPP in Figure 6.13(a) and (b) are not obviously better than those without any overlap in Figure 6.12(a) and (b). However the process without any overlap greatly reduces the computational complexity, which is shown later in Table 6.1. In the LPP without overlap, each segment within the small window is assumed to be a chirp having the same parameter ω_1. When the chirp rates of the consecutive segments are sufficiently different, smearing in the time-frequency domain may occur between the segments.

A window of length M is used to segment the signal, and therefore, each segment needs an M-point Fourier transform whose computational complexity, in terms of the number of complex multiplications, is in the order of $M \log_2 M$. For the spectrogram of an N-point signal sequence, where $N >> M$ and the maximum overlap is used, the computational complexity is in the order of $NM \log_2 M$. The LPP computation for each data segment needs to estimate the

parameter ω_1 by using the PTFT, which requires a computational complexity in the order of MM_1 [44], where M and M_1, being the number of points related to ω and ω_1, respectively, are the dimensional sizes of the PTFT. According to the result reported in [39], M_1 should be larger than M to achieve a satisfactory accuracy. Since the LPP, with an estimated ω_1, is performed in the same way as the spectrogram, the total numbers of complex multiplications for the LPP of an N-point sequence are in the orders of $NM(\log_2 M + M_1)$ for the maximum overlap, and $N(M \log_2 M + M_1)$ for non-overlap between the segments, respectively.

For the reassigned methods such as the RLPP and RSP, most of the computational complexity is for the reassignment process. Therefore, the RLPP does not need much more computational complexity than the RSP. Since the computational complexity of the sorting procedure, i.e., the quick sorting algorithm [182], for the robust methods is in the order of $M \log_2 M$, the computational complexity of the robust spectrogram is in the order of $N^2 M \log_2 M$. Therefore using the robust PTFT to estimate the parameter ω_1, the computational complexity of the robust LPP without overlap is in the order of $NM(N+M_1) \log_2 M$. The main computational complexity for the RrLPP is for the sorting procedure of the median filtering. The computational complexity of the RrLPP is about three times of that needed by the robust LPP since the reassignment computation needs about three times of that for the sorting procedure compared to the robust LPP.

The computation times required by various methods for the specific signal $x(t)$ are listed in Table 6.1. The signal is corrupted by either AWGN or impulsive noise when the robust operation is applied in the processing methods.

The computations are under the Window XP operating system and the programming environment of MATLAB 7.1. The computer is Pentium 4 with a clock rate of 2.66 GHz and a RAM size of 512 MBytes. The numerical values in Table 6.1 are the average of 50 measurements of the computation times. The computation times of LPP and RLPP with the maximum overlap are 38.86 and 41.57 seconds, respectively, compared with 0.81 and 3.74 seconds for those without any overlap. Therefore, the computational complexity is significantly reduced, i.e., achieving about 47 and 10 times of savings in computation time. In Table 6.1, the computation times for the LPP-related representations are measured on the processing without any overlap between the signal segments, while the computation times for the spectrogram-related representations in Table 6.1 are measured on the processing with the maximum overlap to achieve the best possible performance.

Table 6.1: Comparison on computation time required by various computation methods. The AWGN is $0.75[w_3(t) + jw_4(t)]$ and the impulsive noise is $0.5[w_1^3(t) + jw_2^3(t)]$.

Methods	Computation time (s)
spectrogram	0.1641
reassigned spectrogram	3.8730
robust spectrogram	122.9487
reassigned robust spectrogram	370.3964
LPP	0.8087
reassigned LPP	3.7418
reassigned LPP along the frequency direction	2.9340
robust LPP	123.7826
reassigned robust LPP	364.0574
reassigned robust LPP along the frequency direction	252.0833

In Table 6.1, the computation time needed by the LPP is about 5 times of

that needed by the SP. However, it is observed that the robust methods with median filtering, i.e., robust SP and robust LPP, or the reassignment methods, i.e., RSP and RLPP, require about the same computation time. It means that as far as the median filtering or reassignment method is involved, the improvements made by the LPPs do not require extra computation time compared with the spectrograms with median filtering or reassignment method. Furthermore, it is also noted that compared to the RLPP and RrLPP, the RfLPP and RfrLPP can reduce the computation times by about 20% and 30%, respectively. It will be shown in the following subsections that the RfLPP and RfrLPP can provide better distribution concentrations and smaller MSEs. Therefore by using these two methods we can achieve significant performance improvements with savings in computation time.

C. Distribution concentration

Next we will evaluate the performances in terms of the distribution concentration with the signal $x(t)$ embedded in impulsive noise $n(t) = \alpha[w_1(t)^3 + jw_2(t)^3]$, AWGN $n(t) = w_3(t) + jw_4(t)$, and mixture of these noises $n(t) = \alpha[w_1(t)^3 + jw_2(t)^3] + [w_3(t) + jw_4(t)]$, where $\alpha \in [0, 1.5]$. For each value of SNR or α, measurements of 100 trials are averaged. Similar to the concept of the distribution concentration used in [72], we define the distribution concentration as

$$\begin{aligned} \mathbf{B} &= 10\log_{10}\frac{E_1}{E_2}, \\ &= 10\log_{10}\frac{\text{average}(\text{TFT}(t,\omega)_{(t,\omega)\in R})}{\text{average}(\text{TFT}(t,\omega)_{(t,\omega)\notin R})} \end{aligned} \tag{6.5.2}$$

where region R corresponds to the instantaneous frequency lines of the signal components, which are determined by the peak values in the TFTs, E_1 is the

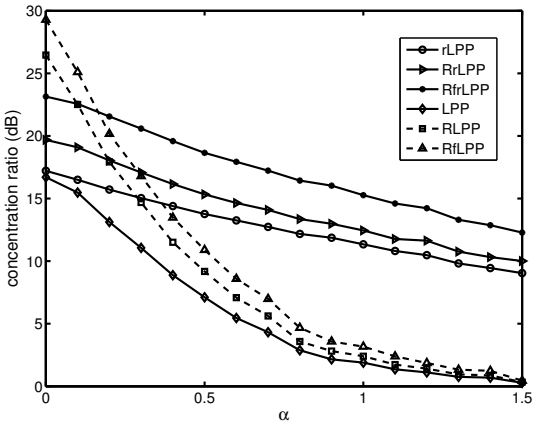

(a) Concentration ratios in impulsive noise

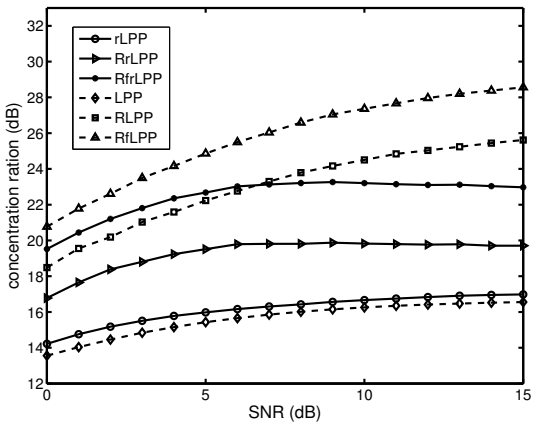

(b) Concentration ratios in AWGN

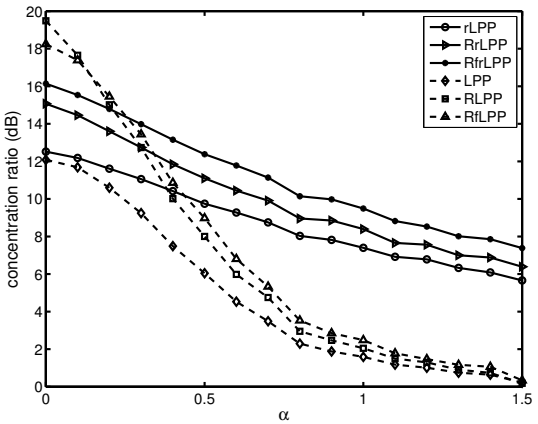

(c) Concentration ratios in mixture noise

Figure 6.14: Distribution concentration ratios of various LPP-related representations for the parabolic FM signal in impulsive noise, AWGN, and mixed noise.

average energy along the instantaneous frequency region R, E_2 is the average energy outside the instantaneous frequency region R.

For the signal in (6.5.1) corrupted by impulsive noise, Figure 6.14(a) shows that the robust LPP-related methods with the median filtering are able to improve the distribution concentration. However, the median filtering is not effective to improve the concentration of the signals corrupted by AWGN, as shown in Figure 6.14(b). In contrast, the reassigned LPP-related methods are effective to improve the concentration for signals in AWGN or impulsive noise. It also confirms that both the median filtering and reassignment operation are necessary to achieve the best distribution concentration for signals in the mixed noise environment, as shown in Figure 6.14(c). It is also noted that, the RfrLPP in Figure 6.14(a) and the RfLPP in Figure 6.14(b) obtain better concentrations, which are consistent with the observations from Figure 6.10 and Figure 6.12, respectively.

D. Mean Squared Errors (MSEs)

We will compare the MSEs of instantaneous frequency estimation achieved by using various LPP-related methods for the signal $S(t)$ embedded in different noise environments. The instantaneous frequency estimation is obtained according to the curve peak positions in the time-frequency transforms, defined as [60]

$$\hat{\omega}(t) = \arg\max_{\omega} \mathrm{TFT}(t, \omega).$$

The MSE of the estimator is defined as

$$\int [\omega(t) - \hat{\omega}(t)]^2 dt,$$

where $\omega(t)$ is the true instantaneous frequency and $\hat{\omega}(t)$ is the estimated instan-

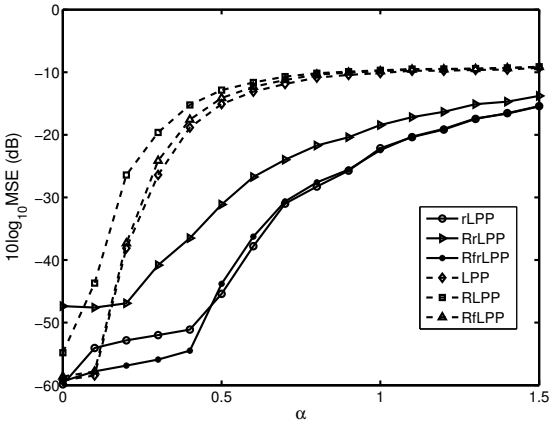

(a) MSE in impulsive noise

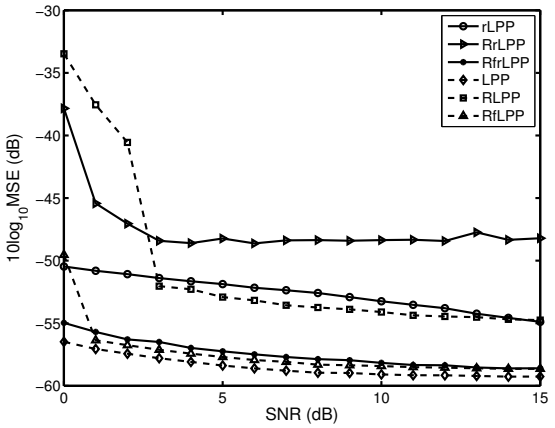

(b) MSE in Gauss noise

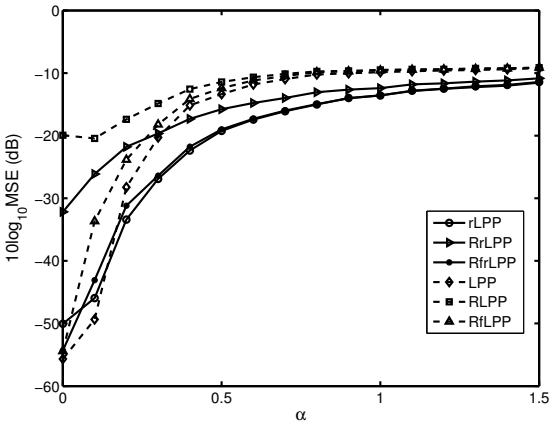

(c) MSE in mixed noise

Figure 6.15: MSEs of instantaneous frequency estimation achieved by using various LPP-related methods for the parabolic FM signal in impulsive noise, AWGN, and mixed noise.

taneous frequency.

In general, median filtering is useful for minimizing the MSEs when the signal is in impulsive noise environment, as seen in Figure 6.15(a) in which larger MSEs are obtained by the LPPs without using median filtering. However, the median filtering has side effects on minimizing the MSEs for signals in Gaussian noise environments, which can be seen from Figure 6.15(b) that the representations with median filtering achieve larger MSEs than their counterparts. Meanwhile the reassignment operations also have adverse effects on minimizing the MSEs for signals in AWGN or impulsive noise. This can be seen obviously from, for example, Figure 6.15(a) and Figure 6.15(b) that the RrLPP and RLPP achieve much larger MSEs than the robust LPP and LPP, respectively. However, it is interesting to see that in Figure 6.15(a), the RfrLPP has almost the same MSEs as the robust LPP, and in Figure 6.15(b), the RfLPP has almost the same MSEs as the LPP. It means that the RfLPP and the RfrLPP have little side effects on minimizing the MSEs in AWGN and impulsive noise, respectively.

It should be noted that in this simulation, the testing signal with a parabolic frequency modulation law is given as an example. Similar results can be achieved with other kind of frequency modulation law such as the LFM signals and the sinusoidal FM signals.

It is also worth mentioning that in this chapter the impulsive noise is modelled as $\alpha[w_1^3 + jw_2^3]$. For impulsive noise belonging to Middleton class A model [183], or the standard Cauchy distributed complex noise $v_1(n) + jv_2(n)$ [184], where $v_1(n)$ and $v_2(n)$ are mutually independent with the standard Cauchy distribution $f_v(x) = \dfrac{1}{\pi(1+x^2)}$, similar performance comparisons can also be achieved.

6.6 Conclusion

This chapter defines the reassignment method based on the second-order LPP to improve the signal concentration performance for signals with time-varying frequencies. Properties of the RLPP are studied and theoretically proved. Simulation results are also presented to verify some properties of the RLPP, RtLPP and RfLPP. The improvements on signal concentration show that these proposed reassigned methods are better analysis tools than the RSP and RSPWVD for the chirp signals, as well as for higher-order signals with time-varying frequencies. The reassignment method is also extended to the robust LPP, therefore achieving the RrLPP, to provide concentrated performance for signals corrupted by the impulsive noise.

Moreover, performances achieved by various LPP-related methods are compared in different noise environments such as AWGN, impulsive noise, and the mixture of AWGN and impulsive noises. Based on the simulated results, it is observed that with the reassignment, the LPP-related methods can improve the concentration in both noise environments, although the reassignment may not be useful to minimize the MSEs of the instantaneous frequency estimation. While the median filtering in the robust LPP-related methods is useful to minimize the MSEs for signal in impulsive noise, it has side effects for signals in AWGN. Therefore for LPP-related methods, robust operation with median filtering, reassignment operation, or both of them, should be adequately selected for signals in a given noise environment to achieve the performance objectives. Furthermore, the RfLPP and the RfrLPP are better choices for signals in AWGN and impulsive noise, respectively, because they can achieve good distribution concentrations and small mean square errors with reduced computational com-

plexities. The information revealed from the comparisons is particularly useful for selecting a suitable combination of the processing techniques to achieve the desired performance objective.

6.7 Appendix

6.7.1 Expressions of the Reassignment Operators for RLPP

We will first prove an equality:

$$\begin{aligned}&\mathrm{LPFT}_g(x;t,\omega)\ \mathrm{LPFT}_h^*(x;t,\omega) \qquad (6.7.1)\\ &= \int\int \mathrm{WVD}\left(h\cdot g;u,-\frac{\omega_1}{2}u+\Omega\right)\ \mathrm{WVD}\left(x;t-u,\omega-\frac{\omega_1}{2}u-\Omega\right)dud\Omega.\end{aligned}$$

where the subscripts g and h indicate the real and even window functions that are used by the associated LPFTs. This equation will be used to prove the time and frequency operators for the RLPP.

Proof: The right-hand side of (6.7.1) is expanded into:

$$\begin{aligned}&\int\int\int\int h\left(u+\frac{\tau}{2}\right)g^*\left(u-\frac{\tau}{2}\right)e^{-j\left(-\frac{\omega_1}{2}u+\Omega\right)\tau}d\tau\\ &\quad\cdot x\left(t-u+\frac{\alpha}{2}\right)x^*\left(t-u-\frac{\alpha}{2}\right)\ e^{-j\left(\omega-\frac{\omega_1}{2}u-\Omega\right)\alpha}d\alpha dud\Omega\\ &=\int\int h\left(u+\frac{\tau}{2}\right)g^*\left(u-\frac{\tau}{2}\right)x\left(t-u+\frac{\tau}{2}\right)\\ &\quad\cdot x^*\left(t-u-\frac{\tau}{2}\right)e^{j\omega_1u\tau}e^{-j\omega\tau}d\tau du. \qquad (6.7.2)\end{aligned}$$

Let $a=u+\frac{\tau}{2}$ and $b=u-\frac{\tau}{2}$, then $u=\frac{a+b}{2}$ and $\tau=a-b$. With $d\tau du=|J|dadb$, where the Jacobian determinant is

$$J=\begin{vmatrix}\frac{\partial u}{\partial a} & \frac{\partial u}{\partial b}\\ \frac{\partial \tau}{\partial a} & \frac{\partial \tau}{\partial b}\end{vmatrix}=-1,$$

(6.7.2) becomes

$$\begin{aligned}&\int\int h(a)g^*(b)x(t-b)x^*(t-a)e^{j\omega_1\frac{a^2-b^2}{2}}\ e^{-j\omega(a-b)}dadb\\&=\mathrm{LPFT}_g(x;t,\omega)\ \mathrm{LPFT}_h^*(x;t,\omega).\end{aligned}$$

Based on (6.7.1), (6.3.2) and (6.3.3) can be proved as follows. We first consider the time operator given in (6.3.2).

Proof: Since

$$\begin{aligned}&\mathrm{Re}\left\{\mathrm{WVD}\left(h\cdot Th;u,-\frac{\omega_1}{2}u+\Omega\right)\right\}\\&=\mathrm{Re}\left\{\int h\left(u+\frac{\tau}{2}\right)\left(u-\frac{\tau}{2}\right)h^*\left(u-\frac{\tau}{2}\right)\ e^{-j\left(-\frac{\omega_1}{2}u+\Omega\right)\tau}d\tau\right\}\\&=\mathrm{Re}\left\{u\mathrm{WVD}\left(h;u,-\frac{\omega_1}{2}u+\Omega\right)\right.\\&\quad\left.-\int\frac{\tau}{2}h\left(u+\frac{\tau}{2}\right)h^*\left(u-\frac{\tau}{2}\right)e^{-j\left(-\frac{\omega_1}{2}u+\Omega\right)\tau}d\tau\right\}\\&=u\mathrm{WVD}\left(h;u,-\frac{\omega_1}{2}u+\Omega\right).\end{aligned}$$

Thus

$$\begin{aligned}&\mathrm{Re}\left\{\mathrm{LPFT}_{Th}(x;t,\omega)\ \mathrm{LPFT}_h^*(x;t,\omega)\right\}\qquad(6.7.3)\\&=\mathrm{Re}\left\{\int\int\mathrm{WVD}\left(h\cdot Th;u,-\frac{\omega_1}{2}u+\Omega\right)\right.\\&\qquad\left.\cdot\,\mathrm{WVD}\left(x;t-u,\omega-\frac{\omega_1}{2}u-\Omega\right)dud\Omega\right\}\\&=\int\int u\mathrm{WVD}\left(h;u,-\frac{\omega_1}{2}u+\Omega\right)\mathrm{WVD}\left(x;t-u,\omega-\frac{\omega_1}{2}u-\Omega\right)dud\Omega,\end{aligned}$$

where Th indicates a time ramped window $t\cdot h(t)$ and the subscripts, for example, Th and h mean the types of the windows used in the LPFTs.

Next let us prove the frequency operator given in (6.3.3).

Proof: Since

$$\begin{aligned}
&\mathrm{Im}\left\{\mathrm{WVD}\left(h\cdot Dh;u,-\frac{\omega_1}{2}u+\Omega\right)\right\}\\
&=\mathrm{Im}\left\{\int H\left(-\frac{\omega_1}{2}u+\Omega+\frac{\xi}{2}\right)\left[-j\left(-\frac{\omega_1}{2}u+\Omega-\frac{\xi}{2}\right)\right]\right.\\
&\quad\left.\cdot H^*\left(-\frac{\omega_1}{2}u+\Omega-\frac{\xi}{2}\right)e^{j\xi u}d\xi\right\}\\
&=\mathrm{Im}\left\{-j\left(-\frac{\omega_1}{2}u+\Omega\right)\mathrm{WVD}\left(h;u,-\frac{\omega_1}{2}u+\Omega\right)+\right.\\
&\quad\left.\int j\frac{\xi}{2}H\left(-\frac{\omega_1}{2}u+\Omega+\frac{\xi}{2}\right)H^*\left(-\frac{\omega_1}{2}u+\Omega-\frac{\xi}{2}\right)\ e^{j\xi u}d\xi\ \right\}\\
&=-(\Omega-\frac{\omega_1}{2}u)\mathrm{WVD}\left(h;u,-\frac{\omega_1}{2}u+\Omega\right).
\end{aligned}$$

Thus

$$\begin{aligned}
&\mathrm{Im}\left\{\mathrm{LPFT}_{Dh}(x;t,\omega)\mathrm{LPFT}_h^*(x;t,\omega)\right\}\\
&=\mathrm{Im}\left\{\int\int\mathrm{WVD}\left(h\cdot Dh;u,-\frac{\omega_1}{2}u+\Omega\right)\right.\\
&\quad\left.\cdot\,\mathrm{WVD}\left(x;t-u,\omega-\frac{\omega_1}{2}u-\Omega\right)dud\Omega\right\}\\
&=-\int\int\left(\Omega-\frac{\omega_1}{2}u\right)\mathrm{WVD}\left(h;u,-\frac{\omega_1}{2}u+\Omega\right)\\
&\quad\cdot\mathrm{WVD}\left(x;t-u,\omega-\frac{\omega_1}{2}u-\Omega\right)dud\Omega,
\end{aligned}\tag{6.7.4}$$

where Dh means a window which is the first derivative of $h(t)$, and LPFT_{Dh} is the LPFT using the window of Dh.

6.7.2 Properties of the RLPP

Some properties of the RLPP presented in Section 6.3 are proved as follows.

(a). Time and frequency shift invariance

Let us consider $y(t) = x(t-t_0)\exp^{j\omega_0 t}$. From the time and frequency shift properties of the WVD [34], it is known that

$$\mathrm{WVD}(y;t,\omega) = \mathrm{WVD}(x;t-t_0,\omega-\omega_0).$$

From (6.3.2), we achieve

$$\begin{aligned}
&\hat{t}(y;t,\omega) \\
&= t - \qquad (6.7.5)\\
&\frac{\int\int u\,\mathrm{WVD}\left(h;u,-\frac{\omega_1}{2}u+\Omega\right)\mathrm{WVD}\left(x;t-t_0-u,\omega-\omega_0-\frac{\omega_1}{2}u-\Omega\right)dud\Omega}{\int\int \mathrm{WVD}\left(h;u,-\frac{\omega_1}{2}u+\Omega\right)\mathrm{WVD}\left(x;t-t_0-u,\omega-\omega_0-\frac{\omega_1}{2}u-\Omega\right)dud\Omega} \\
&= \hat{t}(x;t-t_0,\omega-\omega_0)+t_0. \qquad (6.7.6)
\end{aligned}$$

Similarly from (6.3.3) and following the similar procedure, we have

$$\hat{\omega}(y;t,\omega) = \hat{\omega}(x;t-t_0,\omega-\omega_0)+\omega_0,$$

so that

$$\mathrm{RLPP}(y;t',\omega') = \mathrm{RLPP}(x;t'-t_0,\omega'-\omega_0).$$

(b) Energy conservation

$$\begin{aligned}
&\int\int \mathrm{RLPP}\,(x;t',\omega')\,dt'd\omega' \\
&= \int\int\int\int \mathrm{WVD}\left(h;u,-\frac{\omega_1}{2}u+\Omega\right)\int x\left(t-u+\frac{\tau}{2}\right)x^*\left(t-u-\frac{\tau}{2}\right) \\
&\quad\cdot\exp^{-j\left(\omega-\frac{\omega_1}{2}u-\Omega\right)\tau}\,d\tau dud\Omega dtd\omega \\
&= \int\int \mathrm{WVD}\left(h;u,-\frac{\omega_1}{2}u+\Omega\right)\int x(t-u)x^*(t-u)dud\Omega dt.
\end{aligned}$$

If $\int\int \mathrm{WVD}\left(h; u, -\frac{\omega_1}{2}u + \Omega\right) dud\Omega = 1$, the above equation becomes $\int |x(t)|^2 dt$.

(c) Perfectly localizing chirp and impulse signals

For a chirp signal $x(t) = Ae^{j(\omega_0 t + \alpha t^2/2)}$, we have

$$\mathrm{WVD}(x; t, \omega) = A^2 \delta(\omega - \omega_0 - \alpha t),$$

therefore

$$\hat{\omega}(x; t, \omega) = \omega - \frac{\int\int \left\{ \begin{array}{l} \left(\Omega - \frac{\omega_1}{2}u\right) \ \mathrm{WVD}\left(h; u, -\frac{\omega_1}{2}u + \Omega\right) \\ \cdot A^2 \delta\left(\omega - \frac{\omega_1}{2}u - \Omega - \omega_0 - \alpha(t-u)\right) \end{array} \right\} dud\Omega}{\int\int \left\{ \begin{array}{l} \mathrm{WVD}\left(h; u, -\frac{\omega_1}{2}u + \Omega\right) \\ \cdot A^2 \delta\left(\omega - \frac{\omega_1}{2}u - \Omega - \omega_0 - \alpha(t-u)\right) \end{array} \right\} dud\Omega}.$$

Since $\Omega = \omega - \frac{\omega_1}{2}u - \omega_0 - \alpha(t-u)$,

$$\hat{\omega}(x; t, \omega) = \omega_0 + \alpha t + (\omega_1 - \alpha) \frac{\int u \ \mathrm{WVD}\left(h; u, \omega - \omega_1 u - \omega_0 - \alpha(t-u)\right) du}{\int \mathrm{WVD}\left(h; u, \omega - \omega_1 u - \omega_0 - \alpha(t-u)\right) du}.$$

When the parameter ω_1 is estimated exactly, we have $\omega_1 = \alpha$, and thus

$$\hat{\omega}(x; t, \omega) = \omega_0 + \alpha t,$$

which is exactly the IF of the chirp signal. Thus

$$\mathrm{RLPP}(x; t', \omega') = \int\int \mathrm{LPP}(x; t, \omega) \delta(t' - \hat{t}(x; t, \omega)) \delta(\omega' - \omega_0 - \alpha t) dt d\omega.$$

For the impulse signal $x(t) = A\delta(t - t_0)$, we have

$$\mathrm{WVD}(x; t, \omega) = A^2 \delta(t - t_0).$$

Thus

$$\begin{aligned}\hat{t}(x;t,\omega) &= t - \frac{\int\int u\ \mathrm{WVD}\left(h;u,-\frac{\omega_1}{2}u+\Omega\right)A^2\delta(t-u-t_0)dud\Omega}{\int\int \mathrm{WVD}\left(h;u,-\frac{\omega_1}{2}u+\Omega\right)A^2\delta(t-u-t_0)dud\Omega}\\ &= t_0,\end{aligned}$$

and

$$\mathrm{RLPP}(x;t',\omega') = \delta(t'-t_0)\int\int \mathrm{LPP}(x;t,\omega)\delta(\omega'-\hat{\omega}(x;t,\omega))dtd\omega.$$

Chapter 7

Conclusion and Future work

In this chapter, we conclude the studies presented in this thesis and propose some suggestions for the future work.

7.1 Conclusions

Chapter 3 presents the uncertainty principle of the LPFT. It shows that the uncertainty product of the LPFT of an arbitrary order is related to the parameters of the signal and the window function, as well as the errors of estimating the polynomial coefficients. Important factors, such as the window width, the length of overlap between signal segments, order mismatch and estimation errors of polynomial coefficients, are also discussed in terms of the uncertainty principles. The effects of minimizing computational complexities by reducing the order of the transform and the overlap length between signal segments are also examined. In terms of the signal concentration, comparisons among the FT, the STFT, the WVD and the second-order LPFT are presented. Simula-

tions for speech signal and bat sound are also given to show that the LPFT is an excellent candidate providing better representations for signals having time varying frequencies.

Chapter 4 is dedicated to the quantitative SNR analysis for the LPFT. To better judge the possibility of detecting the narrowband signals in the frequency domain and the time-varying signal in the time-frequency domain, the definition of the 3dB SNR as in communications is employed. This 3dB SNR definition is transform-domain dependent and directly relates to the bandwidth of the signal. Therefore it is suitable for signals in the time-frequency domain as well as in the time and frequency domains, respectively. Based on the relationship between the LPFT and the WVD, theoretical analysis on the 3dB SNR of the LPFT is carried out. The quantitative 3dB SNR analysis of the pseudo WVD (PWVD) in continuous-time form is presented as well. Comparisons on the 3dB SNR performances achieved by using the LPFT, the FT, the STFT and the WVD are presented with simulations to illustrate the advantage of using the LPFT.

In Chapter 5, application examples in ISAR imaging and LFM signal detection are presented to verify the advantage of the LPFT. In ISAR imaging applications, simulations on radar imaging using the LPFT, STFT and FT are presented to show the performance improvements achieved by using the LPFT. Measures are also taken to minimize the required computational complexity by reducing the overlap length between adjacent segments of input data. For LFM signal detection, the LPFT is employed to achieve significant increase of noise margins in the signal parameter domain, which leads to a new method based on the combination of the local polynomial periodogram (LPP) and the Hough

transform. Simulation results for the detection of mono- and multi-component LFM signals corrupted by additive white Gaussian noise and impulsive noise show that the proposed method achieves significant performance improvement on detecting the LFM signals in very low SNR environments. It is also found that by using the time-frequency filtering, the computational complexity of the detection can be substantially reduced.

In Chapter 6, the reassignment method is extended to the second-order local polynomial periodogram (LPP) to get the reassigned LPP (RLPP). The RLPP is defined and its interesting properties are investigated with mathematical proofs. Based on simulation results with various signals, comparisons with the reassigned spectrogram and smoothed pseudo WVD are made to show the desirable ability of the RLPP for improvement on the signal concentration in the time-frequency domain. Furthermore, the reassignment method is combined with the robust methods, such as the robust spectrogram and the robust LPP, to process signals in impulsive noise. Performance using various LPP-related methods are compared for signals embedded in additive white Gaussian noise, impulsive noise, and the mixture of additive white Gaussian noise and impulsive noises. Compared with the counterparts without reassignments, the reassigned methods can help to improve the distribution concentration. However, it is not capable of minimizing the mean squared errors of instantaneous frequency estimation. Furthermore, the reassigned LPP along the frequency direction (RfLPP) and the reassigned robust LPP along the frequency direction (RfrLPP) are preferred because they can achieve good distribution concentrations and small mean square errors with reduced computational complexities.

7.2 Recommendations for Further Research

Based on the studies in this thesis, the following recommendations are made for possible research directions in the future.

7.2.1 Properties of PTFT

More details on properties of the PTFT are needed to be analyzed. For example, sidelobes of the PTFT, which are the peaks other than the peaks corresponding to desired signal components, are to be further explored. Since the PTFT includes the multi-dimensional calculation, the properties of its sidelobes are more complicated than those of one-dimensional DFT.

7.2.2 Uncertainty Principles of the LPFTs

In this thesis, the uncertainty product is obtained by multiplying the duration and bandwidth of the local signal, which places limits on the processing techniques of the windowed transforms. Other kinds of uncertainty principles, such as the global uncertainty principle, are discussed in [59]. It will be interesting to investigate these kinds of uncertainty principles for the LPFTs.

Furthermore, it will be interesting to explore how the uncertainty principle can be used in signal design such as for optimization of the distribution.

7.2.3 LPP-Hough Transform

Statistical performances of the Wigner-Hough transform (WHT), pseudo Wigner-Hough transform (PWHT) and Radon-ambiguity function have been given in

the literature. It will be desirable to give the statistical analysis for the LPP-Hough transform (LHT) to evaluate this new transform and compare it with other transforms.

The Hough transform has been generalized to detect and estimate the nonlinear FM signals embedded in additive white Gaussian noise [185], where the reassigned smoothed pseudo WVD is employed because of its good localization and interference suppression properties. Therefore, another possible extension of the LHT is for the detection of nonlinear FM signals, with the help of the generalized Hough transform [150].

In this thesis, the time-frequency filtering, which is performed in the time-frequency domain through masking, is subject to the prerequisite that estimation of the instantaneous frequency can be achieved. Therefore it becomes unsuitable when the SNR is too low. An alternative filtering method such as the time-frequency peak filtering (TFPF) [186] can be employed under this situation. The TFPF encodes the noisy signal as the instantaneous frequency of an FM analytic signal, and then the instantaneous frequency estimation is performed on the analytic signal using the peak of a TFR to recover the filtered signal. It has been shown in [186] that the TFPF can work with better performance in very noisy environments where the time-frequency filtering fails to work.

7.2.4 Applications of the LPFT for Signals with Time-varying Frequencies

Applications of the LPFT in radar imaging and LFM signal detection, as well as speech and bat sound analysis, have been presented in this thesis. More applications using the LPFT are preferred. Since the LPFT is a generalized form of the STFT, in the areas in which the STFT is used, there exists the potential for generalization and improvement by using the LPFT. For instance, to analyze the patterns of time-frequency structures within a musical passage, the STFT is usually employed due to its simplicity. Despite of its low resolution the STFT has been widely used to process the music signals [29, 30, 187], the musical instruments [31], the music of bird song [66], and the musical rhythm [188]. It is obvious that better results can be obtained by using TFRs which can provide higher resolution with reduced or free cross terms, and the LPFT is an appropriate choice.

Furthermore, the synthesis algorithm for the LPFT is also desired, which is important for other potential applications such as audio and speech synthesis.

7.2.5 Applications of the Reassigned LPP

Applications of the reassigned LPP is highly appreciated, based on its property of perfectly localizing the LFM signals. For example, in communications, the adaptive wavelet transform [189], the adaptive STFT [28] and the WVD [190] have been used for the excision of the second-order polynomial phase interference (PPI). All these transforms, except the WVD, do not have optimal concentration property for the second-order PPI, which is the linear chirp inter-

ference. However, the undesirable influence of cross terms prevents the WVD from being used for the multi-component interference excision. Therefore the RLPP can be the proper candidate to achieve better results in this case.

Moreover, it would be interesting to know whether perfect localization can be achieved for higher-order PPSs by choosing a corresponding higher-order polynomial in the reassigned LPP.

Author's Publications

1 Xiumei Li and Guoan Bi, "The Reassigned Local Polynomial Periodogram and Its Properties," *Signal Process.*, vol. 89, no. 2, pp. 206-217, 2009.

2 Xiumei Li, Guoan Bi, and Yingtuo Ju, "Quantitative SNR Analysis for ISAR Imaging Using Local Polynomial Fourier Transform," *IEEE Trans. Aerosp. Electron. Syst.*, vol. 45, no. 3, pp. 1241-1248, 2009.

3 Guoan Bi, Yingtuo Ju, and Xiumei Li, "Fast Algorithms for Polynomial Time-Frequency Transforms of Real-Valued Sequences," *IEEE Trans. Signal Process.*, vol. 56, no. 5, pp. 1905-1915, 2008.

4 Xiumei Li and Guoan Bi, "Local Polynomial Fourier Transform: A Review and Analysis," *Submitted to Signal Process.*, 2010.

5 Guoan Bi and Xiumei Li, "Detection of LFM Signals with LPP-Hough Transform," *Submitted to Signal Process.*, 2010.

6 Xiumei Li and Guoan Bi, "On Uncertainty Principle of the Local Polynomial Fourier Transform," *to be Submitted to Digital Signal Processing*, 2010.

7 Xiumei Li, Guoan Bi, and Yingtuo Ju, "Improved ISAR Imaging Based on Local Polynomial Fourier Transform," *Proceedings of the Sixth International Conference on Information, Communications and Signal Processing (ICICS)*, Dec. 2007.

8 Xiumei Li and Guoan Bi, "A New Reassigned Time-frequency Representation," *Proceedings of the Sixteenth European Signal Processing Conference (EUSIPCO)*, Aug. 2008.

9 Xiumei Li and Guoan Bi, "A New Transform for Chirp Detection," *Proceedings of the 2008 International Symposium on Information Theory and its Applications (ISITA)*, Dec. 2008.

10 Xiumei Li and Guoan Bi, "Uncertainty Principle of the Second-Order LPFT," *IEEE International Symposium on Circuits and Systems (ISCAS)*, May 2009.

11 Xiumei Li and Guoan Bi, "Reassignment Methods for Robust Time-frequency Representations," *Proceedings of the Seventh International Conference on Information, Communications and Signal Processing (ICICS)*, Dec. 2009.

Bibliography

[1] P. Davis, *Interpolation and Approximation*. NY: Dover, 1975.

[2] J. Xu, L. Durand, and P. Pibarot, "Extraction of the aortic and pulmonary components of the second heart sound using a nonlinear transient chirp signal model," *IEEE Trans. Biomed. Eng.*, vol. 48, no. 3, pp. 277–283, 2001.

[3] H. Hassanpour, W. Williams, M. Mesbah, and B. Boashash, "Time-frequency extraction of EEG spike events for seizure detection in neonate," in *International Symposium on Sigal Processing and its Applications (ISSPA)*, 2001, pp. 246–249.

[4] B. Boarshash and M. Mesbah, "A time-frequency approach for newborn seizure detection," *IEEE Eng. Med. Biol. Mag.*, vol. 20, no. 5, pp. 54–64, 2001.

[5] H. Permuter and J. Francos, "A parametric approach for estimating the orientation of planar surfaces," in *Proc. of International Conference on Image Processing (ICIP)*, 1998, pp. 181–185.

[6] S. Stanković, I. Djurović, and I. Pitas, "Watermarking in the Space/Spatial-Frequency domain using two-dimensional Radon-Wigner distribution," *IEEE Trans. Image Process.*, vol. 10, no. 4, pp. 650–658, 2001.

[7] S. Erküçük, S. Krishnan, and M. Zeytinoğlu, "A robust audio watermark representation based on linear chirps," *IEEE Trans. Multimedia*, vol. 8, no. 5, pp. 925–936, 2006.

[8] A. Ramalingam and S. Krishnan, "Robust image watermarking using a chirp detection-based technique," *IEE Proc. Vis. Image Signal Process.*, vol. 152, no. 6, pp. 771–778, 2005.

[9] I. Djurović and S. Stanković, "Estimation of time-varying velocities of moving objects by time-frequency representations," *IEEE Trans. Image Process.*, vol. 12, no. 5, pp. 550–562, 2003.

[10] S. Stanković, I. Djurović, and R. Herpers, "Velocity and acceleration estimation in video sequences by the local polynomial periodogram," in *International Symposium on Signal Processing and its Applications (ISSPA)*, vol. 1, 2003, pp. 145–148.

[11] S. Sandberg, K. Marco, and M. Tzannes, "Some alternatives in transform-domain suppression of narrow-band interference for signal detection and demodulation," *IEEE Trans. Commun.*, vol. 43, no. 12, pp. 3025–3036, 1995.

[12] S. Barbarossa and A. Scaglione, "Adaptive time-varying cancellation of wideband interferences in spread-spectrum communications based on time-frequency distributions," *IEEE Trans. Signal Process.*, vol. 47, no. 4, pp. 957–965, 1999.

[13] C. Wang and M. Amin, "Performance analysis of instantaneous frequency based interference excision techniques in spread spectrum communications," *IEEE Trans. Signal Process.*, vol. 46, no. 1, pp. 70–82, 1998.

[14] A. Orazco-Lugo, M. Lara, D. Mclernon, and H. Muro-Lemus, "Multiple packet reception in wireless ad hoc networks using polynomial phase modulating sequences," *IEEE Trans. Signal Process.*, vol. 50, no. 5, pp. 1077–1090, 2002.

[15] A. Papandreou-Suppappola and S. Suppappola, "Wideband weyl symbols for dispersive time-varying processing of systems and random signals," *IEEE Trans. Signal Process.*, vol. 51, no. 8, pp. 2093–2110, 2003.

[16] M. Martone, "A multicarrier system based on the fractional Fourier transform for time-frequency selective channel," *IEEE Trans. Signal Process.*, vol. 49, no. 6, pp. 1011–1020, 2001.

[17] H. Liu, "Multicode ultra-wideband scheme using chirp waveforms," *IEEE J. Sel. Areas Commun.*, vol. 24, no. 4, pp. 885–891, 2006.

[18] B. Boashash, "Estimating and interpreting the instantaneous frequency of a signal−Part 2: Algorithms and applications," *Proc. IEEE*, vol. 80, no. 4, pp. 540–568, 1992.

[19] D. Wehner, *High-Resolution Radar, Second Edition*. Norwood, MA: Artech House, 1994.

[20] M. Soumekh, "Reconnaissance with ultra wideband UHF synthetic aperture radar," *IEEE Signal Process. Mag.*, vol. 12, no. 4, pp. 21–40, 1995.

[21] S. Barbarossa, A. Scaglione, and G. Giaanakis, "Product high-order ambiguity function for multicomponent polynomial-phase signal modeling," *IEEE Trans. Signal Process.*, vol. 46, no. 3, pp. 691–708, 1998.

[22] W. Au, *The Sonar of Dolphins*. Berlin, Germany: Springer-Verlag, 1993.

[23] S. Peleg and B. Porat, "Estimation and classification of polynomial-phase signals," *IEEE Trans. Inf. Theory*, vol. 37, no. 2, pp. 422–430, 1991.

[24] M. Skolnik, *Radar Handbook*. NY: McGraw-Hill, 1970.

[25] V. Chen and S. Qian, "Joint time-frequency transform for radar Range-Doppler imaging," *IEEE Trans. Aerosp. Electron. Syst.*, vol. 34, no. 2, pp. 486–499, 1998.

[26] K. Kin, I. Choi, and H. Kim, "Efficient radar target classification using adaptive joint time-frequency processing," *IEEE Trans. Antennas Propag.*, vol. 48, no. 12, pp. 1789–1801, 2000.

[27] M. Amin and G. Mandapati, "Nonstationary interference excision in spread spectrum commnications using projection filtering methods," in *The 32nd Asilomar Conf. on Signals, Systems and Comput.*, 1998, pp. 827–831.

[28] X. Ouyang and M. Amin, "Short-time Fourier transform receiver for nonstationary interference excision in direct sequence spread spectrum communications," *IEEE Trans. Signal Process.*, vol. 49, no. 4, pp. 851–863, 2001.

[29] G. Don and J. Walker, "Music: A time-frequency approach," [Online] Available at: http://www.uwec.edu/walkerjs/media/TFAM.pdf.

[30] M. Dorfler, "Time-frequency analysis for music signals: A mathematical approach," *Journal of New Music Research*, vol. 30, no. 1, pp. 3–12, 2001.

[31] J. Alm and J. Walker, "Time-frequency analysis of musical instruments," *SIAM Review*, vol. 44, no. 3, pp. 457–476, 2002.

[32] R. Mcaulay and T. Quatieri, "Pitch estimation and voicing detection based on a sinusoidal speech modal," in *IEEE Int. Conf. Acoust., Speech, and Signal Process. (ICASSP)*, 1990, pp. 249–252.

[33] K. Sekihara, S. Nagarajan, and Y. Miyashita, "Time-Frequency MEG-MUSIC algorithm," *IEEE Trans. Med. Imag.*, vol. 18, no. 1, pp. 92–97, 1999.

[34] L. Cohen, *Time-Frequency Analysis*. NJ: Prentice-Hall, 1995.

[35] F. Hlawatsch and G. F. Boudreaux-Bartels, "Linear and quadratic time-frequency signal representations," *IEEE Trans. Magn.*, vol. 9, no. 4, pp. 21–67, 1992.

[36] E. Sejdić, I. Djurović, and J. Jiang, "Time-frequency feature representation using energy concentration: An overview of recent advanccs," *Digital Signal Process.*, vol. 19, no. 1, pp. 153–183, 2009.

[37] P. Rao and F. Taylor, "Estimation of instantaneous frequency using the discrete Wigner distribution," *Electr. Lett.*, vol. 26, no. 4, pp. 246–248, 1998.

[38] V. Katkovnik, "A new form of Fourier transform for time-varying frequency estimation," *Signal Process.*, vol. 47, no. 2, pp. 187–200, 1995.

[39] M. Ikram, K. Abed-Meraim, and Y. Hua, "Fast qudratic phase transform for estimating the parameters of multicomponent chirp signals," *Digital Signal Process.*, vol. 7, no. 2, pp. 127–135, 1997.

[40] X. Xia, "Discrete chirp-Fourier transform and its applications to chirp rate estimation," *IEEE Trans. Signal Process.*, vol. 48, no. 11, pp. 3122–3133, 2000.

[41] G. Bi and Y. Wei, "Fast computation for third-order polynomial time frequency transforms," *Electr. Lett.*, vol. 40, no. 5, pp. 349–351, 2004.

[42] Y. Wei and G. Bi, "Fast algorithm for polynomial time frequency transform," *Signal Process.*, vol. 87, no. 5, pp. 789–798, 2007.

[43] G. Bi and Y. Wei, "Split-radix algorithms for arbitrary order of polynomial time frequency transforms," *IEEE Trans. Signal Process.*, vol. 55, no. 1, pp. 134–141, 2007.

[44] G. Bi, Y. Wei, G. Li, and C. Wang, "Radix-2 DIF fast algorithms for polynomial time-frequency transforms," *IEEE Trans. Aerosp. Electron. Syst.*, vol. 42, no. 4, pp. 1540–1546, 2006.

[45] G. Bi and Y. Ju, "Radix-3 fast algorithms for polynomial time frequency transforms," *Signal Process.*, vol. 88, no. 9, pp. 2316–2322, 2008.

[46] Y. Ju and G. Bi, "Generalized fast algorithms for the polynomial time-frequency transforms," *IEEE Trans. Signal Process.*, vol. 55, no. 10, pp. 4907–4915, 2007.

[47] G. Bi, Y. Ju, and X. Li, "Generalized fast algorithms for the polynomial time-frequency transforms of real-valued sequences," *IEEE Trans. Signal Process.*, vol. 56, no. 5, pp. 1905–1915, 2008.

[48] Y. Wei and G. Bi, "Efficient analysis of time-varying muliticomponent signals with modified LPTFT," *EURASIP Journal on Applied Signal Processing*, vol. 2005, no. 1, pp. 1261–1268, 2005.

[49] V. Katkovnik, "Discrete-time local polynomail approximation of the instantaneous frequency," *IEEE Trans. Signal Process.*, vol. 46, no. 10, pp. 2626–2637, 1998.

[50] I. Djurović, T. Thayaparan, and L. Stanković, "Adaptive local polynomial Fourier transform in ISAR," *EURASIP Journal on Applied Signal Processing*, vol. 2006, pp. 1–15, 2006.

[51] ——, "SAR imaging of moving targets using polynomial Fourier transform," *IET Signal Process.*, vol. 2, no. 3, pp. 237–246, 2008.

[52] L. Stanković and S. Djukanović, "Order adaptive local polynomial FT based interference rejection in spread spectrum communication systems," *IEEE Trans. Instrum. Meas.*, vol. 54, no. 6, pp. 2156–2162, 2005.

[53] S. Djukanović, M. Daković, and L. Stanković, "Local polynomial Fourier transform receiver for nonstationary interference excision in DSSS communications," *IEEE Trans. Signal Process.*, vol. 56, no. 4, pp. 1627–1636, 2008.

[54] D. Gabor, "Theory of communication," *Journal of the Institution of Electrical Engineers*, vol. 93, no. 26, pp. 429–457, 1946.

[55] P. Korn, "Some uncertainty principles for time-frequency transforms of the Cohen class," *IEEE Trans. Signal Process.*, vol. 53, no. 2, pp. 523–527, 2005.

[56] P. Loughlin and L. Cohen, "The uncertainty principle: global, local, or both?" *IEEE Trans. Signal Process.*, vol. 52, no. 5, pp. 1218–1227, 2004.

[57] S. Shinde and V. Gadre, "An uncertainty principle for real signals in the fractional Fourier transform domain," *IEEE Trans. Signal Process.*, vol. 49, no. 11, pp. 2545–2548, 2001.

[58] K. Sharma and S. Joshi, "Uncertainty principle for real signals in the linear canonical transform domain," *IEEE Trans. Signal Process.*, vol. 56, no. 7, pp. 2677–2683, 2008.

[59] L. Cohen, "The uncertainty principles of the short-time Fourier transform," *Proc. SPIE*, vol. 2563, pp. 80–90, 1995.

[60] S. Qian and D. Chen, *Joint Time-Frequency Analysis: methods and applications*. NJ: Prentice-Hall, 1996.

[61] X. Xia, "A quantitative analysis of SNR in the short-time Fourier transform domain for multicomponent signals," *IEEE Trans. Signal Process.*, vol. 46, no. 1, pp. 200–203, 1998.

[62] X. Xia and V. Chen, "A quantitative SNR analysis for the pseudo Wigner-Ville distribution," *IEEE Trans. Signal Process.*, vol. 47, no. 10, pp. 2891–2894, 1999.

[63] V. Chen and H. Ling, *Time-Frequency Transform for Radar Imaging and Signal Analysis*. Boston, MA: Artech House, 2002.

[64] H. Kim and H. Ling, "Wavelet analysis of radar echo from finite-size targets," *IEEE Trans. Antennas Propag.*, vol. 41, no. 2, pp. 200–207, 1993.

[65] B. Boashash and M. Mesbah, *Applications in Time-Frequency Signal Processing*. Florida: CRC Press, 2002, ch. 9 Time-Frequency Methodology for Newborn Electroencephalographic Seizure Detection, pp. 339–369.

[66] D. Tothenberg, *Why Birds Sing: A Journey into the Mystery of Bird Song*. NY: Basic Books, 2005.

[67] S. Barbarossa, "Analysis of multicomponent LFM signals by a combined Wigner-Hough transfrom," *IEEE Trans. Signal Process.*, vol. 43, no. 6, pp. 1511–1515, 1995.

[68] M. Wang, A. Chan, and C. Chui, "Linear frequency modulated signal detecting using Radon-ambiguity transform," *IEEE Trans. Signal Process.*, vol. 46, no. 3, pp. 571–586, 1998.

[69] Y. Sun and P. Willett, "Hough transform for long chirp detection," *IEEE Trans. Aerosp. Electron. Syst.*, vol. 38, no. 2, pp. 553–569, 2002.

[70] F. Auger and P. Flandrin, "Improving the readability of time-frequency and time-scale representations by the reassignment method," *IEEE Trans. Signal Process.*, vol. 43, no. 5, pp. 1068–1089, 1995.

[71] O. Rioul and P. Flandrin, "Time-scale energy distributions: a general class extending wavelet transforms," *IEEE Trans. Signal Process.*, vol. 40, no. 7, pp. 1746–1757, 1992.

[72] I. Djurović and L. Stanković, "Time-frequency representation based on the reassigned S-method," *Signal Process.*, vol. 77, no. 1, pp. 115–120, 1999.

[73] I. Djurović, V. Katkovnik, and L. Stanković, "Median filter based realization of the robust time-frequency distributions," *Signal Process.*, vol. 81, no. 7, pp. 1771–1776, 2001.

[74] I. Djurović, "Robust adaptive local polynomial fourier transform," *IEEE Signal Process. Lett.*, vol. 11, no. 2, pp. 201–204, 2004.

[75] M. Ikram, A. Belouchrani, D. Gesbert, and K. Abed-Meraim, "Parametric estimation and suppression of non-stationary interference in DS-spread spectrum communications," in *The 32nd Asilomar Conf. on Signals, Systems and Comput.*, 1998, pp. 1401–1405.

[76] B. Boashash and B. Ristic, "Polynomial time-frequency distributions and time-varying higher-order spectra: Application to the analysis of multicomponent FM signal and to the treatment of multiplicative noise," *Signal Process.*, vol. 67, no. 1, pp. 539–569, 1998.

[77] B. Barkat and B. Boashash, "Instantaneous frequency estimation of polynomial FM signals using the peak of the PWVD: Statistical performance in the presence of additive Gaussian noise," *IEEE Trans. Signal Process.*, vol. 47, no. 9, pp. 2480–2490, 1999.

[78] S. Peleg and B. Porat, "The Cramer-Rao lower bound for signals with constant amplitude and polynomial phase," *IEEE Trans. Signal Process.*, vol. 39, no. 3, pp. 749–752, 1991.

[79] S. Peleg and B. Friedlander, "Multicomponent signal analysis using the polynomial-phase transform," *IEEE Trans. Aerosp. Electron. Syst.*, vol. 32, no. 1, pp. 378–387, 1996.

[80] R. Kennedy, *Fading dispersive communication channels.* NY: Wiley, 1960.

[81] B. Boashash, "Estimating and interpreting the instantaneous frequency of a signal—Part 1: Fundamentals," *Proc. IEEE*, vol. 80, no. 4, pp. 529–538, 1992.

[82] H. Taub and D. Schilling, *Principles of Communication Systems.* NY: McGraw-Hill, 1986.

[83] K. Clarke and D. Hess, *Communication Circuits: Analysis and Design.* Reading, MA: Addison-Wesley, 1971.

[84] S. Haykin, *Adaptive Filter Theory.* NJ: Prentice Hall, 1971.

[85] S. Peleg and B. Porat, "Linear FM signal parameter estimation from discrete-time observations," *IEEE Trans. Aerosp. Electron. Syst.*, vol. 27, no. 4, pp. 607–616, 1991.

[86] S. Peleg and B. Friedlander, "The discrete polynomial-phase transform," *IEEE Trans. Signal Process.*, vol. 43, no. 8, pp. 1901–1914, 1995.

[87] S. Barbarossa and V. Petrone, "Analysis of polynomial-phase signals by the integrated generalized ambiguity function," *IEEE Trans. Signal Process.*, vol. 45, no. 2, pp. 316–327, 1997.

[88] A. Scaglione and S. Barbarossa, "Statistical analysis of the product high-order ambiguity function," *IEEE Trans. Inf. Theory*, vol. 45, no. 1, pp. 343–356, 1999.

[89] T. Abatzoglou, "Fast maximnurm likelihood joint estimation of frequency and frequency rate," *IEEE Trans. Aerosp. Electron. Syst.*, vol. AES-22, no. 6, pp. 708–715, 1986.

[90] O. Besson, M. Ghogho, and A. Swami, "Parameter estimation for random amplitude chirp signals," *IEEE Trans. Signal Process.*, vol. 47, no. 12, pp. 3208–3219, 1999.

[91] M. Ikram and G. Zhou, "Estimation of multicomponent polynomial phase signals of mixed orders," *Signal Process.*, vol. 81, no. 11, pp. 2293–2308, 2001.

[92] P. O'Shea, "A new technique for instantaneous frequency rate estimation," *IEEE Signal Process. Lett.*, vol. 9, no. 8, pp. 251–252, 2002.

[93] ——, "A fast algorithm for estimating the parameters of a quadratic FM signal," *IEEE Trans. Signal Process.*, vol. 52, no. 2, pp. 385–393, 2004.

[94] P. Wang and J. Yang, "Multicomponent chirp signals analysis using product cubic phase funciton," *Digital Signal Process.*, vol. 16, no. 6, pp. 654–669, 2006.

[95] P. O'Shea and R. Wiltshire, "A new class of multilinear functions for polynomial phase signal analysis," *IEEE Trans. Signal Process.*, vol. 57, no. 6, pp. 2096–2109, 2009.

[96] S. Peleg, B. Porat, and B. Friedlander, "The achievable accuracy in estimating the instantaneous phase and frequency of a constant amplitude signal," *IEEE Trans. Signal Process.*, vol. 41, no. 6, pp. 2216–2224, 1993.

[97] P. O'shea, "Fast parameter estimation algorithms for linear FM signals," in *IEEE Int. Conf. Acoust., Speech, and Signal Process. (ICASSP)*, vol. 4, 1994, pp. 17–20.

[98] Y. Wei, "New algorithms for the analysis of signals with time-varying instantaneous frequency," Ph.D. dissertation, Electrical & Electronic Engineering, Nanyang Technological University, 2005.

[99] G. Bi and Y. Chen, "Fast DFT algorithms for length $N = q \times 2^m$," *IEEE Trans. Circuits Syst. II: Analog Digit. Signal Process.*, vol. 45, no. 6, pp. 685–690, 1998.

[100] [Online] Available at: http://dsp.rice.edu/software/bat-echolocation-chirp.

[101] M. Riley, *Speech time-frequency representatioans.* Boston: Kluwer Academic Publishers, 1989.

[102] L. Debnath, *Wavelets and Signal Processing.* Switzerland: Birkhäuser, 2003.

[103] B. Boashash and V. Sucic, "Resolution measure criteria for the objective assessment of the performance of quadratic time-frequency distributions," *IEEE Trans. Signal Process.*, vol. 51, no. 5, pp. 1253–1263, 2003.

[104] S. Chikkerur, A. Cartwright, and V. Govindaraju, "Fingerprint enhancement using STFT analysis," *Pattern Recognition*, vol. 40, no. 1, pp. 198–211, 2007.

[105] J. Bello, L. Daudet, S. Abdallah, C. Duxbury, M. Davies, and M. B. Sandler, "A tutorial on onset detection in music signals," *IEEE Trans. Speech and Audio Process.*, vol. 13, no. 5, pp. 1035–1047, 2005.

[106] D. Jones and R. Baraniuk, "A simple scheme for adapting time-frequency representations," *IEEE Trans. Signal Process.*, vol. 42, no. 12, pp. 3530–3535, 1994.

[107] M. Amin and K. Feng, "Short-time Fourier transforms using cascade filter structures," *IEEE Trans. Signal Process.*, vol. 42, no. 3, pp. 631–641, 1995.

[108] H. Kwok and D. Jones, "Improved instantaneous frequency estimation using an adaptive short-time Fourier transfrom," *IEEE Trans. Signal Process.*, vol. 48, no. 10, pp. 2964–2972, 2000.

[109] Y. Wei and G. Bi, "Robust STFT with adaptive window length and rotation direction," in *Proc. of Fourth International Conference on Information, Communications and Signal Processing (ICICS)*, vol. 2, 2003, pp. 827 – 829.

[110] W. Williams, "Reduced Interference Distribution: Biological applications and interpretations," *Proc. IEEE*, vol. 84, no. 9, pp. 1264–1280, 1996.

[111] Y. Wu and D. C. Munson, "Wide-angle ISAR passive imaging using smoothed pseudo Wigner-Ville distribution," in *Proc. of the Radar Conference*, 2001, pp. 363–368.

[112] S. Stanković and L. Stanković, "An architecture for the realization of a system for time-frequency signal analysis," *IEEE Trans. Circuits Syst. II: Analog Digit. Signal Process.*, vol. 44, no. 7, pp. 600–604, 1997.

[113] B. Boashash and P. O'shea, "Polynomial Wigner-Ville distributions and their relationship to time-varying higher order spectra," *IEEE Trans. Signal Process.*, vol. 42, no. 1, pp. 216–220, 1994.

[114] B. Barkat and L. Stanković, "Analysis of polynomial FM signals corrupted by heavy-tailed noise," *IEEE Trans. Signal Process.*, vol. 84, no. 1, pp. 69–75, 2004.

[115] B. Barkat and B. Boashash, "Design of higher order polynomial Wigner-Ville distributions," *IEEE Trans. Signal Process.*, vol. 47, no. 9, pp. 2608–2611, 1999.

[116] D. Reid, A. Zoubir, and B. Boashash, "Aircraft flight parameter estimation based on passive acoustic techniques using the polynomial Wigner-Ville distribution," *J. Acoust. Soc. Am.*, vol. 102, pp. 207–223, 1997.

[117] M. Daković, T. Thayaparan, S. Djukanović, and L. Stanković, "Time-frequency-based non-stationary interference suppression for noise radar systems," *IET Radar Sonar Navig.*, vol. 2, no. 4, pp. 306–314, 2008.

[118] V. Katkovnic and A. Gershman, "A local polynomial approximation based beamforming for source localization and tracking in nonstationary environments," *IEEE Signal Process. Lett.*, vol. 7, no. 1, pp. 3–5, 2000.

[119] L. Stanković, "Local polynomial Wigner distribution," *Signal Process.*, vol. 59, no. 1, pp. 123–128, 1997.

[120] C. Hory, C. Mellet, J. Valiere, and C. Depollier, "Local polynomial time-frequency transform formulation of the pseudo L-Wigner distribution," *Signal Process.*, vol. 81, no. 1, pp. 233–237, 2001.

[121] H. Ozaktas, Z. Zalevsky, and M. Kutay, *The Fractional Fourier Transform with Applications in Optics and Signal Processing.* NY: John Wiley & Sons Ltd, 2000.

[122] F. Zhang, Y. Chen, and G. Bi, "Adaptive harmonic fractional Fourier transform," *IEEE Signal Process. Lett.*, vol. 6, no. 11, pp. 281–283, 1999.

[123] L. Stanković, "A measure of some time-frequency distributions concentration," *Signal Process.*, vol. 81, no. 3, pp. 621–631, 2001.

[124] E. Merzbacher, *Quantum Mechanics.* NY: John Wiley and Sons Ltd, 1998.

[125] G. Folland and A. Sitaram, "The uncertainty principle: A mathematical survey," *The Journal of Fourier analysis and applications*, vol. 3, no. 3, pp. 207–238, 1997.

[126] K. Selig, "Uncertainty principles revisited," *Electronic Transations on Numerical Analysis*, vol. 14, pp. 165–177, 2002.

[127] D. Mustard, "Uncertainty principles invariant under the fractional Fourier transform," *Journal of the Australian Mathematical Society, Series B*, vol. 33, pp. 180–191, 1991.

[128] G. Xu, X. Wang, and X. Xu, "The logarithmic, Heisenberg's and short-time uncertainty principles associated with fractional Fourier transform," *Signal Process.*, vol. 89, no. 3, pp. 339–343, 2009.

[129] ——, "Genaralized entropic uncertainty principle on fractional Fourier transform," *Signal Process.*, vol. 89, no. 12, pp. 2692–2697, 2009.

[130] J. Zhao, R. Tao, Y. Li, and Y. Wang, "Uncertainty principles for linear canonical transform," *IEEE Trans. Signal Process.*, vol. 57, no. 7, pp. 2856–2858, 2009.

[131] V. Katkovnik, "New method for varying adaptive bandwidth selection," *IEEE Trans. Signal Process.*, vol. 47, no. 9, pp. 2567–2571, 1999.

[132] X. Xia, G. Wang, and V. Chen, "Quantitative SNR analysis for ISAR imaging using joint time-frequency analysis−short time Fourier transform," *IEEE Trans. Aerosp. Electron. Syst.*, vol. 38, no. 2, pp. 649–659, 2002.

[133] J. Jeong and W. Williams, "Mechanism of the cross-terms in spectrograms," *IEEE Trans. Signal Process.*, vol. 40, no. 10, pp. 2608–2613, 1992.

[134] M. Bell and R. Grubbs, "Jem modeling and measurement for radar target identification," *IEEE Trans. Aerosp. Electron. Syst.*, vol. 29, no. 1, pp. 73–87, 1993.

[135] J. Wilbur and R. Mcdonald, "Nonlinear analysis of cyclically correlated spectral spreading in modulated signals," *J. Acoust. Soc. Amer.*, vol. 92, no. 1, pp. 219–230, 1993.

[136] S. Huang, R. Lerner, and K. Parker, "On estimating the amplitude of harmonic vibration from the doppler spectrum of reflected signals," *J. Acoust. Soc. Amer.*, vol. 88, no. 6, 1990.

[137] Y. Zhang, S. Qian, and T.Thayaparan, "Detection of a manoeuvring air target in strong sea clutter via joint time-frequency representation," *IET Signal Process.*, vol. 2, no. 3, pp. 216–222, 2008.

[138] A. Karakasiliotis, A. Lazarov, P. Frangos, G. Boultadakis, and G. Kalognomos, "Two-dimensional ISAR model and image reconstruction with stepped frequency-modulated signal," *IET Signal Process.*, vol. 2, no. 3, pp. 277–290, 2008.

[139] [Online] Available at: http://airborne.nrl.navy.mil/ vchen/tftsa.html.

[140] S. Kay, *Fundamentals of Statistical Signal Processing: Detection Theory.* NJ: Prentice Hall, 1998.

[141] P. Tichavsky and P. Handel, "Two algorithms for adaptive retrieval of slowly time-varying multiple cisoids in noise," *IEEE Trans. Signal Process.*, vol. 43, no. 5, pp. 1116–1127, 1995.

[142] O. Macchi and N. Bershad, "Adaptive recovery of a chirped sinusoid in noise, part I: Performance of the RLS algorithm," *Signal Process.*, vol. 39, no. 3, pp. 583–594, 1991.

[143] N. Bershad and O. Macchi, "Adaptive recovery of a chirped sinusoid in noise, part II: Performance of the LMS algorithm," *Signal Process.*, vol. 39, no. 3, pp. 595–602, 1991.

[144] G. Adams and R. Evans, "Neural networks for frequency line tracking," *IEEE Trans. Signal Process.*, vol. 42, no. 4, pp. 936–941, 1994.

[145] S. Kay and G. F. Boudreaux-Bartels, "On the optimality of the Wigner distribution for detection," in *IEEE Int. Conf. Acoust., Speech, and Signal Process. (ICASSP)*, vol. 10, 1985, pp. 1017–1020.

[146] L. Cirillo, A. Zoubir, and M. Amin, "Parameter estimation for locally linear FM signals using a time-frequency Hough transform," *IEEE Trans. Signal Process.*, vol. 56, no. 9, pp. 4162–4175, 2008.

[147] W. Li, "Wigner distribution method equivalent to dechirp method for detecting a chirp signal," *IEEE Trans. Acoust., Speech, Signal Process.*, vol. 35, no. 8, pp. 1210–1211, 1987.

[148] P. Hough, "A method and means for recognizing complex patterns," *U. S. Patent 3,069,654*, 1962.

[149] D. Ballard, "A survey of the Hough transform," *Comput. Vis., Graph., Image Process.*, vol. 44, no. 1, pp. 87–116, 1998.

[150] ——, "Generalizing the hough transform to detect arbitrary shapes," *Pattern Recognition*, vol. 13, no. 2, pp. 111–122, 1981.

[151] B. Carlson, E. Evans, and S. Wilson, "Search radar detection and track with the Houth transform," *IEEE Trans. Aerosp. Electron. Syst.*, vol. 30, no. 1, pp. 109–115, 1994.

[152] Q. Zhang, T. Yeo, H. Tan, and Y. Luo, "Imaging of a moving target with rotating parts based on the Hough transform," *IEEE trans. Geosci. Remote Sens.*, vol. 46, no. 1, pp. 291–299, 2008.

[153] J. Turan, P. Filo, and D. Siskovicova, "Parameter estimation based on Hough transform," *I*, vol. 44, no. 1, pp. 87–116, 1998.

[154] R. Duda and P. Hart, "Use of the Hough tranformation to detect lines and curves in pictures," *Graph. andImage Process.*, pp. 11–12, 1972.

[155] P. Chevret, N. Gache, and V. Zimpfer, "Time-frequency filters for target classification," *J. Acoust. Soc. Am.*, vol. 106, no. 4, pp. 1829–1837, 1999.

[156] X. Zhu, G. Beauregard, and L. Wyse, "Real-time signal estimation from modified short-time fourier transform magnitude spectra," *IEEE Trans. Audio, Speech, and Language Process.*, vol. 15, no. 5, pp. 1645–1653, 2007.

[157] L. Stankovic, S. Djukanovic, and I. Djukanovic, "Space/spatial-frequency analysis based filtering," *IEEE Trans. Signal Process.*, vol. 48, no. 8, pp. 2343–2352, 2000.

[158] C. Pinnegar, "Time-frequency and time-time filtering with the S-transform and TT-transform," *Digital Signal Process.*, vol. 15, no. 6, pp. 604–620, 2005.

[159] L. Stankovic, "On the time-frequency analysis based filtering," *Annals of Telecommunications*, vol. 55, no. 5-6, pp. 216–225, 2000.

[160] V. Katkovnik, "Robust M-periodogram," *IEEE Trans. Signal Process.*, vol. 46, no. 7, pp. 3104–3107, 1998.

[161] C. Nikias and M. Shao, *Signal Processing with alpha-stable distributions and applications*. NY: John Wiley and Sons Ltd, 1995.

[162] Y. Ju, "Processing algorithms for signals with time-varying frequencies," Ph.D. dissertation, Electrical & Electronic Engineering, Nanyang Technological University, 2009.

[163] I. Djurović and L. Stanković, "Robust Wigner distribution with application to the instantaneous frequency estimation," *IEEE Trans. Signal Process.*, vol. 49, no. 12, pp. 2985–2993, 2001.

[164] J. Xiao and P. Flandrin, "Multitaper time-frequency reassignment for nonstationary spectrum estimation and chirp enhancement," *IEEE Trans. Signal Process.*, vol. 55, no. 6, pp. 2851–2860, 2007.

[165] K. Fitz and L. Haken, "On the use of time-frequency reassignment in additive sound modeling," *Journal of the Audio Engineering Society*, vol. 50, no. 11, pp. 879–893, 2002.

[166] S. Ram and H. Ling, "Application of the reassigned joint time-frequency transform to wideband scattering from waveguide cavities," *IEEE Antennas Wireless Propag. Lett.*, vol. 6, pp. 580–583, 2007.

[167] ——, "Analysis of microdopplers from human gait using reassigned joint time-frequency transform," *Electr. Lett.*, vol. 43, no. 23, pp. 282–287, 2007.

[168] F. Plante, G. Meyer, and W. Ainsworth, "Improvement of speech spectrogram accuracy by the method of reassignment," *IEEE Trans. Speech Audio Process.*, vol. 6, no. 3, pp. 282–285, 1998.

[169] S. Hainsworth, M. Macleod, and P. Wolfe, "Analysis of reassigned spectrograms for musical transcription," in *Proceedings of the IEEE Workshop on the Applications of Signal Processing to Audio and Acoustics (WASPAA)*, 2001, pp. 23–26.

[170] S. Hainsworth, "Analysis of musical audio for polyphonic transcription," [Online] Available at: citeseer.ist.psu.edu/hainworth01analysis.html, 2001.

[171] M. Niethammer and L. J. Jacobs, "Time-frequency representations of lamb waves," *J. Acoust. Soc. Am.*, vol. 109, no. 5, pp. 1841–1847, 2001.

[172] C. Richard and R. Lengellé, "Joint recursive implementation of time-frequency representations and their modified version by the reassignment method," *Signal Process.*, vol. 60, no. 2, pp. 163–179, 1997.

[173] G. Nilsen, "Recursive time-frequency reassignment," *IEEE Trans. Signal Process.*, vol. 57, no. 8, pp. 3283–3287, 2009.

[174] S. Hainsworth and M. Macleod, "Time frequency reassignment: a review and analysis," *Tech. Rep. CUED/F-INFENG/TR.459, Cambridge University Engineering Department*, 2003.

[175] S. Fulop and K. Fitz, "Algorithms for computing the time-corrected instantaneous frequency (reassigned) spectrogram, with applicaitons," *J. Acoust. Soc. Amer.*, vol. 119, no. 1, pp. 360–371, 2006.

[176] S. Kadambe and G. F. Boudreaux-Bartels, "A comparison of the existence of cross terms in the Wigner distribution and the squared magnitude of the wavelet transform and the short time Fourier transform," *IEEE Trans. Signal Process.*, vol. 40, no. 10, pp. 2498–2517, 1992.

[177] X. Li, Y. Wang, G. Bi, Y. Shi, and X. Li, "On the cross-terms in LPPs," in *IEEE International Symposium on Circuits and Systems (ISCAS)*, 2009.

[178] K. Kodera, R. Gendrin, and C. de Villedary, "Analysis of time-varying signals with small BT values," *IEEE Trans. Acoust., Speech, Signal Process.*, vol. 26, no. 1, pp. 64–76, 1978.

[179] F. Auger and P. Flandrin, "Generalization of the reassignment method to all bilinear time-frequency and time-scale representations," in *IEEE Int. Conf. Acoust., Speech, and Signal Process. (ICASSP)*, 1994, pp. 317–320.

[180] P. Huber, *Robust Statistics*. NY: John Wiley & Sons Ltd, 1981.

[181] I. Djurović, L. Stanković, and J. Bohme, "Robust L-estimation based forms of signal transforms and time-frequency representations," *IEEE Trans. Signal Process.*, vol. 15, no. 7, pp. 1753–1761, 2003.

[182] C. Hoare, "Quicksort," *Computer Journal*, vol. 5, no. 1, pp. 10–16, 1962.

[183] S. Zabin and H. Poor, "Efficient estimation of the class A parameters via the EM algorithm," *IEEE Trans. Inf. Theory*, vol. 37, no. 1, pp. 60–72, 1991.

[184] J. Friedmann, H. Messer, and J. Cardoso, "Robust parameter estimation of a deterministic signal in impulsive noise," *IEEE Trans. Signal Process.*, vol. 48, no. 4, pp. 935–942, 2000.

[185] S. Barbarossa and O. Lemoinea, "Analysis of nonlinear FM signals by pattern recognition of their time-frequency representation," *IEEE Signal Process. Lett.*, vol. 3, no. 4, pp. 112–115, 1996.

[186] B. Boashash and M. Mesbah, "Signal enhancement by time-frequency peak filtering," *IEEE Trans. Signal Process.*, vol. 52, no. 4, pp. 929–937, 2004.

[187] J. Walker and A. Potts, "Time-frequency spectra of music," [Online] Available at: http://www.uwec.edu/walkerjs/media/TFSM.pdf.

[188] X. Cheng, J. Hart, and J. Walker, "Time-frequency analysis of musical rhythm," *Notices of the American Mathematical Society*, vol. 56, no. 3, pp. 356–372, 2009.

[189] M. Tazebay and A. Akansu, "Adaptive subband transforms in time-frequency excisers for DSSS communications systems," *IEEE Trans. Signal Process.*, vol. 43, no. 11, pp. 2776–2782, 1995.

[190] S. Lach, M. Amin, and A. Lindsey, "Broadband interference excision for software-radio spread-spectrum commnications using time-frequency distribution synthesis," *IEEE J. Sel. Areas Commun.*, vol. 17, no. 4, pp. 704–714, 1999.